WASHINGTON UNIVERSITY IN ST.LOUIS
Department of Physics

Dissertation Examination Committee:
Kater Murch, Chair
Erik Henriksen
Eli Levenson-Falk
Mikhail Tikhonov
David Wisbey

Studying Quantum Memory Effects of the Environment with Superconducting Circuits

by
Daria Kowsari

A dissertation presented to
Washington University in St. Louis
in partial fulfillment of the
requirements for the degree
of Doctor of Philosophy

May 2023

Table of Contents

List of Figures

List of Tables

Acknowledgments

First and foremost, I would like to express my sincere gratitude for my advisor, Kater Murch. Kater is a great example of a generous boss who knows how to be a leader without putting too much pressure on his peers which results in a thriving work environment. I owe my success to his mentorship style for always walking beside me and supporting the ideas that I came up with. Just to mention one case, I vividly recall the day that I talked to him about starting a project on a proposal that I conceived and it was really surprising to me how wholeheartedly he embraced this, which resulted in one of the first fabrication papers ever published from the group.

I feel honored for being among such intelligent colleagues in Murch lab. First, I want to thank Patrick Harrington and Jonathan Monroe for patiently training me on all the skills that I needed to succeed in my career over the first two years of my studies. I am grateful for working along Weijian Chen, who always helped me fix my mistakes and become a better scientist. Interacting closely with Chandrashekhar Gaikwad helped me grasp the intuition behind the complex physical phenomena that we stumble upon daily in lab. Finally, I want to thank my lab mates Maryam Abbasi, Xiayu Linpeng, Xingrui Song, Yunzhao Wang, Kaiwen Zheng, Serra Erdamar, Alexandria Udenkwo, Yueheng Shi, and Xinyi Zhao for allowing me to gain new knowledge from them.

Above that, I am thankful for all the help from the physics department staff, Todd Hardt, Mary Sullivan, Shirley McTigue, Sarah Akin, Sai Iyer, Alison Verbeck, and Kelly March. You are the main reason that research can move forward in the department. In addition, I am grateful for all the device fabrication and material characterization assists from the staff at the institute of materials science and engineering department at WashU, Rahul Gupta, Huafang Li, Liangji Zhang, and Beth Gartin.

I had a chance to collaborate with many remarkable scientist all over the states throughout my studies. Starting with the colleagues at Washington University, I am immensely grateful for all the fabrication and material characterization help from Erik Henriksen and Xinyi Du as well as Aravind Nagulu and Yi Zhuang for granting me the opportunity to learn the details of the microwave engineering techniques. I was lucky to be a part of the ADMX team consisting of James Buckley, Jonah Hoffman, and Jordan Russell to broaden my knowledge on the dark side of physics.

I want to express my appreciation for David Wisbey and Nathan Thobaben at Saint Louis University. Your immense help with al the resonator microwave measurements helped me conceive the research article I was most proud of in my doctoral studies. Moreover, collaborating with Eli Levenson-Falk and Haimeng Zhang at the University of Southern

California broadened my knowledge on the theory of open quantum systems. Specifically, I would like to thank Haimeng for all the discussions that we had throughout the years that always helped me stay on the right track.

I am lucky that I made such supportive and caring friends such as, Ziyuan Zhang, Kiandokht Amiri, and Katie Randolph who always kept me happy and sane. Above all, I would like to thank the best friends anyone could ever make in the whole world, Jacob Moran and Sydney Kaplan for their unconditional love and kindness. Although this is the part that our lives get separated, I believe that nothing can come between a true friendship, not even thousands of miles.

Finally, I would like to thank my family, my beloved mother, father, sister, and aunts for their endless support and love. This achievement would not be possible without the sacrifices you made throughout the years.

Daria Kowsari

Washington University in Saint Louis

May 2023

Travel far and wide and you shall possess the secrets of man.

Hávamál

ABSTRACT OF THE DISSERTATION

Studying Quantum Memory Effects of the Environment with Superconducting Circuits

by

Daria Kowsari

Doctor of Philosophy in Physics

Washington University in St. Louis, 2023

Professor Kater Murch, Chair

The presence of the environment in real-world experiments that strive to harness quantum mechanical effects is inevitable. This results in dissipation, which is known to be the main source of errors that prevent us from building a practical quantum computer. Nevertheless, one can employ the environment as a resource, especially when there is a strong coupling between the system and its environment. In this regime, the dynamics of the system is governed by the generalized Nakajima-Zwanzig master equation incorporating all the memory effects induced by the environment. The existence of memory allows us to investigate intriguing phenomena, such as the revival of an entangled state. This acts as a measure to probe the characteristics of the environment. In this work, we study the evolution of an entangled state in this regime via a multi-qubit superconducting processor. In addition to the dissipation caused by the presence of the environment, the intrinsic material defects, e.g. the two-level system fluctuators, also contribute to the loss in superconducting circuits. To circumvent this issue, we explore a method to fabricate niobium superconducting circuits under high vacuum pressures to suppress the microwave loss caused by materials.

Chapter 1

Introduction

1.1 From Quantum Circuits to Open Quantum Systems

1.1.1 History of quantum circuits

Since the first conception of macroscopic quantum effects in circuits in 1980 [1], quantum circuits have been developed to realize artificial atoms in the laboratory. One example of such a system is the Josephson tunnel junction (JJ), consisting of two superconducting layers mediated by a thin insulating layer [2]. The quantum effect occurs below the critical temperature of the superconductor, where the cooper pairs tunnel through the thin insulator with a phase difference across the insulating layer [3]. In one of the pioneering experiments, Martinis et. al. [4] measured the quantized energy levels of a JJ to further develop the idea of utilizing this circuit as the desired artificial atom for quantum computing purposes. Later on in a remarkable experiment, Yamamoto et. al. [5] demonstrated a controllable gate operation performed on a pair of charge quantum bits (qubit) to realize a controlled-NOT gate in a superconducting circuit. However, due to the lack of a robust readout scheme and short coherence times of the circuit, these experiments never produced any groundbreaking results besides demonstrating the feasibility of such implementations in superconducting circuits.

To circumvent the problematic aspects of the early-stage circuits mentioned above, the first step was to integrate the cavity quantum electrodynamics (QED) techniques to the superconducting circuits platform to make the readout more robust and reliable. First proposals to realize a practical control scheme was to use open three-dimensional cavities where the qubit can be coupled to the electromagnetic fields of the cavity to reliably control its state and result in entangled states [6]. In another remarkable article, Schoelkopf's group [7] suggested a novel architecture to protect the qubit against the electromagnetic environment surrounding it to achieve a high-fidelity readout incorporating a one-dimensional transmission line. Nevertheless, the intrinsic short coherence times of the qubit architectures to date was a still a major hindering factor in realizing high-fidelity qubit gates. A major leap towards the improvement of the coherence times of the qubits was taken by Koch et. al. [8] in 2007. They proposed a new charge insensitive qubit circuit, named "transmon". The transmon circuit consists of the widely-used JJ element attached to a large shunted capacitor. Due to the large capacitor, the charge energy due to the capacitor is much smaller than that of the energy stored in the junction, hence making it less susceptible to charge noise.

The invention of the transmon circuit was a significant achievement towards advancing the superconducting quantum computing platform. Moreover, it paved the path for advancing circuit QED techniques, allowing the realization of multi-qubit processors. This advancement in the circuit QED field yielded in remarkable results, ranging from the implementation of simple quantum computing algorithms [9, 10, 11] and error correction demonstrations [12, 13, 14, 15] to surpassing the classical computing capabilities by employing devices with tens of qubits [16] and even facilitating the search for the dark matter axions with quantum-limited amplifiers [17].

1.1.2 The environment and memory

The dissipation caused by the system-environment in the real-world experimental setups is inevitable. This dissipation is one of the major factors contributing to the decoherence in superconducting circuits alongside the dissipation caused by the intrinsic material defects formed during the fabrication of such circuits. Dissipation is also the main feature in superconducting circuits that allows us to measure the state of the qubit while driving the system. Therefore, a complete isolation of the system is impractical for the quantum computing field. Nevertheless, one can take advantage of this dissipation and enable it as a resource in our system using quantum bath engineering techniques.

In the bath engineering scheme, the dissipation is engineered to result in stabilized quantum states [18, 19, 20] as well as enabling the realization of cat states [21]. In all of these applications, the system-environment interaction is assumed to be weak, meaning that the dissipation takes place in only one direction, with energy and information flow towards the environment. However, once we step into the strong coupling regime, a back-flow of information from the environment to the system is also possible [22]. This new type of dissipation only happens in a non-Makovian system and the remarkable outcome of this phenomenon is that the current state of the qubit will depend on its entire history, giving rise to the concept of memory. To emphasize on this, the concept of quantum memory has been proposed to be one of the revolutionary aspects of quantum computing, which allows us to build quantum networks by using the concept of quantum repeaters [23].

A non-Markovian environment can be used to preserve a state [24, 25, 26], achieve steady states with higher coherence compared to their Markovian counterparts [27], and study the noise correlations in multi-qubit processors [28, 29]. In addition to these applications, this concept results in peculiar phenomena in open systems, such as an increase in the distinguishability of two states over time [30] and the revival of an entangled state during free evolution of the system [31]. These interesting phenomena can be utilized as a measure for the degree of non-Markovianity of the system. In this thesis, we study the effects of the non-Markovianity on the evolution of entanglement in a three-qubit superconducting processor by taking into account one of the qubits as the environment to emulate a simple non-Markovian bath.

1.2 Circuit quantum electrodynamics

In this section, we introduce the central element of the quantum processors, the transmon qubit. Next, we analyze the couplings between the transmon qubit and the cavity required for the state readout of such circuits. Finally, we describe the heterodyne readout scheme used for the simultaneous measurement of multi-qubit processors.

1.2.1 Transmon qubit

Since the inception of the superconducting quantum circuits, the transmon qubit [8], modeled as a nonlinear oscillator, took a lot of attention due to having the longest coherence time reported to date. This was achieved by adding a large capacitor to the circuit that makes it insensitive to the charge noise. In addition, the ease of fabrication was another factor to make this the most ubiquitous element of all the superconducting qubit processors.

We start the derivation of the transmon qubit Hamiltonian, by first looking at a simple classical linear LC oscillator. In this circuit, the energy oscillates between the magnetic and electric energies generated by the inductive L and capacitive C elements of the circuit. We define the time-dependent energy and flux present in the circuit as [32],

$$E(t) = \int_{-\infty}^{t} V(s) I(s)\, ds, \tag{1.1}$$

$$\Phi(t) = \int_{-\infty}^{t} V(s)\, ds, \tag{1.2}$$

where $V(s)$ and $I(s)$ are the time-dependent voltage and current of the circuit.

Using the relations, $V = L\,dI/dt$ and $I = C\,dV/dt$, we can derive the inductive and capacitive energies using Eq. 1.1 and 1.2 as,

$$\mathcal{E}_C = \frac{1}{2}C\dot{\Phi}^2, \tag{1.3}$$

$$\mathcal{E}_L = \frac{1}{2L}\Phi^2. \tag{1.4}$$

Using the Legendre transformation to define the capacitor charge as, $Q = C\dot{\Phi}$, we arrive at the Lagrangian of the system,

$$\mathfrak{L} = \mathcal{E}_C - \mathcal{E}_L = \frac{1}{2}\frac{Q^2}{C} - \frac{1}{2L}\Phi^2. \tag{1.5}$$

The Hamiltonian is now given as,

$$H = Q\dot{\Phi} - \mathfrak{L} = \frac{1}{2}\frac{Q^2}{C} + \frac{1}{2L}\Phi^2 = \frac{1}{2}\frac{Q^2}{C} + \frac{1}{2}LI^2, \tag{1.6}$$

which is the expected Hamiltonian for a classical parallel LC circuit with the resonance frequency of $\omega_{\text{res}} = 1/\sqrt{LC}$.

Promoting the charge and flux coordinates to operators, allows us to have a quantum mechanical description of the above Hamiltonian (Eq. 1.6). These operators follow a commutation relation as, $[\Phi, Q] = i\hbar$, where $\hbar$ is the reduced Planck constant. Defining the reduced flux and charge operators as $\phi = 2\pi\Phi/\Phi_0$ and $n = Q/2e$, with e denoting the charge of the electron and $\Phi_0 = h/(2e)$ representing the magnetic flux quantum, we can rewrite the quantum mechanical description of the Hamiltonian as,

$$H = 4E_C n^2 + \frac{1}{2}E_L\phi^2, \tag{1.7}$$

where $E_C = e^2/2C$ is the charging energy generated by the capacitive element in the circuit and $E_L = (\Phi_0/2\pi)^2/L$ is the inductive energy. Note that the reduced flux and charge operators also follow a commutation relation as, $[\phi, n] = i$.

The Hamiltonian in Eq. 1.7 resembles the quantum harmonic oscillator, where the energy levels are equally split [33]. This fact is not suitable for qubit experiments where we need to address the energy levels separately to imitate a two-level system similar to a spin-1/2 particle. Therefore, one has to add a non-linear element to the circuit in order to split the energy levels unevenly.

To this end, we replace the inductive element in the circuit with a Josephson junction (JJ) [34] consisting of two superconducting leads sandwiched by an insulator (see Sec. 4.3.1 for more details on the JJ fabrication). In contrast with the linear circuit, the voltage and current relations are given as, $I = I_c\sin(\phi)$ and $V = (\hbar/2e)d\phi/dt$, where I_c is the critical current of the junction, defined as the maximum current that the JJ can handle before it turns resistive. Using these relations and the same approach as the linear LC oscillator, we can derive the Hamiltonian of a non-linear LC circuit consisting of a JJ as,

$$H = 4E_c n^2 - E_J\cos(\phi), \tag{1.8}$$

where $E_J = I_c\Phi_0/2\pi$ is the energy stored in the junction and $E_c = e^2/2C_{\text{tot}}$ is the charging energy with $C_{\text{tot}} = C_J + C_s$ being the sum of the capacitance from the JJ and the shunted capacitor. The second term in the Hamiltonian (Eq. 1.8) is the essence of achieving an anharmonic oscillator as the potential no longer has a parabolic shape.

To enter the transmon regime, we need to set the energy stored in the junction to be much larger than the capacitive energy ($E_J \gg E_C$). This can be easily achieved by connecting the JJ to shunted capacitor pads to get $C_s \gg C_J$. The main advantage of this choice of parameters is that the circuit will no longer be susceptible to charge noise.

We can now rewrite the charge and phase operators in terms of the creation (annihilation) operators of a single excitation in the circuit, $a^\dagger(a)$,

$$n = i\, n_0(a - a^\dagger), \tag{1.9}$$

$$\phi = \phi_0(a + a^\dagger), \tag{1.10}$$

where $n_0 = (E_J/32E_C)^{1/4}$ and $\phi_0 = (2E_C/E_J)^{1/4}$ are the zero point quantum fluctuations of the charge and phase. Expanding the second term in the circuit Hamiltonian (Eq. 1.8) yields,

$$E_J \cos(\phi) = \frac{1}{2}E_J\phi^2 - \frac{1}{24}E_J\phi^4 + \mathcal{O}(\phi^6). \tag{1.11}$$

It is clear that the linear classical LC oscillator Hamiltonian can be recovered by only keeping the first term of this expansion. However, we can arrive at the Duffing oscillator Hamiltonian by keeping the terms up to the fourth term after applying rotating wave approximation and inserting the charge and phase operators defined above (Eq. 1.9 and 1.10),

$$H = \omega_q a^\dagger a + \frac{\alpha}{2} a^\dagger a^\dagger a a, \tag{1.12}$$

with $\alpha = \omega_{12} - \omega_{01} = -E_C/\hbar$ denoting the anharmonicity of the circuit defined as the difference of the first and second transition frequencies of the qubit, which is always negative and it typically lies in the range of $100 - 300$ MHz for a transmon qubit. Moreover, the first transition frequency of the qubit is, $\hbar\omega_q = \sqrt{8E_J E_C} - E_C$. Due to the large anharmonicity of the transmon qubit, we can drive the first two energy levels of the circuit reliably and simplify the drive Hamiltonian as,

$$H = \omega_q \frac{\sigma_z}{2}, \tag{1.13}$$

where σ_z is the Pauli-z operator.

In most experiments, we need to tune the frequency of the qubit to get to the desired spot. The main reason behind this is that to apply some two-qubit gates, we need to bring the qubits into resonance with each other to perform entangling (swap) gates [35]. In addition, the current limitations in the fabrication of the superconducting circuits does not allow for a safe margin of error in the frequency of the circuit, and having the tuning ability is always desirable to circumvent the issues emerged from fabrication [36]. To achieve such a functionality, we make use of superconducting quantum interference devices (SQUID) [2]. A SQUID consists of two JJs in parallel, forming a loop for the flux to pass through. In this structure, the inductance of the JJ depends on the flux threading the loop as,

$$L_{\mathrm{SQUID}} = \frac{\Phi_0}{4\pi I_c \cos(\pi\Phi_{\mathrm{ext}}/\Phi_0)}, \tag{1.14}$$

where Φ_{ext} is the external flux applied to the loop.

The effective Hamiltonian of a SQUID is in the form of,

$$H = 4E_C n^2 - 2E_J|\cos(\pi\Phi_{\mathrm{ext}}/\Phi_0)|\cos(\phi). \tag{1.15}$$

We can now define the flux-dependent junction energy as, $E'_J(\Phi_{\mathrm{ext}}) = 2E_J|\cos(\pi\Phi_{\mathrm{ext}}/\Phi_0)|$. Since the frequency of the transmon is proportional to $\sqrt{E_J}$, applying an external magnetic flux to the SQUID loop shifts its frequency with a maximum attainable frequency of $\hbar\omega_{\mathrm{max}} = 4\sqrt{E_J E_C} - E_C$, in the case of having symmetric JJs in the SQUID.

1.2.2 Qubit and cavity coupling

In circuit quantum electrodynamics (cQED), we are interested in coupling the qubit to the standing waves of a harmonic oscillator to readout its state. To achieve such a coupling, the qubit is placed near the oscillator to make sure of its coupling. The Hamiltonian of such a system in the basis of the qubit $\{|i\rangle\}$ can be written as a sum of the cavity, qubit, and the interaction terms,

$$\begin{aligned} H &= H_c + H_q + H_{\text{int}} \\ &= \hbar\omega_c a_c^\dagger a_c + \hbar \sum_j \omega_j |j\rangle\langle j| + \hbar \sum_{i,j} g_{ij} |i\rangle\langle j| (a_c + a_c^\dagger), \end{aligned} \tag{1.16}$$

where ω_c is the resonance frequency of the cavity, $a_c^\dagger$ (a_c) denote the creation (annihilation) operators of the cavity, and g_{ij} represents the dipole coupling rate between the cavity and qubit.

After applying a rotating wave approximation (eliminating the terms that excite the energy for both the cavity and qubit) and assuming a limited number of transmon levels, we can replace the qubit Hamiltonian with the Hamiltonian of an anharmonic oscillator (Eq. 1.12) and rewrite the total Hamiltonian (Eq. 1.16) as,

$$H = \hbar\omega_c a_c^\dagger a_c + \hbar\omega_q a_q^\dagger a_q + \frac{\alpha}{2} a_q^\dagger a_q^\dagger a_q a_q + \hbar g (a_q^\dagger \sigma_- + a_q \sigma_+). \tag{1.17}$$

where $\sigma_\pm$ are the raising and lowering operators of the cavity. This Hamiltonian can be further simplified by only considering the first two energy levels of the transmon and treating it as a two-level system (Eq. 1.13),

$$H_{\text{JC}} = \hbar\omega_c (a_c^\dagger a_c + \frac{1}{2}) + \frac{\hbar\omega_q}{2}\sigma_z + \hbar g (a_q^\dagger \sigma_- + a_q \sigma_+), \tag{1.18}$$

where the vacuum energy has been added back and $g = g_{0,1}$. This is the well-known Jaynes-Cummings (JC) Hamiltonian [37] that describes the dynamics of the interactions between the cavity and qubit in the cQED framework.

After diagonalizing the JC Hamiltonian (Eq. 1.18) in the bare basis, we arrive at the dressed eigenstates [38],

$$|n\rangle|+\rangle = \cos(\theta_n)|n-1\rangle|e\rangle + \sin(\theta_n)|n\rangle|g\rangle, \tag{1.19}$$

$$|n\rangle|-\rangle = -\sin(\theta_n)|n-1\rangle|e\rangle + \cos(\theta_n)|n\rangle|g\rangle, \tag{1.20}$$

where $\tan(2\theta_n) = 2g\sqrt{n}/\Delta$ and the eigenenergies of, $E_{n,\pm} = n\hbar\omega_c \pm (\hbar/2)\sqrt{4g^2n + \Delta^2}$. In the limit where the qubit and cavity are in resonance ($\Delta = 0$), we reach the vacuum-Rabi splitting regime where the eigenstates takes the form, $|n\rangle|\pm\rangle = (|n\rangle|g\rangle \pm |n-1\rangle|e\rangle)/\sqrt{2}$ with an energy difference of $2g$, which results in oscillations between an excitation in the qubit and cavity, typically known as a vacuum-Rabi oscillation.

1.2.3 Dispersive limit

The JC Hamiltonian (Eq. 1.18) can be further simplified once we are in the dispersive regime where the frequency difference of the cavity and qubit is much larger than their coupling rate, $\Delta = |\omega_q - \omega_c| \gg g$. In this regime, the cavity and qubit cannot directly exchange energy. A Schrieffer-Wolf transformation [39] using the unitary operator $U = \exp[g(a_q a_c^\dagger - a_q^\dagger a_c)/\Delta]$ can be applied to Eq. 1.18 to obtain the dispersive JC Hamiltonian by keeping the first two order of g/Δ ratio,

$$UH_{\mathrm{JC}}U^{\dagger}/\hbar = \frac{1}{2}\omega_q\sigma_z + \omega_c(a_c^{\dagger}a_c + \frac{1}{2}) + \chi a_c^{\dagger}a_c\sigma_z + \frac{\chi}{2}\sigma_z, \tag{1.21}$$

where $\chi = g^2/\Delta$ is the dispersive shift. After defining $\tilde{\omega}_q = \omega_q + \chi$ to account for the Lamb shift of the qubit and ignoring the vacuum energy of the cavity, Equation 1.21 can be rearranged to clarify how we readout the state of the qubit,

$$H_{\mathrm{dis}}/\hbar = (\omega_c + \chi\sigma_z)a_c^{\dagger}a_c + \frac{1}{2}\tilde{\omega}_q\sigma_z. \tag{1.22}$$

It is clear from this representation that the cavity frequency (as well as its phase) experiences a shift of $\omega_c \pm \chi$ contingent on the state of the qubit. This phenomenon is the backbone of the quantum non-demolition (QND) measurement, which is stemmed from the fact that the interaction and the drive Hamiltonians commute [40]. In this scheme, the measurement result on the system is not altered during the readout action of the system.

The QND aspect of the measurement also depends on the number of photons present in the cavity. In the case that we surpass the critical photon number $n_c = \Delta^2/(4g^2)$, the dispersive JC Hamiltonian (Eq. 1.22) no longer holds [7] and the outcome of the measurement will be affected during the readout process of the cavity. Thereby, the critical photon number sets an upper bound for the allowed power level for the readout to result in a QND measurement.

To uncover a new interpretation of the dispersive JC Hamiltonian, we can rearrange the terms in Eq. 1.21 such that,

$$H_{\text{dis}}/\hbar = \omega_c a_c^\dagger a_c + \frac{1}{2}(\omega_q + \chi + 2\chi a_c^\dagger a_c)\sigma_z. \tag{1.23}$$

This representation reveals two important frequency shifts of the qubit. First, we have the Lamb shift of the qubit by $\chi/2$, which is always present in the coupled qubit cavity system. Due to the Lamb shift, the frequency of the qubit is always measured in a laboratory by taking into account its effect. Additionally, there is a more interesting term, where a shift of χ in the qubit frequency is dependent on the photon number in the cavity ($a_c^\dagger a_c$). This mechanism is known as the AC-Stark shift [41]. The AC-Stark shift induced by thermal and microwave noise present in the system can result in the qubit frequency fluctuations and cause dephasing. Therefore, it is crucial to properly thermalize the processor, utilize microwave filters and attenuators to minimize the dephasing rate emerged from AC-Stark shift [42].

Projective measurement

In the simplest scheme of the quantum measurement, we strive to measure the system projected along different basis $|i\rangle$ (with $i = x, y, z$) to reconstruct the full density matrix. Since in our measurement setup we always measure the system along the Z-axis, tomography pre-rotations are required to project the system along the other axes. More details on the tomography scheme is presented in Section 4.4.

To briefly cover the theory behind this measurement scheme, we start by considering the system in a state, represent by the density matrix formalism [33] as,

$$\rho = \sum_n P_n |\psi_n\rangle\langle\psi_n|, \tag{1.24}$$

where P_n is the probability of finding the system in $|\psi_n\rangle$.

We can now define the operators $\Pi_i = |i\rangle\langle i|$, that project the state to the basis i, where the projected density is written as,

$$\rho' = \frac{\Pi_i \rho \Pi_i^\dagger}{\mathrm{Tr}(\Pi_i \rho \Pi_i^\dagger)}, \tag{1.25}$$

with the outcome probability given as, $p_i = \mathrm{Tr}(\rho\Pi_i)$. To elaborate, every time we measure a system, it collapses into an eigenstate of the i basis with a probability of p_i. The projective measurement is central to the experiments conducted in this work, where we are mainly interested in reconstructing the density matrix of the system.

1.2.4 Qubit readout

Now we can shift gears from theory and discuss the actual experimental setup in the laboratory. As mentioned in Sec. 1.2.3, the state of the qubit shifts the frequency of the readout cavity. The goal of this section is to explain the microwave techniques required to harness this shift in the frequency and utilize that to discriminate between two states of the qubit. For simplicity, we first start by introducing the idea behind the measurement of a single qubit and then extend the method for the simultaneous measurement of multiple qubits. The derivations in this Section are adapted from [43].

The best way to harness the state discrimination of a qubit is by examining the in-phase and quadrature components of the voltage (IQ plane). The readout scheme starts by examining the output signal from the fridge after interacting with the readout resonator (either reflection or transmission) and the frequency of ω_{RO}, which can be written as, $s(t) = A_{\mathrm{RO}}\cos(\omega_{\mathrm{RO}}t + \theta_{\mathrm{RO}})$, where A_{RO} and θ_{RO} are the state-dependent amplitude and phase of the resonator that we need to measure. It is easier to write the signal in the complex plane as,

$$s(t) = \mathrm{Re}(A_{\mathrm{RO}}e^{i\omega_{\mathrm{RO}}}e^{i\theta_{\mathrm{RO}}}), \tag{1.26}$$

where $\mathrm{Re}(\cdot)$ takes the real part of a complex function.

To measure the state of a qubit, we investigate the phasor of the signal that contains all the information to discriminate the states of the qubit by considering the phase shift in the resonator. The phasor can be written in terms of the in-phase (I) and quadrature (Q) as,

$$A_{\mathrm{RO}}e^{i\theta_{\mathrm{RO}}} = A_{\mathrm{RO}}\cos(\theta_{\mathrm{RO}}) + iA_{\mathrm{RO}}\sin(\theta_{\mathrm{RO}}) = I + iQ. \tag{1.27}$$

The main advantage of using the I and Q is to perform a homodyne or heterodyne measurement. To this end, we typically utilize analog IQ microwave mixer. To obtain the desired amplitude and phase of the resonator, we send the signal $s(t)$ (Eq. 1.26) from the output of the cryostat to the RF port alongside a reference signal that enters the local oscillator (LO) mixer port in the form of, $y(t) = A_{\mathrm{LO}} \cos(\omega_{\mathrm{LO}} t)$ as shown in (Fig. 1.1(a)). The resulting signals in the I and Q ports of the mixer now are digitized with the intermediate frequencies, $\omega_{\mathrm{IF}} = \omega_{\mathrm{RO}} \pm \omega_{\mathrm{LO}}$. One obtains the phase and amplitude of the resonator after signal processing discussed below.

Homodyne readout

In the case of the homodyne measurement, the LO frequency is identical to the output signal frequency from the fridge, resulting in a zero intermediate frequency. Hence, the I and Q outputs from the mixer are both at DC and simply time-averaging the signal is sufficient to obtain the amplitude and phase of the readout. For the Q port of the mixer, the signal is multiplied by $y_Q(t) = -(A_{\mathrm{LO}}/2)\sin(\omega_{\mathrm{LO}}\, t)$ and similarly, we have $y_I(t) = (A_{\mathrm{LO}}/2)\cos(\omega_{\mathrm{LO}}\, t)$ for the I port. The time averages over the time interval T are in the form of,

$$I = \frac{1}{2T}\int_0^T dt\, s(t) y_I(t) = \frac{A_{\mathrm{RO}} A_{\mathrm{LO}}}{8} \cos(\theta_{\mathrm{RO}}), \tag{1.28}$$

$$Q = \frac{1}{2T}\int_0^T dt\, s(t) y_Q(t) = \frac{A_{\mathrm{RO}} A_{\mathrm{LO}}}{8} \sin(\theta_{\mathrm{RO}}), \tag{1.29}$$

where the 1/2 factor behind the integral rises from the fact the signal $(s(t))$ is equally branched in the I and Q. From these relations, we can write the amplitude and phase as,

$$A_{\mathrm{RO}} \propto \sqrt{I^2 + Q^2}, \tag{1.30}$$

$$\theta_{\mathrm{RO}} = \arctan(Q/I). \tag{1.31}$$

The state discrimination of the signal occurs by having distinct phases contingent on the state of the qubit. Homodyne measurement, however, suffers from two major issues. First, the signal is demodulated to DC, which makes the measurement susceptible to $1/f$ noise. The more hindering factor of this type of measurement is that it is quite complex and rather expensive to extend this method to the multi-qubit measurements, where one needs to simultaneously probe the state of the qubits. To overcome these problems, we introduce a more general measurement method, known as the heterodyne measurement.

Heterodyne readout

The main difference between the heterodyne and homodyne measurement is that in the heterodyne scheme, the local oscillator and the readout resonator frequencies are different, giving rise to an intermediate frequency ($\omega_{\mathrm{IF}} = |\omega_{\mathrm{RO}} - \omega_{\mathrm{LO}}|$) in the I and Q digitized output signals (Fig. 1.1(a)). To generate such a signal, the up (down)-conversion techniques are typically used to achieve the desired RO frequency. The reader is encouraged to visit Section 3.3.3 of [38] for more details on such microwave engineering methods.

Using the same approach as the homodyne measurement to take the time average of the I and Q signals, we can write,

$$I_{\mathrm{IF}} = \frac{1}{2T}\int_0^T dt\, s(t) y_I(t) = \frac{A_{\mathrm{RO}} A_{\mathrm{LO}}}{8} \cos(\omega_{\mathrm{IF}} t + \theta_{\mathrm{RO}}), \tag{1.32}$$

$$Q_{\mathrm{IF}} = \frac{1}{2T}\int_0^T dt\, s(t) y_Q(t) = \frac{A_{\mathrm{RO}} A_{\mathrm{LO}}}{8} \sin(\omega_{\mathrm{IF}} t + \theta_{\mathrm{RO}}). \tag{1.33}$$

In this case, the demodulated signals oscillate with at a frequency of ω_{IF}. To digitally demodulate the signal we first need to consider the I and Q signals at each time step during the sampling time as,

$$I_{\mathrm{IF}}(n) = \frac{A_{\mathrm{RO}}A_{\mathrm{LO}}}{8}\cos(\Omega_{\mathrm{IF}}n + \theta_{\mathrm{RO}}), \tag{1.34}$$

$$Q_{\mathrm{IF}}(n) = \frac{A_{\mathrm{RO}}A_{\mathrm{LO}}}{8}\sin(\Omega_{\mathrm{IF}}n + \theta_{\mathrm{RO}}),, \tag{1.35}$$

where $n = t/\Delta t$ and $\Omega_{\mathrm{IF}} = \omega_{\mathrm{IF}}\Delta t$ is the digital frequency with the sampling duration of Δt. Now the digital demodulation over the time interval $(n_1 : n_2)$ is given as,

$$I = \frac{1}{\Delta n}\sum_{n=n_1}^{n_2} I_{\mathrm{IF}}(n)\cos(\Omega_{\mathrm{IF}}n), \tag{1.36}$$

$$Q = \frac{1}{\Delta n}\sum_{n=n_1}^{n_2} Q_{\mathrm{IF}}(n)\sin(\Omega_{\mathrm{IF}}n). \tag{1.37}$$

Rewriting the demodulated signals (Eq. 1.36 and 1.37) in the complex form we have, $z_{\mathrm{IF}}(n) = I + iQ = A_{\mathrm{RO}}A_{\mathrm{LO}}\exp(i\theta_{\mathrm{RO}})\exp(i\Omega_{\mathrm{IF}}n)/8$. Hence, by multiplying each data point of the demodulated signal by $\exp(-i\Omega_{\mathrm{IF}}n)$, we end up in the desired non-rotating frame with a change in θ_{RO}, determining the state separation. Figure 1.1(b) shows the $I - Q$ plane of a demodulated signal with two separated clusters representing the ground and excited state of the qubit after averaging the signal for 20,000 times.

Extending this to the simultaneous two-qubit readout, first we need to send the readout signal basically as sum of two modulated signals with different frequencies to result in a signal consisting of two distinct sidebands required to probe the state of two cavities. Next, the signals I_{IF} and Q_{IF} (Eq. 1.32 and 1.33) are demodulated twice over a certain timespan with different intermediate frequencies determined by the frequency of the cavities. This results in separate $I - Q$ blobs required to fully reconstruct the two-qubit density matrix with the tomography prerotation pulses described later in Sec. 4.4.2.

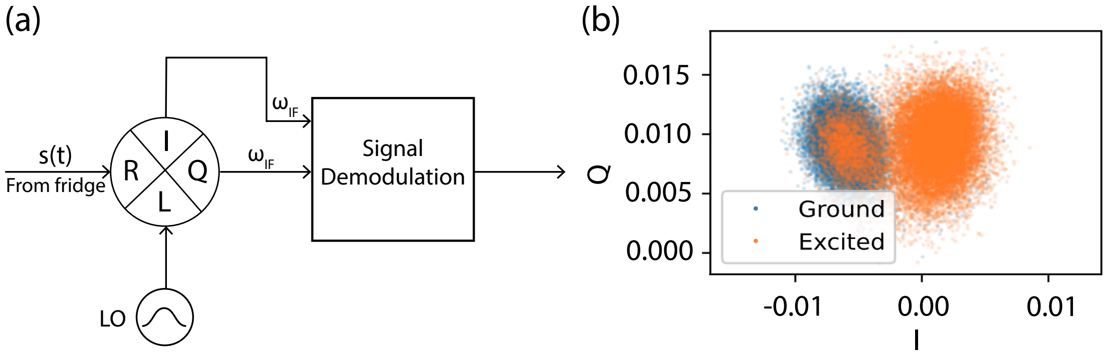

Figure 1.1: (a) The IQ mixer wiring for the demodulation of the output signal. (b) The I-Q plane representing the separated ground and excited qubit states.

Chapter 2

Study of Microwave Loss in Electron-Beam Evaporated Niobium Superconducting Circuits

This chapter covers the results of our published article on the loss characterization in electron-beam evaporated niobium [44]. It starts by a brief overview of various sources of loss in the superconducting circuits in Section 2.1. Then in Section 2.2, I go over the basics of the metal oxidation as well as a literature review on the niobium oxides known to this date. Section 2.3 discusses the well-known two-level system theory. The basics of the microwave resonators, fabrication techniques, and the material characterizations are covered in Section 2.4. Finally, Section 2.5 shows the microwave measurement setup and the loss characterization results of the fabricated devices.

2.1 Sources of loss in niobium superconducting circuits

Recent achievements in quantum computing have shown that superconducting circuits are one of the most promising platforms to realize the long-sought challenge of building a fault-tolerant quantum computer [16, 45, 46]. The performance of such devices are, however, limited by decoherence sources such as quasiparticles [47, 48, 49], magnetic vortices [50], and radiation effects [51]. Recent advances in fabrication techniques and microwave engineering have significantly reduced the impacts of the above-mentioned defects [52, 53, 54], thereby leaving two-level-system (TLS) fluctuators as the most prominent source of loss in superconducting circuits [55, 56, 57]. It has been shown that TLS defects are mainly located at metal-air (MA), substrate-air (SA), and metal-substrate (MS) interfaces [58, 59, 60, 61, 62]. The contribution of losses from these interfaces can be minimized by implementing careful surface treatments thus enhancing the coherence of the devices [63, 64].

Owing to its high superconducting transition temperature, critical field, and low microwave loss [65], niobium (Nb) has become one of the common materials used in the fabrication of superconducting circuits [66, 67]. Nevertheless, the known stoichiometric range of its native oxides results in a complex loss-inducing MA interface [68, 69]. Lately, it has been shown that removing the oxides on the MA interface of Nb films can result in highly coherent devices, proving MA as the lossiest interface in these circuits [70, 71]. Additionally, conventional niobium deposition techniques, such as DC magnetron sputtering can result in a damaged

MS interface due to the presence of high energy argon ions [72] and point defects stemming from trapped argon atoms [73].

In this work, we investigate a refined deposition method [74] of Nb utilizing an ultra-high vacuum (UHV) electron-beam evaporator as well as studying the impact of removing the native surface oxide of the films on the TLS defect densities. We fabricate the Nb thin films into coplanar waveguide (CPW) resonators due to their sensitivity to the true intrinsic TLS defect density of the materials [58, 75] and characterize the loss induced by TLS defects in the films.

2.2 Niobium oxygen system

The first step towards characterizing loss in Nb circuits is to fully comprehend its complex oxide system. This section starts with covering the basics of the well-known Cabrera-Mott oxidation model and further discusses the metallic niobium characteristics and its three prominent oxides and their unique properties.

2.2.1 Cabrera-Mott oxidation model

As shown in [70], the native oxide layer of the superconductors has the most significant contribution to the loss in superconducting circuits. Hence, studying the metal oxide growth following the renowned Cabrera-Mott model gives us a better insight in identifying and eliminating this source of loss in these circuits. This section covers the details behind this model and how oxides form on the surface of thin films adapted from [76].

The central assumption of the Cabrera-Mott model is that the electrons can freely ionize the adsorbed oxygen on the surface of the metal. This ionization results in a uniform potential on the metal-oxide interface due to the presence of the negatively charged oxygen anions and the positive metal surface. This potential is commonly known as the Mott potential, V_{m}. Therefore, the oxide growth occurs by the migration of the cations between the interatomic sites and the metal-oxide interface. This migration requires an initial activation energy, W, which is much higher than the succeeding migration barriers and since the oxide thickness x is thin in the initial stages, it can result in a strong electric field, $E = V_{\mathrm{m}}/x$. Furthermore, according to the Mott potential the migration barriers decrease by, $qaE/2$, where a is the distance between two interatomic sites and q denotes the atomic charge.

Cabrera-Mott also predicts that the oxide growth rate is contingent on the number of point defects on the metal-oxide interface due to their high activation barrier. The rate of the oxide growth estimated by this model is given as,

$$\frac{dx}{dt} = \frac{D}{a} \exp\left(\frac{qaE}{2k_{\mathrm{B}}Tx}\right), \tag{2.1}$$

where D, k_{B}, and T denote the diffusion constant of the material, the Boltzmann constant, and the temperature of the metal. Note that from Equation 2.1, we can see that the Cabrera-Mott theory predicts a self-limiting oxidation process by a maximum thickness of, $x_{\max} = qaE/2k_{\mathrm{B}}T$. In the limit where the oxidation thickness is much thinner than its maximum value, $x \ll x_{\max}$ we can derive the inverse-logarithmic law of the oxide growth rate,

$$x(t) \simeq \frac{1}{1-\ln t}. \tag{2.2}$$

This theory has been experimentally verified recently in the regrowth of the native surface oxide of the niobium superconducting resonators [71]. In this study, the authors exposed the samples to the ambient air for various time steps and realized an oxide regrowth governed by the Cabrera-Mott theorem, further proving the efficacy of this model.

2.2.2 Niobium and its oxides

Niobium

Discovered in 1801, niobium (Nb) belongs to the group V in the periodic table with electrical structure of Kr[$4d^45s^1$]. In its stable form, Nb is a metal crystallized in a body-centered cubic (BCC) lattice with a high melting temperature of 2477 °C and an electrical resistivity of 15.2 $\mu\Omega$/cm at room temperature [77]. Nb forms stable nitrides, carbides, borides, and silicides [78]. Therefore, it has been widely used in various industries from making high-strength steels used in the pipelines for gas and oil transportation to the making of nickel-based superalloys used in aircraft engines to prevent abrasion and corrosion [79, 80]. Adding to these applications, Nb is a type-II superconductor with a high critical temperature of $T_c \simeq 9.3$ and a critical magnetic field as high as $B_{c2} \equiv 420$ mT at 0 K [77, 81], making it ideal for the fabrication of low-loss superconducting circuits [66, 82].

Due to having a valence electron in its 4d energy level, Nb can form a thick native oxide layer with various stable oxygen compounds [83]. It has been reported that the thickness of this oxide layer can be as high as 6 nm [84] with a composition mostly consisted of niobium penta-oxide. The composition and thickness of such oxide is still a vast area of research due to its intricacy. However, it has been proposed that one can take advantage of heating up niobium above 2000 K in UHV [81] to remove the native oxide of niobium. Furthermore, the surface of the niobium can be passivated after removing the oxide to form a protective layer against ambient air, using conventional nitridation techniques [85].

Niobium monoxide

The very first oxidation state of niobium, niobium monoxide (NbO) represents Nb in its 2+ charge state. NbO forms a face-centered cubic (FCC) structure [86]. NbO has the highest point defects among all the transition metal monoxides with 25% of ordered vacancies in both the oxygen and niobium sublattices [87]. Niobium monoxide has a resistivity of 21 $\mu\Omega$/cm with a melting point of $\sim$1940 °C [88, 89].

Remarkably, NbO shows superconducting properties below the critical temperature, $T_c \simeq$ 1.38 [90] and it has been also explored that increasing the ratio of oxygen (niobium) in the compound significantly decreases (increases) the critical temperature due to the stark change in the resistivity of the sample [90]. To elaborate, this drastic change in the resistivity occurs because NbO can easily form a mixed-phase sample upon a slight change in the ratios of the oxygen and niobium present in the sample. There has not been any report on the applications of niobium monoxide in the industry to date. Nonetheless, because of the enhanced oxygen diffusion properties of NbO, it can be a viable option for niobium-based electrolytic capacitors [91].

Niobium di-oxide

Moving onwards to the second oxidation state, we have niobium di-oxide (NbO_2) with niobium present in its 4+ charge state. NbO_2 crystallizes in a tetragonal structure with a rutile sublattice [92] and a melting point of $\sim$1901 °C [77]. It is synthesized by controlled oxidation of Nb or NbO [93] as well as a reduction from Nb_2O_5.

At temperatures between 797 and 808 °C, NbO_2 experiences a crystal transformation to a rutile lattice as well as a second-order phase transition [92, 94]. This can be understood as a semiconductor-metal transition with a metallic conductivity of 10^3 $1/\Omega \cdot \text{cm}$ at these high temperatures [95]. In addition, the tetragonal phase of the niobium di-oxide has been characterized an n-type semiconductor with a band gap of $0.5 - 1.2$ eV and an electrical resistivity in the oder of 10^4 $\Omega \cdot \text{cm}$ [94, 96]. NbO_2 also exhibits abrupt jumps in its current-voltage characteristics indicating a resistive switching properties [97].

In terms of applications, NbO_2 has been utilized for making biosensors using Nb/NbO_2 electrodes [98]. Furthermore, the chemical stability of niobium di-oxide has inspired its application in making nanowires using chemical vapor transport method [99].

Niobium pentoxide

The last but not the least, we have the most thermodynamically stable oxide state of the niobium, known as niobium pentoxide (Nb_2O_5) with Nb in its 5+ charge state. Since all the electrons in the $4d$ energy level are bounded to the oxygen, Nb_2O_5 has the lowest electrical conductivity compared to the aforementioned oxide states [100]. Adding more to the complexity of the niobium-oxygen system, Nb_2O_5 can occur in various crystalline structures contingent on the preparation methods each with distinct physical properties. More precisely, niobium-pentoxide crystallizes in tetragonal, hexagonal, orthorhombic, and monoclinic structures [101, 102] with each structure taking up various phases, leading to a total of 4 structures with 9 different polymorphs [103, 104]. As an example, the monoclinic R-Nb_2O_5 phase can be formed by heating the niobium oxychloride ($NbOCl_3$) at 273 °C [105].

Despite its complexity, niobium pentoxide has the most promising application in technology. It has been shown that Nb_2O_5 exhibits a well-known behavior known as the memory in solids. This characteristic is described as how Nb_2O_5 behaves differently to the same heat treatment contingent on its original synthesis attributed to the present impurities and structural defects in the samples [106]. The immediate application following this feature is the resistive random access memory based on the passive electronic component, named memristor [107]. The resistance of the memristor is dependent on the history of the current passed through it. Hence, having a material such as Nb_2O_5 with memory of is origin can have direct applications in the realization of such an intriguing component.

In addition to all the well-studied oxides mentioned above, niobium has a range of non-stoichiometric oxides. These oxides are divided into two groups, one with stoichiometric ranges between Nb and NbO with 4 metastable oxides [108]. The other group is ranged between NbO_2 and Nb_2O_5 [109]. A comprehensive study of these metastable oxides is beyond the scope of this dissertation and the interested reader is encouraged to examine this review article for more details [110].

2.3 Two-level system model

This section starts with reviewing the background of the two-level system (TLS) model and moves onto the semi-empirical treatment proposed by Gao in 2008 [111] to quantify the TLS loss in superconducting circuits.

Known to be originated from the thermal, acoustic, and dielectric properties of the materials at milliKelvin temperatures, the TLS fluctuators are one of the main sources of loss in the superconducting circuits [112]. The unsaturated TLSs are excited by absorbing a photon and relaxed by dissipating that photon to the bath, which is the main decoherence mechanism in the superconducting circuits. Even though the origin of the TLS loss is yet not clearly determined [113], it has been proposed that the loss might be due to the presence of the polar molecules, e.g. hydroxyl bonds OH^-, and other impurities, resulting in a dipole coupling with the rf frequency electric fields [114]. In addition, there has been experimental results demonstrating that the TLS loss mainly resides in the various interfaces of the circuits with the highest contribution from the metal-air (MA) interface, where the amorphous native surface oxide of the metal is located [115].

The standard TLS model proposed by Anderson in 1972 [116] and Phillips in 1987 [117], predicts a broad spectrum of the tunneling states in an amorphous medium. These states incorporate dipole moments, capable of coupling to electric fields. Therefore, the TLS is referred to as one or a group of atoms tunneling between two sites. In this model, the system Hamiltonian in the local basis of two states $\{|\phi_1\rangle, |\phi_2\rangle\}$ can be written as,

$$H = \frac{1}{2}\begin{pmatrix} -\Delta & \Delta_0 \\ \Delta_0 & \Delta \end{pmatrix}, \tag{2.3}$$

where Δ is the energy difference between two states and Δ_0 denotes the tunnel splitting.

For this model, we assume a uniform distribution for Δ as,

$$P(\Delta, \Delta_0)d\Delta d\Delta_0 = \frac{P_0}{\Delta_0}d\Delta d\Delta_0, \tag{2.4}$$

with P_0 representing the two-level density of states.

The Hamiltonian (Eq. 2.3) can be diagonalized with eigenenergies, $E^{(\pm)}/2 = \pm\sqrt{\Delta^2 + \Delta_0^2}$ and eigenstates in the form of,

$$\begin{aligned} |\psi_1\rangle &= \cos\theta|\phi_1\rangle + \sin\theta|\phi_2\rangle, \\ |\psi_2\rangle &= \sin\theta|\phi_1\rangle - \cos\theta|\phi_2\rangle, \end{aligned} \tag{2.5}$$

where $\theta = 1/2 \tan^{-1}(\Delta_0/\Delta)$.

Furthermore, in the new basis representation $\{|\psi_1\rangle, |\psi_2\rangle\}$ the Hamiltonian can be rewritten as, $H_0 = |E|/2\sigma_z$, with σ_z denoting the Pauli-z matrix.

Now considering the TLS interacting with an external electric field $\vec{\mathcal{E}}$, we can write the effective Hamiltonian in the diagonalized basis as,

$$H_{\text{int}} = [\frac{\Delta}{|E|}\sigma_z + \frac{\Delta_0}{|E|}\sigma_x]\, \vec{d_0} \cdot \vec{\mathcal{E}}, \tag{2.6}$$

where $\vec{d_0}$ denotes the maximum transition dipole of a TLS with energy splitting E. The first term in Equation 2.6 is attributed to the permanent dipole moment and the latter term describes the transition dipole moment.

The total Hamiltonian of a TLS interacting with an external field is given as, $H = H_0 + H_{\text{int}}$. One can immediately notice the similarities of this Hamiltonian to that of a 1/2 spin interacting with a magnetic field in the form of,

$$H = -\hbar\gamma \vec{B} \cdot \vec{S}, \tag{2.7}$$

where $\vec{S} = \sigma/2$ with $\vec{B}$ consisting of the static ($\vec{B_0}$) and oscillating parts ($2\vec{B}' \cos\omega t$) resulting in two terms similar to Equation 2.6, and γ represents the gyromagnetic ratio.

For such a system in the presence of the longitudinal and transverse relaxation times T_1 and T_2 the Bloch equations of motion are given as,

$$\begin{aligned}
\frac{d}{dt}\langle S_x(t)\rangle &= \gamma(\langle S_y\rangle B_z - \langle S_z\rangle B_y) - \frac{\langle S_x\rangle}{T_2} = 0, \\
\frac{d}{dt}\langle S_y(t)\rangle &= \gamma(\langle S_z\rangle B_x - \langle S_x\rangle B_z) - \frac{\langle S_y\rangle}{T_2} = 0, \\
\frac{d}{dt}\langle S_z(t)\rangle &= \gamma(\langle S_x\rangle B_y - \langle S_y\rangle B_x) - \frac{\langle S_z\rangle - S_z^{\mathrm{eq}}[B_z(t)]}{T_1} = 0, \qquad (2.8)
\end{aligned}$$

with $S_z^{\mathrm{eq}} = \tanh(\hbar\gamma B_z(t)/2kT)/2$.

Solutions to Equation 2.8 are given in [118]. Using the solutions, the magnetic susceptibilities, $\chi_i(\omega)$ defined as,

$$\begin{aligned}
S_x &= \chi_x(\omega)\hbar\gamma B_x, \\
S_z &= \chi_z(\omega)\hbar\gamma B_z, \qquad (2.9)
\end{aligned}$$

can be resolved as,

$$\begin{aligned}
\chi_x(\omega) &= -\frac{S_z^0}{2\hbar}\left[\frac{1}{\omega_0 - \omega + iT_2^{-1}} + \frac{1}{\omega_0 + \omega - iT_2^{-1}}\right], \\
\chi_z(\omega) &= \frac{dS_z^{\mathrm{eq}}}{d(\hbar\gamma B_0)}\frac{1 - i\omega T_1}{1 + \omega^2 T_1^2}, \qquad (2.10)
\end{aligned}$$

where $\omega_0 = -\gamma B_0$ and

$$S_z^0 = \frac{1 + (\omega_0 - \omega)^2 T_2^2}{1 + (\gamma B_x')^2 T_1 T_2 + (\omega_0 - \omega)^2 T_2^2} S_z^{\mathrm{eq}}. \tag{2.11}$$

Given in Equation 2.10, the susceptibilities have distinct origins. $\chi_x(\omega)$ is attributed to the resonant response of the spins, while $\chi_z(\omega)$ represent more of a relaxation process. Following the same approach, we can define the susceptibility tensor of a TLS in an electric field as,

$$\overset{\rightrightarrows}{\chi}_{\mathrm{res}}(\omega) = -\frac{\sigma_z^0}{\hbar}\left[\frac{1}{\omega_E - \omega + iT_2^{-1}} + \frac{1}{\omega_E + \omega - iT_2^{-1}}\right]\vec{d}\vec{d}, \tag{2.12}$$

where

$$\begin{aligned} \sigma_z^0 &= \frac{1 + (\omega_E - \omega)^2 T_2^2}{1 + \Omega^2 T_1 T_2 + (\omega_E - \omega)^2 T_2^2} \sigma_z^{\mathrm{eq}}(E), \\ \sigma_z^{\mathrm{eq}}(E) &= -\tanh\left(\frac{E}{2k_{\mathrm{B}}T}\right), \end{aligned} \tag{2.13}$$

with $\omega_E = E/\hbar$, $\vec{d} = \vec{d_0}\Delta_0/E$, and $\Omega = 2\vec{d}\cdot\vec{\mathcal{E}}/\hbar$ denotes the Rabi frequency.

At microwave frequency ranges (∼GHz) and milliKelvin temperatures, we can write the TLS contribution to the dielectric function in presence of external electric fields with orientation $\hat{e}$ as,

$$\epsilon_{\mathrm{TLS}}(\omega) = \iiint \left[\hat{e}\cdot\overset{\rightrightarrows}{\chi}_{\mathrm{res}}(\omega)\cdot\hat{e}\right] P(\Delta, \Delta_0)\, d\Delta\, d\Delta_0\, d\hat{d} = \epsilon'_{\mathrm{TLS}}(\omega) - i\epsilon''_{\mathrm{TLS}}(\omega). \tag{2.14}$$

Under the assumption of the weak field and $\Omega^2 T_1 T_2 \ll 1$, Eq. 2.14 can be written as,

$$\epsilon_{\mathrm{TLS}}(\omega) = -\frac{2Pd_0^2}{3}\left[\Psi\left(\frac{1}{2} - \frac{\hbar\omega - i\hbar T_2^{-1}}{2i\pi k_{\mathrm{B}}T}\right) - \log\frac{E_{\max}}{2\pi k_{\mathrm{B}}T}\right], \tag{2.15}$$

with Ψ denoting the complex digamma function and $E_{\max}$ representing the maximum TLS energy splitting.

With the above relations for the dielectric function, the impact of the TLSs on the frequency shift (Δf_r) and the internal quality factor (Q_i) as a function of the temperature can be derived using circuit quantum electrodynamics [119] as,

$$\frac{\Delta f_r}{f_r} = -\frac{\int_{V_h} \epsilon'_{\mathrm{TLS}}(\omega)|\vec{\mathcal{E}}|^2\, d^3\vec{r}}{2\int_V \epsilon|\vec{\mathcal{E}}|^2\, d^3\vec{r}} = \frac{F\delta^0_{\mathrm{TLS}}}{\pi}\left[\mathrm{Re}\Psi\left(\frac{1}{2} - \frac{\hbar\omega}{2i\pi k_{\mathrm{B}}T}\right) - \log\frac{\hbar\omega}{2\pi k_{\mathrm{B}}T}\right], \tag{2.16}$$

$$\frac{1}{Q_i(T)} = -\frac{\int_{V_h} \epsilon''_{\mathrm{TLS}}(\omega)|\vec{\mathcal{E}}|^2\, d^3\vec{r}}{\int_V \epsilon|\vec{\mathcal{E}}|^2\, d^3\vec{r}} = F\delta^0_{\mathrm{TLS}}\tanh\left(\frac{\hbar\omega}{2k_{\mathrm{B}}T}\right), \tag{2.17}$$

where $\delta^0_{\mathrm{TLS}} = 3Pd_0/2\epsilon_h$ and the filling factor F is defined as,

$$F = \frac{\int_{V_h} \epsilon_h|\vec{\mathcal{E}}|^2\, d^3\vec{r}}{\int_V \epsilon|\vec{\mathcal{E}}|^2\, d^3\vec{r}}, \tag{2.18}$$

defined as the ratio of the electric energy stored in the material occupied by TLS with volume, V_h to that of the entire resonator with a total volume of, V.

Moreover, the power-dependence relation of the TLS-induced loss in the superconducting resonators under the assumption of the strong field after solving for the full integral in

Eq. 2.14 is given as,

$$\delta_{\mathrm{TLS}}(|\vec{\mathcal{E}}|) = F\delta^0_{\mathrm{TLS}}\frac{\tanh(\frac{\hbar\omega}{2k_{\mathrm{B}}T})}{\sqrt{1+|\frac{\vec{\mathcal{E}}}{\vec{\mathcal{E}_c}}|^2}}, \tag{2.19}$$

with $|\vec{\mathcal{E}_c}|$ denting the critical electric field which above the TLS contribution gets saturated and $|\vec{\mathcal{E}}|$ representing the magnitude of the electric field present in the sample. This relation can be rewritten in terms of the photon numbers present in the resonator in the form of,

$$\delta_{\mathrm{TLS}}(\langle n\rangle) = F\delta^0_{\mathrm{TLS}}\frac{\tanh(\frac{\hbar\omega}{2k_{\mathrm{B}}T})}{\sqrt{1+\frac{\langle n\rangle}{n_c}}}, \tag{2.20}$$

where n_c is the critical photon numbers in the resonator and the number of photons, n is directly proportional to the microwave power applied to the resonator P_{app} as,

$$\langle n\rangle = \frac{2}{\hbar\omega^2}\frac{Z_0}{Z_r}\frac{Q^2}{Q_c}P_{\mathrm{app}}. \tag{2.21}$$

Here, Z_0 is the characteristic impedance of the microwave environment and Z_r is the impedance of the CPW resonator. Q and Q_c denote the total and coupling quality factors of the resonator.

2.4 Superconducting co-planar waveguides

This section covers the basic foundations of microwave resonators treated as a simple inductance-capacitance circuit and further develops on the nano-fabrication techniques used to realize such circuits in the superconducting platform. Various material characterization techniques to identify the main sources of loss in such circuits are also described later in this section.

2.4.1 Basics of microwave resonators

Microwave resonators have a vast range of applications, from amplifiers [120] and filters [121] to quantum computing, where they are used to probe the state of a quantum bit [122]. Here, we start by studying a simple lumped element parallel resonator, which can be easily translated into the co-planar waveguide resonators used in this study to characterize the TLS-induced loss of the niobium films.

The simplest form of a resonator is a parallel circuit consisting of resistive, inductive, and capacitive components represented as R, L, and C. Figure 2.1(a) shows the diagram of such a circuit for a hanger-style microwave resonator with a coupling capacitance of C_{c}. Conventionally, the resonators are fabricated using thin superconducting metal films on a substrate with a thickness of a few hundred microns. The designed layout of a short-circuited $\lambda/4$ fabricated hanger-style co-planar waveguide (CPW) resonator with capacitive coupling to the feedline is shown in Fig. 2.1(b). Around resonance, the input impedance of such a circuit is given as,

$$Z_{\text{in}} = \Big(\frac{1}{R} + \frac{1}{i\omega L} + i\omega C\Big)^{-1}, \tag{2.22}$$

where the resonance frequency of the resonator is, $\omega_{\text{res}} = 1/\sqrt{LC}$.

Moreover, to quantify the resonator performance, we define the quality factor of the device as the ratio of the average energy stored in the device to the energy that is lost due to the various decoherence mechanism mentioned above. The resonator is typically coupled to a feedline by either inductive or capacitive coupling, contributing to the total quality factor. The coupling quality factor, Q_{c} is dependent on the gap between the coupling lead and the feedline as well as the length of the coupling lead, l_{c} (Fig. 2.1(b)). The total quality factor of

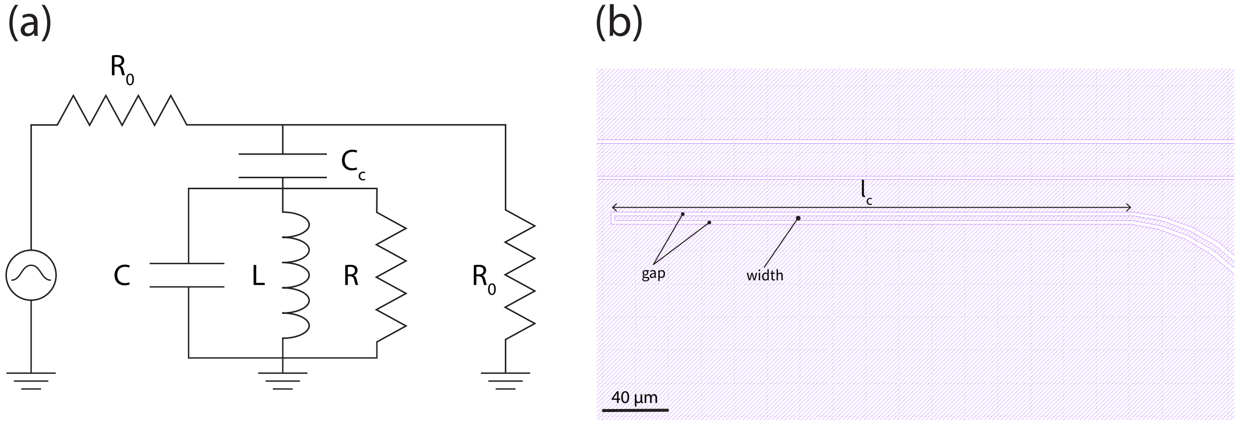

Figure 2.1: Hanger-style CPW microwave resonator represented as (a) a simple parallel RLC circuit and (b) the actual designed layout with the colored areas indicating the metallized regions.

the resonator is given as,

$$\frac{1}{Q_\mathrm{r}} = \frac{1}{Q_\mathrm{i}} + \frac{1}{Q_\mathrm{c}}, \tag{2.23}$$

with Q_i representing the internal quality factor of the resonator. If the loss in the system is only limited by the TLS defects, then Q_i will be a quantity of the TLS-induced loss. Additionally, the inverse of the quality factor is defined as the loss tangent, $1/Q_\mathrm{i} = \tan\delta_\mathrm{TLS} \simeq \delta_\mathrm{TLS}$ for $\tan\delta_\mathrm{TLS} < 10^{-2}$.

To extract the quality factors of the devices, the Lorentizan transmission profile of the resonators is fit to a function in the form of,

$$S_{21}(f) = ae^{-2\pi i f\tau}\left[1 - \frac{Q_\mathrm{r}e^{-i\phi_0}/Q_\mathrm{c}}{1 + 2iQ_\mathrm{r}(\frac{f-f_\mathrm{r}}{f_\mathrm{r}})}\right], \tag{2.24}$$

where f_r is the resonance frequency of the device. The fitting parameters a, τ, and ϕ_0 represent the gain, cable decay, and the rotation of the resonance circle in the complex plane. This fitting method is commonly known as the ϕ-rotation method, proposed by Gao in 2008 [111].

It has been shown that the electric field strength in the CPW is proportional to its center width size [58]. To elaborate, the smaller gap and width result in stronger fields, e.g. increasing the center width from 3 to 20 μm, reduces the filling factor by an order of magnitude. In this work, we set the center width to 3 μm in order to report the true filling-factor-adjusted loss tangent ($F\delta_\mathrm{TLS}$) of the deposited niobium films. Moreover, the Q_c of the resonators has been fixed to $\sim 600,000$ by adjusting the above-mentioned dimensions using the finite-element simulations described in details in Section 4.2.2.

2.4.2 Fabrication and material characterization

Samples are fabricated on a 2-inch, (100)-oriented, high resistivity (> 8 k$\Omega \cdot$ cm), single-side polished intrinsic silicon substrate cleaned in a Piranha solution (3:1 mixture of sulfuric acid and hydrogen peroxide) at 120 °C for 10 minutes followed by a 5-minute etch in a buffered-oxide-etch (BOE) solution to remove organic contaminants as well as the native silicon surface oxide [63, 123]. The BOE solution is a 6:1 mixture of ammonium fluoride (NH_4F) and hydrofluoric acid (HF). The substrate is then pumped down in a ultra-high vacuum (UHV) electron-beam evaporator (AJA ATC-ORION-8E) with a base pressure lower than 5 nTorr.

After loading the wafer, a 200 nm layer of 99.95% purity Nb is evaporated onto the substrate at a rate of 1.2 nm/min, which is commensurate to the previous study [74]. Note that the substrate is inevitably heated during this process due to the high melting point of Nb. Since pure Nb quickly adsorbs impurities [65], especially when heated, we let the sample remain under UHV conditions to cool down for 1-2 hours prior to proceeding to the next steps.

We spin and softbake the Nb samples with a high resolution photoresist (MicroChem S1805) and pattern the coated wafer with a Heidelberg DWL 66+ photolithography system. The pattern consists of 8 hanger-style, quarter-wavelength CPW resonators with a gap (width) of 2 μm (3 μm). Devices are designed to have frequencies ranging from 5.2 to 7 GHz with coupling quality factors $\sim 6 \times 10^5$. We develop the exposed resist by using a metal-ion-free solution (MicroChem MF-319). A reactive ion etch system (Oxford Plasmalab 100) is then used to etch the samples using a fluorine chemistry (Ar + SF_6). To assist the removal of the residual resist, the samples are first ashed for 30 seconds using oxygen plasma (Plasma Etch PE 50, 100 W, 15 cc/min) and then soaked in N-Methyl-2-pyrrolidone (NMP) heated to 70 °C for 8 hours. At last, samples are coated with the photoresist (S1805) to enhance their preservation over time [70] and protect against damage caused by dicing. Figure 2.2 depicts the complete fabrication flow of the CPW resonators.

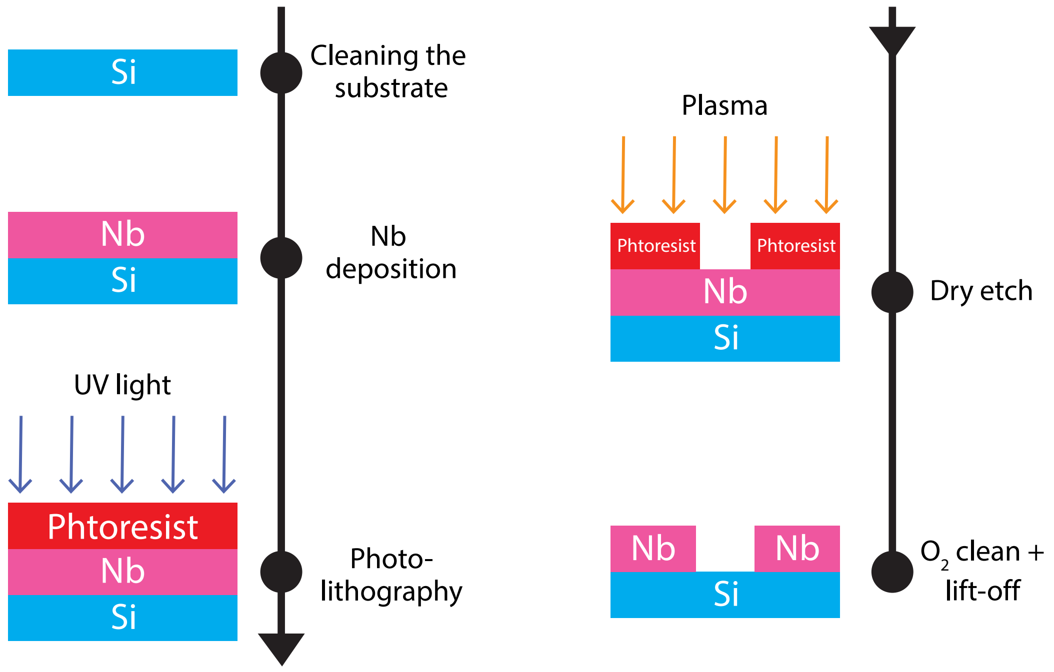

Figure 2.2: Fabrication flow of a superconducting Nb CPW resonator using a subtractive process.

Surface topography

Figure 2.3 illustrates the surface topography of the Nb films fabricated into CPWs (Fig. 2.3(a)) using the above-mentioned techniques. The scanning electron microscopy (SEM) image shows the elongated Nb grains formed on the surface (Fig. 2.3(b)). The dark-field scanning transmission electron microscopy (STEM) cross-sectional image of the etched films shows that our etching process is anisotropic (Fig. 2.3(c)). In this study, the etching has been engineered to result in trenches shallower than 500 nm for all the fabricated devices to maintain the effective substrate dielectric constant in the devices, and thereby avoid deviations from the desired resonance frequencies [124].

The STEM image shows grain sizes greater than 20 nm (Fig. 2.3(d)) exceeding previous values reported using the same deposition technique [74]. Correlation between the grain sizes and materials loss has been recently studied [125], substantiating the advantage of larger grain sizes by treating the grain boundaries as Josephson weak-links [126]. Finally, the films resulted in a superconducting transition temperature $\mathrm{T_c} = 9.20 \pm 0.06$ K and a residual resistivity ratio (RRR) of 4.8 (Fig. 2.3(e)) exhibiting the high quality of the evaporated Nb, in accord with recent results with sputtered Nb [125]. The RRR is calculated by dividing the surface resistance at 310 K to that right before the transition at 9.258 K as $2.33\ \Omega/0.49\ \Omega \simeq 4.8$.

Note that the films deposited at higher pressures (> 6 nTorr) resulted in a significantly lower transition temperature $\mathrm{T_c} \simeq 7.85$ K as well as a RRR of only 1.8, which can be attributed to the fact that having a low deposition rate makes the quality of the films extremely sensitive to the deposition environment. Therefore, having a UHV deposition environment is a crucial condition for achieving high quality films using this technique.

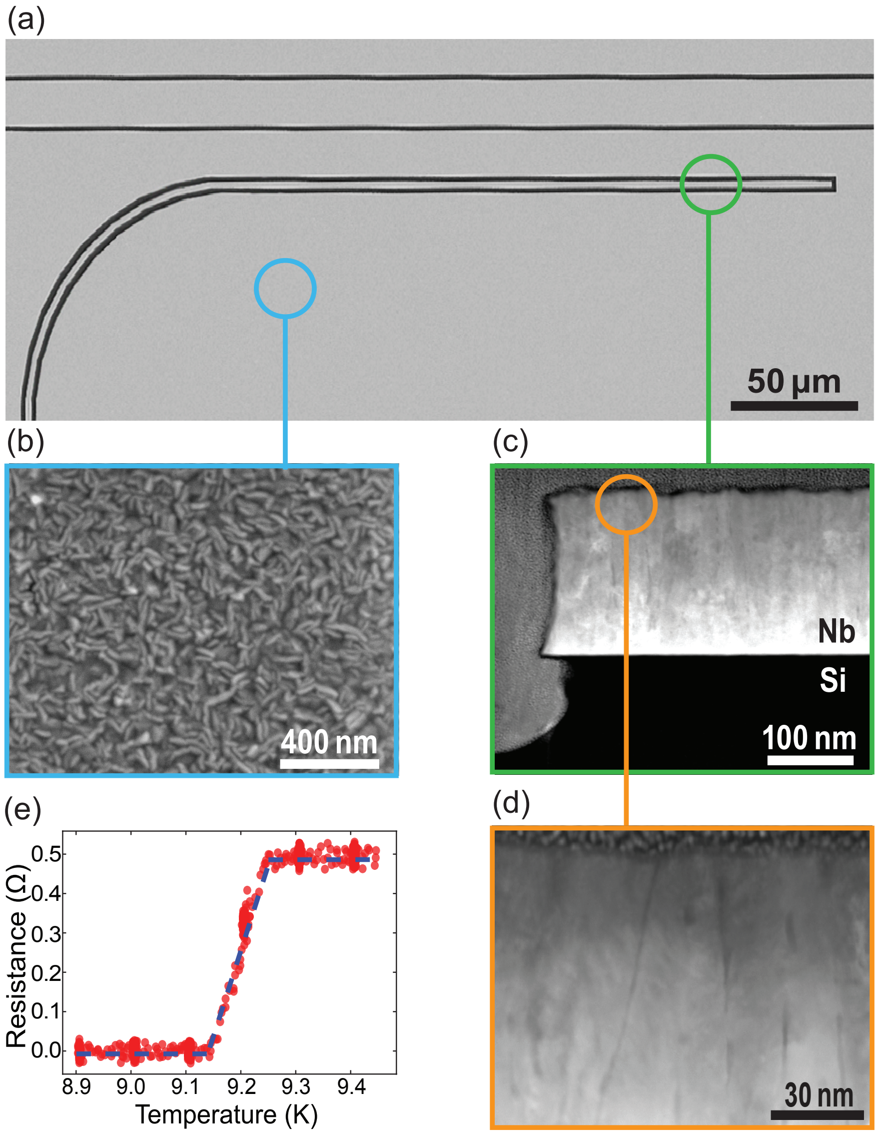

Figure 2.3: Surface topography of the niobium films. (a) The scanning electron microscopy image of a fabricated CPW resonator. (b) Dense grains of niobium formed on the surface. (c) Cross-sectional TEM image of the CPW trench. (d) The STEM image of the grains. (e) The surface resistance of the films against temperature. This figure is adapted from [44].

Metal-air interface characteristics

Transmission electron microscopy (TEM) images show a clear band of about 5 nm of oxide on top of the Nb, which is reduced to ∼1.7 nm after removing the surface oxides in a BOE solution for 20 minutes (Fig. 2.4(a, b)). Note that it takes about 20 minutes to transfer the sample to the characterization instruments, during which the oxide grows back following Cabrera-Mott theory [71]. To identify the elements present in the films, we perform electron-energy loss spectroscopy (EELS) measurements. Averaged EELS spectra are displayed in Fig. 2.4(c, d) along the red (orange) lines for the oxide (metal) regions of the TEM images in Fig. 2.4(a, b). The regions indicated by red lines exhibit a clear peak located at ∼535 eV, which corresponds to the presence of oxygen. Below this $\mathrm{NbO_x}$ band, there is no sign of this peak. Furthermore, EELS data revealed a clear reduction in the average oxygen content from ∼50% in the oxide band to less than 5% while scanning inside the metallic Nb film indicating the absence of oxygen impurities in the films.

We employ X-ray photoelectron spectroscopy (XPS) to further investigate the compounds present on the surface. Here we utilize a PHI VersaProbe II surface analysis instrument equipped with an aluminum K-alpha X-ray source. Under the optimal neutralization settings, an overall shift of ∼2.7 eV from the nominal binding energy values is observed due to the surface charge of the Nb films. The presented data have been adjusted to account for this shift. We examine the XPS spectrum of $\mathrm{Nb_{3d}}$ by curve fitting the data using the Lmfit [127] package. The fits reveal peaks for three distinct niobium oxides (Fig. 2.4(e, f)). These peaks were fit using the “skewedVoigt” model for asymmetric metallic Nb peaks and the “pseudoVoigt” model for all the other peaks using a Shirley inelastic background with $3d_{5/2}$ binding energies located at 202.05, 203.40, 205.84, and 207.38 eV for Nb, NbO, NbO_2, and Nb_2O_5 respectively for the untreated film. As discussed in Section 2.2.2, NbO is superconducting, with a transition temperature of 1.38 K [128]. Nb_2O_5 is the most thermodynamically stable state of the niobium-oxygen system with the highest binding energy (∼207 eV) and the lowest electrical conductivity [129]. Due to its various crystalline phases and physical properties, Nb_2O_5 has been considered as one of the main sources of defects present on the surface of Nb [110]. NbO_2 also contributes to the loss due to oxygen vacancies [125], which has the lowest participation in the deposited films reported here.

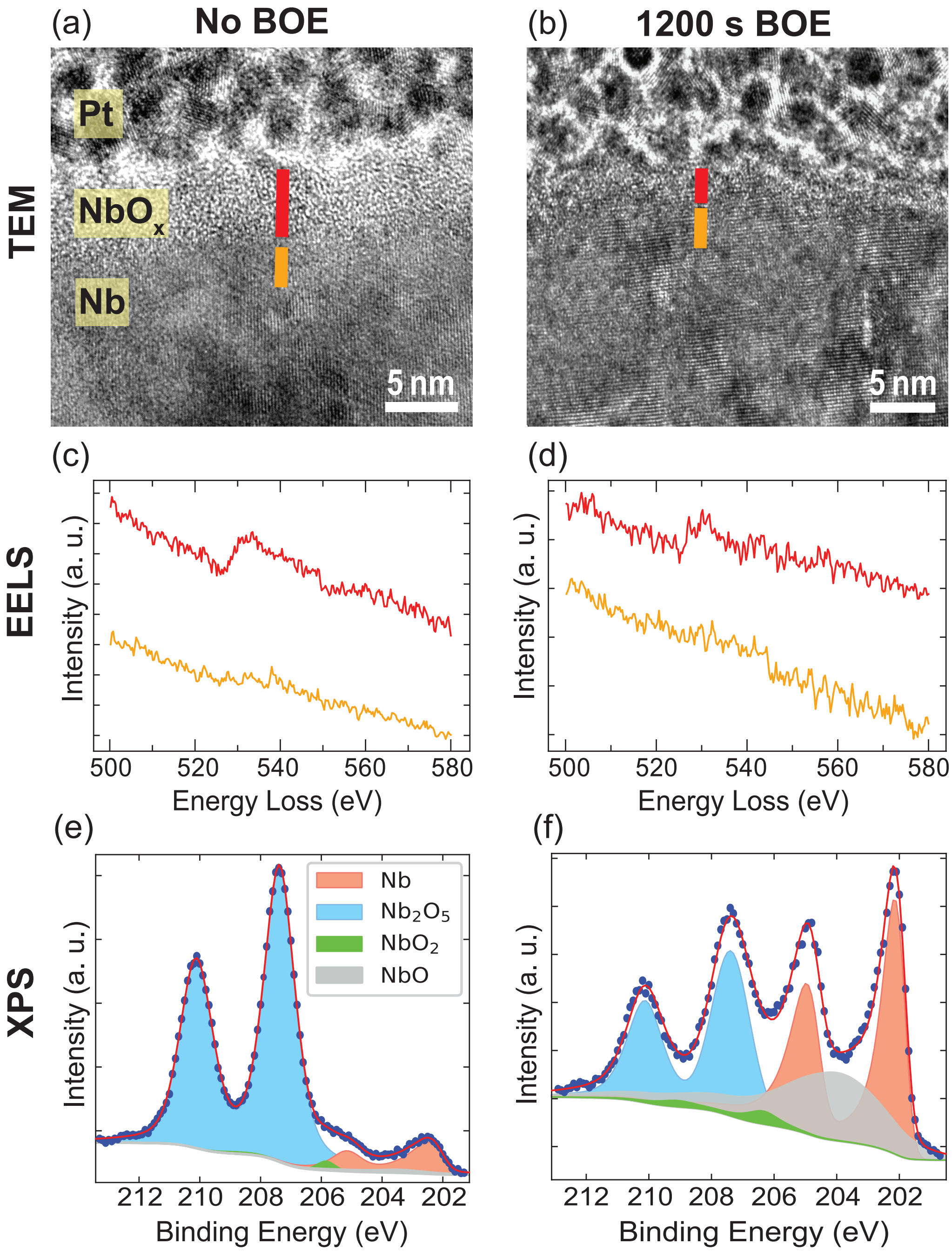

Figure 2.4: Characterized metal-air interface with and without post-cleaning the film using (a, b) TEM, (c, d) EELS, and (e, f) XPS. This figure is adapted from [44].

2.5 Measurement setup and microwave loss characterization

Prior to placement in the measurement cryostat, devices are cleaned for 7 minutes in an ultrasonic bath of acetone and isopropyl alcohol to remove particles on the samples and strip the protective photoresist. The transfer time to the fridge is kept under 90 minutes for the BOE post-cleaned samples to minimize oxide regrowth on the devices. The samples are placed inside palladium-plated copper microwave launch packaging surrounded by Cryoperm shielding to protect the devices from infrared radiation and external magnetic fields. Mounted devices are cooled inside an adiabatic demagnetization refrigerator (ADR) with a base temperature of 50 mK. Figure 2.5 shows the fridge diagram of the experiment where we utilize 70 dB of attenuation inside the fridge as well as the room temperature attenuators to reach the single-photon regime. A low-noise, high-gain amplifier is installed in the output line at the 4 K stage to amplify the signal. Moreover, we use two room-temperature amplifiers to further increase the transmission level of the signal.

The resonator transmission, S_{21}, is measured using a vector network analyzer in an experimental setup described previously [59, 130, 131]. Data is collected with the ADR in the temperature regulation mode. Figure 2.6(a) displays the transmission near the resonance of a particular device (indicated by the arrow in Fig. 2.6(c)) at low power. The quality factors are extracted by employing the ϕ-rotation method (Eq. 2.24). Figure 2.6(b) displays the internal loss tangent, δ_{int} (inverse of the internal quality factor Q_{i}) as a function of average photon number [51] of the BOE-cleaned device mentioned above. Using the TLS model (Eq. 2.20),

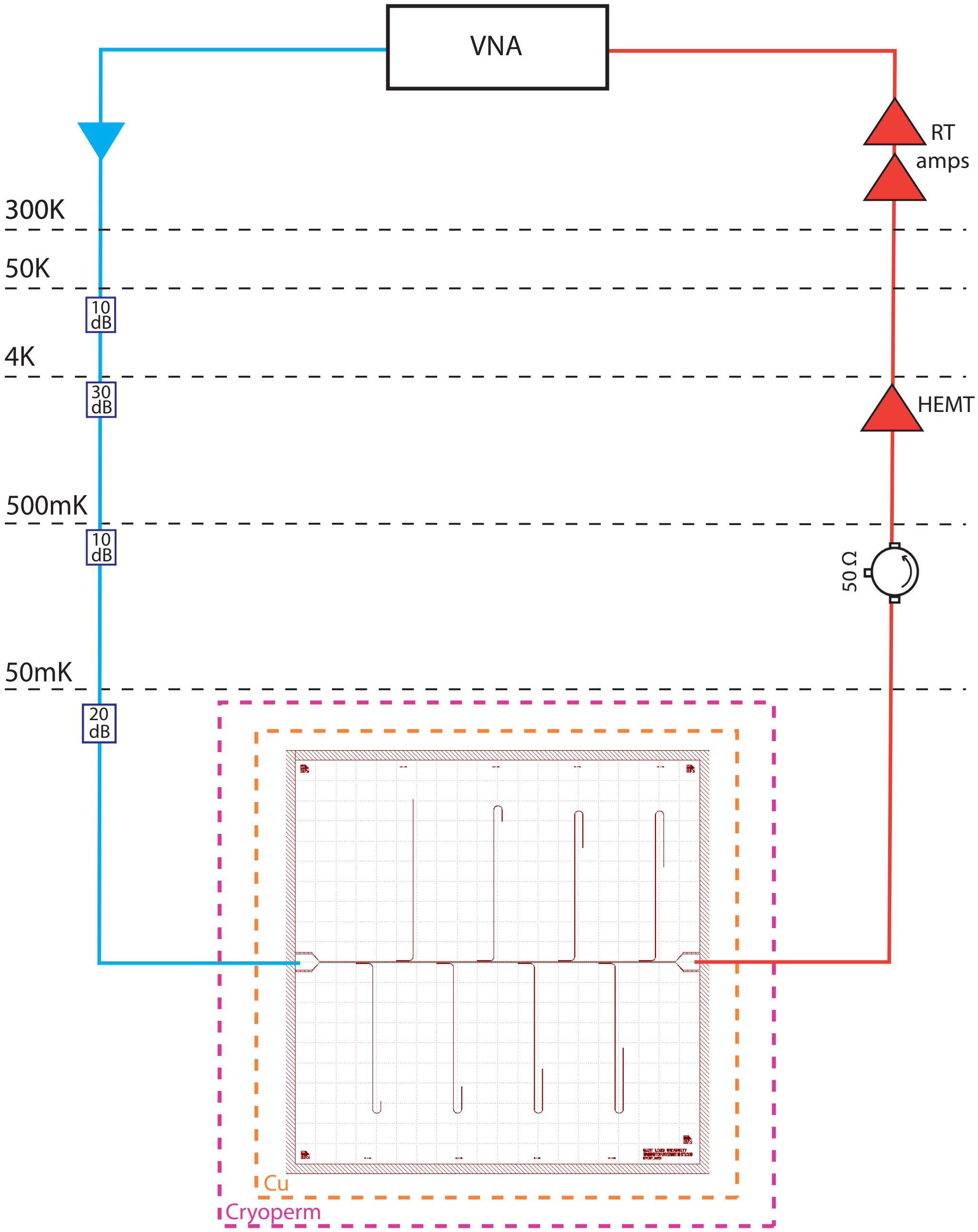

Figure 2.5: ADR diagram of the resonator's measurement setup indicating all the utilized cryogenic components.

we extract the filling-factor-adjusted TLS loss tangent ($F\delta_{\mathrm{TLS}}$), where F is defined as the fraction of the resonator's total loss stored in the TLS material. Figure 2.6(c) displays $F\delta_{\mathrm{TLS}}$

for several devices versus resonance frequency. The $F\delta_{\mathrm{TLS}}$ values are an order of magnitude smaller for the case of post-cleaned devices (red circles) than the untreated devices (blue squares) resulting in values as low as 0.15 ppm. The dashed line indicates the average value of $F\delta_{\mathrm{TLS}}$ of the post-cleaned devices. The average value is 0.32 ppm, well below previous results using the same CPW geometry [124]. The average low power Q_{i} of the post-cleaned devices is 1.13×10^6. In contrast, the untreated devices (blue squares) show an average TLS loss tangent of 1.21 ppm with an average single-photon regime Q_{i} of 3.35×10^5 comparable with other sputtered niobium studies [59, 132].

Figure 2.6(d) displays measurements of the internal loss of the aforementioned device versus temperature at a fixed power of -93 dBm. Based on the TLS model, the TLS-induced loss tends to saturate at high temperatures [58, 75] as shown in Fig. 2.6(d). By fitting to the TLS model using Equation 2.17, we obtain a $F\delta_{\mathrm{TLS}}$ of 0.44 ppm in accord with the power scan.

The above results agree with previous findings [70, 71, 115] that the MA interface is one of the main sources of TLS loss. In our study, we have employed a small CPW gap, which results in a significantly higher concentration of electric field inside the trenches of the CPW, therefore maximizing the coupling with the TLS fluctuators at the interfaces of the material as well as resulting in a larger filling factor value [51, 133]. Hence, devices with larger features [70] would reduce this filling factor and electric field density thereby reducing $F\delta_{\mathrm{TLS}}$ by nearly one order of magnitude as well as yielding higher internal quality factors [51, 58].

To conclude, we have refined a method to deposit extremely low-loss niobium films for superconducting CPW resonators using a UHV electron-beam evaporator. With post-cleaning of the Nb surface, devices demonstrated loss tangents well-below previous limits, highlighting the role of the MA interface as one of the main sources of loss in superconducting devices. Moreover, the characterization results show a significant reduction in the surface oxide thickness, verifying the efficacy of our cleaning method. Future work may explore a practical passivation scheme to bypass the MA interface-induced losses for the fabrication of highly coherent superconducting qubit processors.

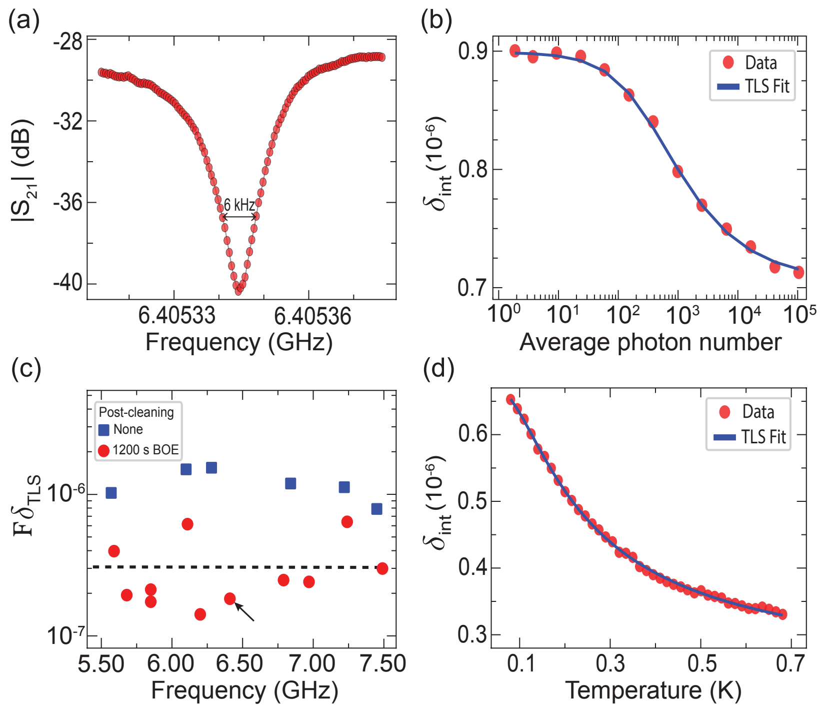

Figure 2.6: Microwave measurement results of the fabricated resonators. (a) The transmission of a resonator near resonance. (b) The internal loss of the resonator indicated with an arrow in (c) as a function of the average photon number present in the resonator. (c) The $F\delta_{\text{TLS}}$ of 17 resonators with and without post-cleaning. (d) The internal loss as a function of the temperature for the indicated resonator. This figure is adapted from [44].

Chapter 3

Theory of Open Quantum Systems

3.1 Quantum system dynamics

Studying the evolution of the quantum systems allows us to explore intriguing features. For instance, in the presence of a weak interaction with the environment, the system's evolution is governed by a non-unitary superoperator, giving rise to dynamics deviating from closed system Schrödinger equation governed evolution. The dynamics can be further generalized by stepping into a region where there is a strong interaction between the system and the environment. In some cases, such an open system exhibits memory effects. This section starts by formulating the dynamics of both closed and open quantum systems. Then I move onto the detailed description of dynamics in a non-Markovian open quantum system and the various methods used to quantify the non-Markovianity of a system.

3.1.1 Closed system dynamics

In the absence of dissipation channels, the dynamics of a quantum system is governed by the well-known Liouville von-Neumann equation. To derive such dynamics, we can start by the Schrödinger equation given as,

$$i\hbar \frac{d}{dt}|\psi(t)\rangle = H(t)|\psi(t)\rangle, \tag{3.1}$$

where $\hbar$ is the reduced Planck's constant, $|\psi(t)\rangle$ represents the state of the system at time t, and $H(t)$ denotes the time-dependent Hamiltonian of the system. For simplicity, $\hbar$ is set to one for the rest of this chapter.

The solution of Eq. 3.1 can be written in terms of a unitary operator, describing the evolution of the system with the initial time t_0. This operator relates the state of the system at two different time steps as,

$$|\psi(t)\rangle = U(t, t_0)|\psi(t_0)\rangle. \tag{3.2}$$

Substituting Eq. 3.2 into 3.1, we can solve for the unitary operator as,

$$U(t, t_0) = \mathcal{T} \exp(-i \int_{t_0}^{t} H(s)\, ds), \tag{3.3}$$

where $\mathcal{T}$ is the time-ordering operator, which orders the product of the time-dependent operators.

Assuming a state initialized at t_0 in the form of,

$$\rho(t_0) = \sum_j a_j |\psi_j(t_0)\rangle\langle\psi_j(t_0)|, \tag{3.4}$$

with a_j indicating the weight of state $|\psi_j\rangle$, we can write the time evolution of such a state using Eq. 3.2 as,

$$\rho(t) = U(t, t_0)\rho(t_0)U^\dagger(t, t_0). \tag{3.5}$$

Note that the density matrix, ρ, is positive, self-adjoint and has a unit trace by definition [134]. Now by taking the time derivative of Eq. 3.5, we obtain the well-known Liouville von-Neumann equation,

$$\frac{d}{dt}\rho(t) = -i[H(t), \rho(t)]. \tag{3.6}$$

To generalize the Liouville von-Neumann equation, we take into account a number of systems interacting with each other. This results in a more complicated Hamiltonian in the form of,

$$H(t) = H_0 + H_I(t). \tag{3.7}$$

Here, H_0 is the Hamiltonian of the systems in the absence of the interactions and $H_I(t)$ represents the time-dependent interaction Hamiltonian. To solve for the evolution of such

Hamiltonian, we move to the interaction picture as follows. Considering the unitary evolution of the total Hamiltonian as $U(t, t_0)$, the unitary operator evolution in the interaction picture is then given by,

$$U_I(t, t_0) = U_0^\dagger(t, t_0)U(t, t_0), \tag{3.8}$$

where $U_0^\dagger(t, t_0) = \exp(-iH_0(t - t_0))$ represents the time evolution of the system, excluding the interactions.

Using Eq. 3.8, the density matrix in the interaction picture is given as,

$$\rho_I(t) = U_I(t, t_0)\rho(t_0)U_I^\dagger(t, t_0). \tag{3.9}$$

Taking the time derivate of the density matrix $\rho_I(t)$, leads us to the von-Neumann equation in the interaction picture,

$$\frac{d}{dt}\rho_I(t) = -i[H_I'(t), \rho_I(t)], \tag{3.10}$$

where the interaction Hamiltonian in the interaction picture is given as, $H_I'(t) = U_0^\dagger(t, t_0)H_I U_0(t, t_0)$.

3.1.2 Presence of the environment

In spite of the previous case, here we examine the evolution of an open quantum system coupled to a bath. Therefore, in addition to the evolution of the closed state, alone, we need to take into account the dissipations caused by the coupling to the environment. The evolution of such an open system under certain approximations that we discuss later, is governed by the well-known Gorini-Kossakowski-Sudarshan-Lindblad (GKSL) master equation [135, 136]. The main reason behind applying these approximations is to simplify the calculations of the dynamics of a system where the bath can have large degrees of freedom. For a system coupled to a bath with Hamiltonians denoted by, H_S and H_B, the total Hamiltonian of the coupled system in the system and bath Hilbert space ($H_S \otimes H_B$) is written as,

$$H(t) = H_S \otimes \mathcal{I}_B + \mathcal{I}_S \otimes H_B + H_I(t), \tag{3.11}$$

where $H_I(t)$ represents the interaction Hamiltonian of the system and bath.

The dynamics of the singled out system is given by tracing out the bath degrees of freedom,

$$\rho_S(t) = \mathrm{Tr}_B(\rho_{SB}(t)), \tag{3.12}$$

with ρ_{SB} representing the total density matrix of the coupled system and the partial trace over the environment is defined as,

$$\mathrm{Tr}_B(\rho_S B) = \sum_j \rho_S \otimes \langle \psi_{B_j} | \rho_B | \psi_{B_j} \rangle, \tag{3.13}$$

where ψ_{B_j} represents the state of the environment. Furthermore, the evolution of the system after tracing out the environment is given by the von-Neumann equation as,

$$\frac{d}{dt}\rho_S(t) = \mathrm{Tr}_B(-i[H(t), \rho_{SB}(t)]). \tag{3.14}$$

Now we examine the required approximations that lead us to the GKSL master equation. To commence, we solve for the density matrix with all the operators defined in their interaction picture using Eq. 3.10 as,

$$\rho_{SB}(t) = \rho_{SB}(t_0) - i \int_{t_0}^{t} ds [H_I(s), \rho_{SB}(s)]. \tag{3.15}$$

Substituting Eq. 3.15 into the von-Neumann equation and tracing over the environment with the assumption that $\mathrm{Tr}_B([H_I(t), \rho_{SE}(t_0)]) = 0$, we get,

$$\frac{d}{dt}\rho_S(t) = -\int_{t_0}^{t} ds \mathrm{Tr}_B([H_I(t), [H_I(s), \rho_{SB}(s)]]). \tag{3.16}$$

First approximation to simplify Eq. 3.16 is known as the *Born approximation.* It states that assuming a weak coupling between the system and the environment, the density matrix of the whole system is separable at all times with the environment state being unchanged during the entire evolution, $\rho_{SB}(t) \simeq \rho_S(t) \otimes \rho_B$.

Next, we have the *first Markov approximation* where we neglect all the memory effects caused by the environment and assume that the reduced density matrix of the system is not changing over time. To elaborate, this implies that the state of the system is not dependent on the history of the evolution ($\rho_S(s) \sim \rho_S(t)$). Implementing these two approximations in Eq. 3.16 leads us to a simpler master equation,

$$\frac{d}{dt}\rho_S(t) = -\int_{t_0}^{t} ds \mathrm{Tr}_B([H_I(t), [H_I(s), \rho_S(t) \otimes \rho_B]]). \tag{3.17}$$

This relation is commonly known as the Redfield master equation [137]. Even though that the Redfield equation is local in time, the dependency of its choice of an initial state at time t_0 prevents it from being considered as a Markovian master equation. Thereby, additional approximations need to be implemented.

In the case where the time scale of the system over which the system evolves, τ_S, is much larger than that of the environment, $\tau_S \gg \tau_B$, we can incorporate the *second Markov approximation*. To this end we perform a change of variable and replace s with $t - s$ in the integrand of Eq. 3.17 and change the integration's upper limit to infinity. This yields the Markovian master equation in the form of,

$$\frac{d}{dt}\rho_S(t) = -\int_{0}^{\infty} ds \mathrm{Tr}_B([H_I(t), [H_I(t), \rho_S(t) \otimes \rho_B]]). \tag{3.18}$$

The set of the described approximations above is known as the *Born-Markov approximation*. Moving on toward deriving the GSKL master equation, one applies a secular approximation, where we neglect the fast-oscillating terms. We start by introducing the interaction Hamiltonian in the laboratory frame as,

$$H_I = \sum_{\alpha} A_\alpha \otimes B_\alpha, \tag{3.19}$$

where A_α and B_α are arbitrary Hermitian operators denoting acting on the system and bath.

The system operators can be decomposed using the eigenvectors ($|\epsilon\rangle$) of the system Hamiltonian H_S as,

$$A_\alpha(\omega) = \sum_{\epsilon' - \epsilon = \omega} |\epsilon\rangle\langle\epsilon|A_\alpha|\epsilon'\rangle\langle\epsilon'|. \tag{3.20}$$

Here, we sum over all energy eigenvalues ϵ and ϵ' with a fixed energy difference of ω. Moreover, using the completeness of these operators, we can write the interaction Hamiltonian in the interaction frame as,

$$H_I(t) = \sum_{\alpha,\omega} e^{-i\omega t} A_\alpha(\omega) \otimes B_\alpha(t) = \sum_{\alpha,\omega} e^{i\omega t} A_\alpha^\dagger(\omega) \otimes B_\alpha^\dagger(t). \tag{3.21}$$

Now, substituting Eq. 3.21 into the Markovian master equation derived earlier (Eq. 3.18), we get,

$$\begin{aligned}\frac{d}{dt}\rho_S(t) &= \int_0^\infty ds \mathrm{Tr}_B\{H_I(t-s)\rho_S(t)\rho_B H_I(t) - H_I(t)H_I(t-s)\rho_S(t)\rho_B\} + \text{h.c.} \\ &= \sum_{\omega,\omega'}\sum_{\alpha,\beta} e^{i(\omega'-\omega)}\Gamma_{\alpha\beta}(\omega)(A_\beta(\omega)\rho_S(t)A_\alpha^\dagger(\omega') - A_\alpha^\dagger(\omega')A_\beta(\omega)\rho_S(t)) + \text{h.c.}, \end{aligned} \tag{3.22}$$

where h.c. denotes the Hermitian conjugate and $\Gamma_{\alpha\beta}$ is the Fourier transform of the environment's correlation functions as,

$$\Gamma_{\alpha\beta} = \int_0^\infty ds e^{i\omega s}\langle B_\alpha^\dagger(t)B_\beta(t-s)\rangle, \tag{3.23}$$

with the correlation function defined as, $\langle B_\alpha^\dagger(t)B_\beta(t-s)\rangle = \mathrm{Tr}_B(B_\alpha^\dagger(t)B_\beta(t-s)\rho_B)$.

Due to the weak coupling between the system and the environment and the short time scale of the environment discussed earlier, we can apply a rotating wave approximation and omit the non-secular terms (any term proportional to $\exp[i(\omega'-\omega)t]$ with $\omega \neq \omega'$) in Eq. 3.22, which results in,

$$\frac{d}{dt}\rho_S(t) = \sum_{\omega}\sum_{\alpha,\beta}\Gamma_{\alpha\beta}(\omega)(A_\beta(\omega)\rho_S(t)A^\dagger(\omega) - A_\alpha^\dagger(\omega)A_\beta(\omega)\rho_S(t)) + \text{h.c.} \tag{3.24}$$

Defining $\gamma_{\alpha\beta}(\omega) = \Gamma_{\alpha\beta}(\omega) + \Gamma^*_{\beta\alpha}(\omega)$ and $S_{\alpha\beta} = 1/2i(\Gamma_{\alpha\beta}(\omega) - \Gamma^*_{\beta\alpha}(\omega))$, leads to,

$$\frac{d}{dt}\rho_S(t) = -i[H_{LS}, \rho_S(t)] + \sum_{\omega}\sum_{\alpha,\beta}\gamma_{\alpha\beta}(\omega)\Bigg(A_\beta(\omega)\rho_S(t)A^\dagger_\alpha(\omega) - \frac{1}{2}\{A^\dagger_\alpha(\omega)A_\beta(\omega), \rho_S(t)\}\Bigg), \tag{3.25}$$

where the Lamb shift Hamiltonian is given as,

$$H_{LS} = \sum_{\omega}\sum_{\alpha,\beta} S_{\alpha\beta}(\omega)A^\dagger_\alpha(\omega)A_\beta(\omega). \tag{3.26}$$

Finally, diagonalizing the $\gamma_{\alpha\beta}(\omega)$ terms in Eq. 3.25 leads us to the long-sought GKSL master equation given as,

$$\frac{d}{dt}\rho_S(t) = -i[H_{LS}, \rho_S(t)] + \sum_k \gamma_k(L_k\rho_S(t)L^\dagger_k - \frac{1}{2}\{L^\dagger_k L_k, \rho_S(t)\}), \tag{3.27}$$

with L_k denoting the Lindblad jump operators.

The GKSL master equation can be simplified into a single non-Hermitian operator known as the Liouvillian super-operator, $\mathcal{L}$, written as [138],

$$\frac{d}{dt}|\rho_S(t)\rangle\rangle = \mathcal{L}(t)|\rho_S(t)\rangle\rangle, \tag{3.28}$$

where $|\cdot\rangle\rangle$ represents a super-ket in the Fock-Liouville space.

The main reason behind rearranging the GKSL equation in this form is to define a completely-positive trace-preserving (CPTP) map using the Liouvillian super-operator to link the density matrix at various time steps as, $\rho_S(t) = \Lambda_{t,t_0}\rho_S(t_0)$, where $\Lambda_{t,t_0} = \exp[\mathcal{L}(t-t_0)]$. Furthermore, the CPTP condition of this map can be also guaranteed if it is divisible such that,

$$\Lambda_{t_3,t_1} = \Lambda_{t_3,t_2}\Lambda_{t_2,t_1}, \tag{3.29}$$

with $0 \leq t_1 \leq t_2 \leq t_3$. This condition holds for Markovian processes where the system satisfies the condition, $\gamma_k \geq 0$ over the entire evolution.

3.1.3 Beyond the Markov approximation

To account for the memory effects in the real-world open systems, we need to generalize the GKSL master equation (Eq. 3.27). Nakajima and Zwanzig formulated a master equation that governs the dynamics of such open systems [139, 140]. The memory effects arise once we move onto the regime where there is a strong coupling between the system and the environment. In this regime, the Born-Markov approximation is not any longer applicable and the system reaches a non-Markovian regime with the memory effects relating all the history of the evolution at each time step. In this section, we take the projection operator approach to derive the Nakajima-Zwanzig master equation proposed in [141].

We start the derivation of the non-Markovian master equation by introducing the Hamiltonian of the coupled system as,

$$H = H_0 + \alpha H_I, \tag{3.30}$$

where H_0 and H_I are the free evolution and the interaction Hamiltonians with α representing a dimensionless expansion parameter. The equation of motion in the interaction picture is given as,

$$\frac{d}{dt}\rho(t) = -i\alpha[H_I(t), \rho(t)] = \alpha\mathcal{L}(t)\rho(t). \tag{3.31}$$

We define two projection super-operators in the form of,

$$\mathcal{P}\rho = \mathrm{Tr}_B(\rho) \otimes \rho_B, \tag{3.32}$$

$$\mathcal{Q}\rho = \rho - \mathcal{P}\rho. \tag{3.33}$$

Here, projection $\mathcal{P}\rho$, gives all the necessary information required to reconstruct the reduced density matrix of the system, ρ_S. On the other hand, the complementary super-operator, $\mathcal{Q}$ acts on the irrelevant part of the density matrix, meaning that the result is not useful in reconstructing ρ_S.

Following the definition of these super-operators, we can immediately see their properties,

$$\begin{aligned}
&\mathcal{P} + \mathcal{Q} = \mathcal{I}, \\
&\mathcal{P}^2 = \mathcal{P}, \\
&\mathcal{Q}^2 = \mathcal{Q}, \\
&\mathcal{P}\mathcal{Q} = \mathcal{Q}\mathcal{P} = 0.
\end{aligned} \tag{3.34}$$

Applying the super-operator projectors (Eq. 3.32 and 3.33) to the von-Neumann equation (Eq. 3.31) and inserting the identity operator between the Liouvillian super-operator and the density matrix on the right hand side, leads to a coupled differential equation system,

$$\frac{d}{dt}\mathcal{P}\rho(t) = \alpha\mathcal{P}\mathcal{L}(t)\mathcal{P}\rho(t) + \alpha\mathcal{P}\mathcal{L}(t)\mathcal{Q}\rho(t), \tag{3.35}$$

$$\frac{d}{dt}\mathcal{Q}\rho(t) = \alpha\mathcal{Q}\mathcal{L}(t)\mathcal{P}\rho(t) + \alpha\mathcal{Q}\mathcal{L}(t)\mathcal{Q}\rho(t). \tag{3.36}$$

To arrive at the master equation, we need to solve Equation 3.36 and insert the solution to 3.35. The solution then is given as,

$$\mathcal{Q}\rho(t) = \mathcal{G}(t, t_0)\mathcal{Q}\rho(t_0) + \alpha\int_{t_0}^{t} ds\mathcal{G}(t, s)\mathcal{Q}\mathcal{L}(s)\mathcal{P}\rho(s), \tag{3.37}$$

where the propagator is defined as,

$$\mathcal{G}(t, s) = \tau \exp\left[\alpha\int_{s}^{t} ds'\mathcal{Q}\mathcal{L}(s')\right], \tag{3.38}$$

where τ is the time-ordering operator.

At last, inserting Eq. 3.37 into 3.35 leads us to the Nakajima-Zwanzig equation,

$$\begin{aligned}\frac{d}{dt}\mathcal{P}\rho(t) = \alpha\mathcal{P}\mathcal{L}(t)\mathcal{G}(t,t_0)\mathcal{Q}(t_0)\rho(t_0) + \alpha\mathcal{P}\mathcal{L}(t)\mathcal{P}\rho(t)& \\ + \alpha^2\int_{t_0}^{t} ds\mathcal{P}\mathcal{L}(t)\mathcal{G}(t,s)\mathcal{Q}\mathcal{L}(s)\mathcal{P}\rho(s).&\end{aligned} \tag{3.39}$$

Next, we define the memory kernel super-operator as,

$$\mathcal{K}(t,s) = \alpha^2\mathcal{P}\mathcal{L}(t)\mathcal{G}(t,s)\mathcal{Q}\mathcal{L}(s)\mathcal{P}, \tag{3.40}$$

and rearrange the terms in Equation 3.39 we get,

$$\frac{d}{dt}\mathcal{P}\rho(t) = \alpha\mathcal{P}\mathcal{L}(t)\mathcal{P}\rho(t) + \int_{t_0}^{t} ds\mathcal{K}(t,s)\mathcal{P}\rho(s) + \alpha\mathcal{P}\mathcal{L}(t)\mathcal{G}(t,t_0)\mathcal{Q}(t_0)\rho(t_0). \tag{3.41}$$

The first term in Eq. 3.41, gives rise to the Markovian master equation derived in the previous section. More interestingly, this equation explains the memory effects of the system given by the second term consisting of the memory kernel super-operator integrated over the entire evolution. This is the essence behind non-Markovian open system dynamics where the current state of the system is dependent on the entire history of the evolution. Finally, the last term denotes an inhomogeneous term dependent on the initial condition at t_0.

It is easy to see that, under the assumption of having a separable initial state, $\rho(t_0) = \rho_S(t_0) \otimes \rho_B$, the inhomogeneous term $(\mathcal{P}\mathcal{L}(t)\mathcal{G}(t,t_0)\mathcal{Q}(t_0)\rho(t_0))$ vanishes as $\mathcal{Q}\rho(t_0) = 0$.

In addition to this assumption, if we replace the memory kernel with a delta function, $\mathcal{K}(t,s) \sim \delta(t-s)$, we can recover the Markovian master equation (Eq. 3.28) independent of the history of the system.

In order to reconstruct the general master equation (Eq. 3.41) of an open system, first we need to utilize quantum process tomography (QPT) [142] to find the quantum dynamical maps for each time step. The transfer tensors can then be constructed between any two arbitrary time steps using the calculated dynamical maps [143]. Finally, all the terms in Eq. 3.41 can be written in terms of the transfer tensors with the approximation of large number of time steps [144].

3.2 Measures of non-Markovianity

The memory effects of an open system can be quantified by examining the evolution of the system. Thereby, measuring the non-Markovianity of a system is typically achieved by either studying the distinguishability of two distinct initial states over time or by examining the evolution of an initially entangled state in the presence of the system and environment interactions. This section discusses both of these methods in details as well as reviewing the common entanglement measures to quantify the separability of a density matrix.

3.2.1 Distinguishability

Proposed by Breuer et. al. in 2009 [30], the trace distance method has been the most common measure of the non-Markovianity of an open system due to its ease of implementation.

The main idea behind this method is to study the distinguishability of two separately prepared states. In the case of having a non-Markovian bath, there will be a back-flow of information from the environment back to the system due to the memory effects discussed in Section 3.1.3. This means that unlike the Markovian case where the distinguishability monotonically decreases over time, the distinguishability of the states can be increased over time. This phenomenon is used to quantify the non-Markovianity of the system.

To formulate this method, we start by introducing the trace distance of two arbitrary density matrices, ρ_1 and ρ_2 as [145],

$$D(\rho_1, \rho_2) = \frac{1}{2}\mathrm{Tr}(|\rho_1 - \rho_2|), \tag{3.42}$$

where $|\rho| = \sqrt{\rho^\dagger \rho}$. This measure is bounded as $0 \leq D(\rho_1, \rho_2) \leq 1$, where the upper bound is only satisfied when the states are orthogonal with the other bound achieved once the states are both identical.

Putting the mathematical equation aside, there is an interesting physical intuition behind the trace distance. Considering two parties, Alice and Bob, where Alice prepares two distinct states marked as, ρ_1 and ρ_2, each with equal probabilities of 1/2 and transfers them to Bob through a noisy quantum channel denoted by a CPTP map, Λ_t, evolving the initial states to time t (Fig. 3.1). Now the task for Bob is to measure the states and try to distinguish between the two. It can be shown that the probability that Bob can distinguish these two is given as,

$$\mathrm{P_d}(\rho_1, \rho_2) = \frac{1}{2}(1 + D(\Lambda_t(\rho_1), \Lambda_t(\rho_2))). \tag{3.43}$$

Hence, the trace distance is directly proportional to the distinguishability of the states and a good measure of the non-Markovianity of an open system. As it can be seen, the distinguishing probability is equal to one if the two state are orthogonal. Note that one of the key characteristics of a non-Markovian system is the non-divisibility of its dynamical maps at various times [30].

Moving onwards with the derivation of the measure, as we mentioned earlier contingent on the degree of the present memory effects in the system, the distinguishability of the states may increase. Therefore, the trace distance of two distinct states may increase over time as it is gone through a quantum channel during the evolution, $D(\rho_1, \rho_2) \leq D(\Lambda_t(\rho_1), \Lambda_t(\rho_2))$. To account for this increase in the distinguishability of the system, we utilize the derivative of the trace distance and integrate over all the regions that we have a positive derivative. Thus, the non-Markovianity measure is defined as,

$$\mathcal{N}(\Lambda) = \max_{\rho_1, \rho_2} \int_{\dot{D}>0} dt \frac{d}{dt} D(\Lambda_t(\rho_1), \Lambda_t(\rho_2)). \tag{3.44}$$

with $\dot{D}$ denoting the time derivative of the trace distance and we integrate over the two distinct states that result in the maximum non-Markovianity. In a separate work, Wißmann et. al. [146] prove theoretically that choosing two orthogonal initial states ensures the optimal outcome of this measure.

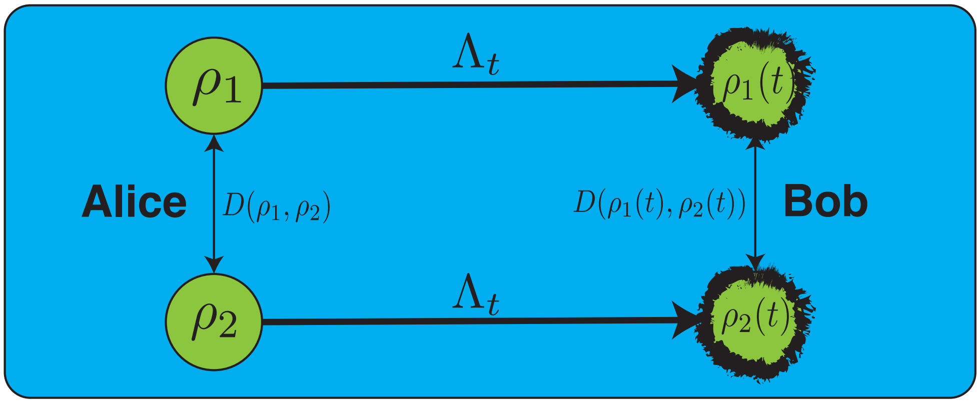

Figure 3.1: State distinguishability scheme with two distinct initial states subjected to a noisy quantum channel [147].

3.2.2 Entanglement

Perhaps the most intriguing and mysterious aspect of the quantum mechanics is entanglement. This phenomenon implies that the measurement on one of the entangled particles, simultaneously affects the state of the other particle no matter how much they are separated from each other. This has also significant potential in the field of secure quantum telecommunication, where we try to transmit the data with the least chance that the data can be eavesdropped during the transmission [148].

An entangled state is the one that cannot be written as a separable product state of multiple states, e.g. for a two-qubit system,

$$|\psi\rangle = |\psi_1\rangle \otimes |\psi_2\rangle. \tag{3.45}$$

On the other hand, an entangled state occurs when we have a superposition of multi-qubit, correlated states. The simplest form of an entangled state for a two-qubit system is given as,

$$|\psi_B\rangle = \frac{1}{\sqrt{2}}(|01\rangle + |10\rangle). \tag{3.46}$$

It is easy to see that it is impossible to rewrite this state as a separable state (Eq. 3.45). This state is maximally entangled and is commonly known as one of the four Bell states. To elaborate, measuring the first qubit will give us a 50% chance of being in $|0\rangle$ or $|1\rangle$ state, preventing us from predicting the projected state of the qubit, which is the essence of entanglement in quantum systems.

Concurrence

To quantify the degree of entanglement, one can choose among various well-known measures such as, von-Neumann entropy [145], CHSH measure [149], or logarithmic negativity [150]. In this work, we use a tomographic method suitable for experiments known as the concurrence.

The concurrence $\mathcal{C}$, proposed by Wooters in 1998 [151], is an entanglement measure based on the tomographically reconstructed density matrix ρ. One main advantage of the concurrence over the other measures, like the von-Neumann entropy is that this measure takes into account the entire subdivisions of the system space. Hence, having a non-zero concurrence assures the presence of entanglement in the system.

In this formalism, we make use of the spin flip transformation given as,

$$|\tilde{\psi}\rangle = \sigma_y|\psi^*\rangle, \tag{3.47}$$

where $|\psi^*\rangle$ represents the complex conjugate of the system state and σ_y is the Pauli-y operator. For a two-level system this is identical to the time reversal operation and indeed flips the state of $|\psi\rangle$ [33]. Extending this formalism to a two-qubit system, we can write the flipped density matrix as,

$$\tilde{\rho} = (\sigma_y \otimes \sigma_y)\rho^*(\sigma_y \otimes \sigma_y). \tag{3.48}$$

Defining a new matrix, $M = \rho\tilde{\rho}$, leads us to the concurrence formulated as,

$$\mathcal{C}(\rho) = \max\{0, \sqrt{\lambda_1} - \sqrt{\lambda_2} - \sqrt{\lambda_3} - \sqrt{\lambda_4}\} \tag{3.49}$$

where $\lambda_1, ..., \lambda_4$ are the eigenvalues of M matrix sorted in the decreasing order. The spin-flip transformation projects the state into an orthogonal state, hence setting M to zero. However, an entangled state is invariant under this transformation, which gives rise to a non-zero concurrence. This definition bounds the concurrence as, $0 \leq \mathcal{C} \leq 1$, with a maximally entangled state having a concurrence of one.

Entanglement revival

We introduce a measure for the non-Markovianity of the system based on the evolution of the entanglement. As known, having a CPTP map does not result in a revival of the entanglement. Hence, for a Markovian environment the entanglement monotonically decays over time [152]. However, if we move onto a regime where there is a strong coupling between the system and the environment, there is a chance that the entanglement can be revived due to the memory effects induced by the environment discussed in Section 3.1.3.

The main advantage of utilizing entanglement as a probe of the memory in an open system is that there is no need to have prior knowledge about the dynamics of the system as well as avoiding an optimization problem, such the trace distance measure introduced in Sec. 3.2.1 where we need to find an optimal set of initial states. This method was first proposed by Rivas et. al. [31], where they theoretically studied the entanglement evolution of an open system coupled to a bath of harmonic oscillators. In their proposal, they considered a two-level system coupled to an ancilla with the system, alone, being coupled to a bath of oscillators. Figure 3.2(a) shows their proposed scheme with the bath indicated by the golden color. The main idea is to prepare the system and ancilla in an entangled state at t_0 and let the system evolve by having interactions with the bath.

The entanglement measure over the entire time evolution of the system is formulated as,

$$\mathcal{I}^{(E)} = \int_{t_0}^{t_f} \left| \frac{d\mathcal{C}[\rho_{SB}(t)]}{dt} \right| dt - \Delta\mathcal{C}, \tag{3.50}$$

where $\mathcal{C}$ denotes the concurrence (Eq. 3.49) and $\Delta\mathcal{C} = \mathcal{C}[\rho_{SB}(t_0)] - \mathcal{C}[\rho_{SB}(t_f)]$. It is clear that for a Markovian bath the slope of the entanglement over time is always decreasing over time, resulting in a zero measure (green curve in Fig. 3.2(b)). However, they showed that by increasing the coupling between the system and bath, the entanglement can be revived over time, due to the back-flow of information from the environment (red curve in Fig. 3.2(b)). Thereby, this measure is a great tool to quantify the non-Markovianity of the system. In the next chapter, we will discuss an experiment where we utilize this measure to probe the memory effects of the environment.

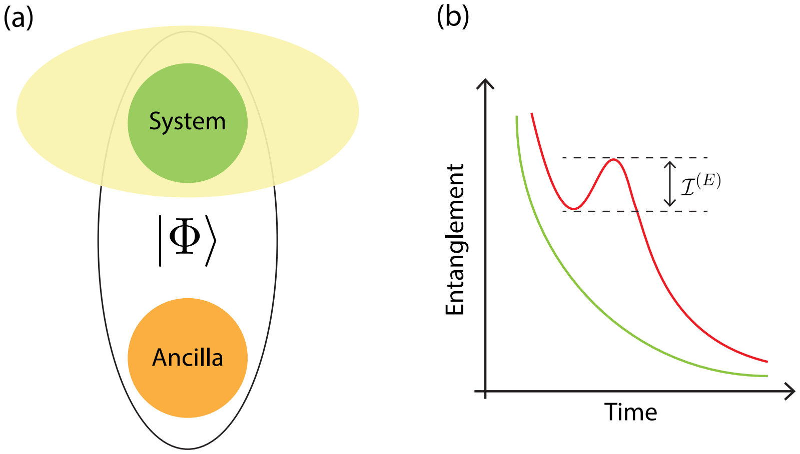

Figure 3.2: (a) A cartoon explaining the scheme behind realizing the non-Markovianity in an open quantum system. (b) The evolution of an entangled state in the presence of a (non-)Markovian environment represented by (red) green curve [31].

Chapter 4

Realizing Non-Markovian Dynamics in Superconducting Qubit Processors

This chapter discusses in detail the most sophisticated experiment conducted in Murch lab to date on the realization of an open quantum system with memory. I start with giving an overview of the project and the motivations behind the study of the memory in open systems. I will then go over the toolset required to design multi-qubit superconducting circuits to realize a Hamiltonian of interest in Section 4.2. Section 4.3 covers the basics of microwave engineering required for setting up cryogenic experiments and after that I will move onto the two-qubit tomography (Sec. 4.4) and the cross-resonance gate (Sec. 4.5) to entangle two qubits using an all-microwave gate scheme. At last, I will conclude the chapter by presenting the results and the future plausible paths for this project in Section 4.6.

4.1 Retrieval of entanglement

Essentially for any experiment conducted in a laboratory, there is always an inevitable interaction between the system and its environment. The environment can be the main source of decoherence properties in the system with its dynamics described by the Lindbaldian master equation under Born-Markov approximations, as discussed in Section 3.1.2. Nonetheless, one can take advantage of the environment and utilize it to resolve challenges, such as the measurement problem, where we use the environment to probe the state of the system. However, having a strong interaction between the system and environment results in the violation of the Born-Markov approximations. In this case, the system will experience a back-flow of information from its environment with its dynamics described by the generalized master equation (Sec. 3.1.3), which takes into account the impact of the memory in the environment by linking the current state of the system to all of its precedent history over time in terms of a memory kernel. This allows us to study exhilarating physical phenomena, e.g., the state retrieval [153], a better understanding of the temporally correlated noise in multi-qubit circuits hindering the progress towards achieving a fault-tolerant quantum computer [28, 154, 155], and the study of the memory kernel [144, 156] merely present in non-Markovian open systems.

Among various measures of the non-Markovianity ranging from trace distance [30] to operational approaches [157], the entanglement measure proposed in 2010 by Rivas et. al. [31] is of great importance due to its direct applications in quantum algorithms, such as superdense coding. The main goal of this algorithm is to transmit an entangled state between two parties using only one qubit. It has been shown that introducing non-Markovian noise and memory effects improves the efficiency of this algorithm [158, 159]. Expanding on the entanglement measure scheme, the system is initially entangled to an ancilla qubit and the system itself is coupled to a bath of harmonic oscillators with the non-Markovian transition achieved by increasing the coupling rate to the bath. In that regime, one can experience a retrieval of the entangled state over its course of evolution in time. To elaborate on that, due to the back-flow of information from the environment, the dissipated information can be recaptured contingent on having a strong interaction between the system and environment. Although this phenomenon has been previously explored in the optical platforms [160], the lack of such experimental study in the rapidly evolving field of the superconducting qubits has inspired this work.

4.2 Design and simulation of multi-qubit processors

The first step in realizing non-Markovian dynamics in a real-world experiment is to design and simulate a superconducting qubit processor backed by the parameters extracted from the numerical solutions of the desired Hamiltonian. This section starts with covering the basics of the numerical simulations by introducing the required toolset and moves onto designing and simulation of the multi-qubit processors.

4.2.1 Numerical simulations

The simplest approach to check the feasibility of a theory is by numerically solving for the density matrix evolution of the system using the master equations discussed in Chapter 3 using conventional numerical ordinary differential equation methods, such as the Runge-Kutta [161] or take a different route and use a Monte Carlo method where we examine the quantum trajectories to find a solution to the master equation utilizing the well-known quantum jump method first introduced in the field of quantum optics [162]. Either way, the solution should represent the dynamics of the system with the lowest possible cost compared to conducting the experiment and showcase the results as a benchmark and inception of a complex project.

Recently, there has been a significant rise in the number of packages capable of solving the dynamics of open quantum systems in the presence of dissipation. Among those, the `QuTiP` [163, 164] and `HOQST` [165] packages have received the most attention. The main advantage of `HOQST` is its ability to simulate the dynamics in the presence of various noise models as well as being based on Julia programming language, which is capable of solving differential equations about two times faster than python-based packages. In spite of that, `QuTiP` has the largest number of users due to the fact that it is based on python where most people have prior knowledge of the language. Likewise, in our study we utilize the `QuTiP` package to examine the dynamics of our system of interest.

As discussed in the previous section, to realize non-Markovian open quantum systems we need to make use of a quantum processor with three coupled qubits (two coupled pairs) where the third qubit can be taken into account as the environment of the system qubit (Fig. 4.1).

The Hamiltonian of such a system with qubits mediated via a co-planar waveguide resonator is in the form of,

$$H = \frac{1}{2}\sum_{i=0}^{2}\omega_i Z_i + J_{\mathrm{SA}}\ X \otimes X \otimes I + J_{\mathrm{SE}}\ I \otimes X \otimes X, \tag{4.1}$$

with J_{SA} and J_{SE} denoting the coupling rate between the system-ancilla and system-environment qubits and ω_i represents the resonant frequency of qubit i.

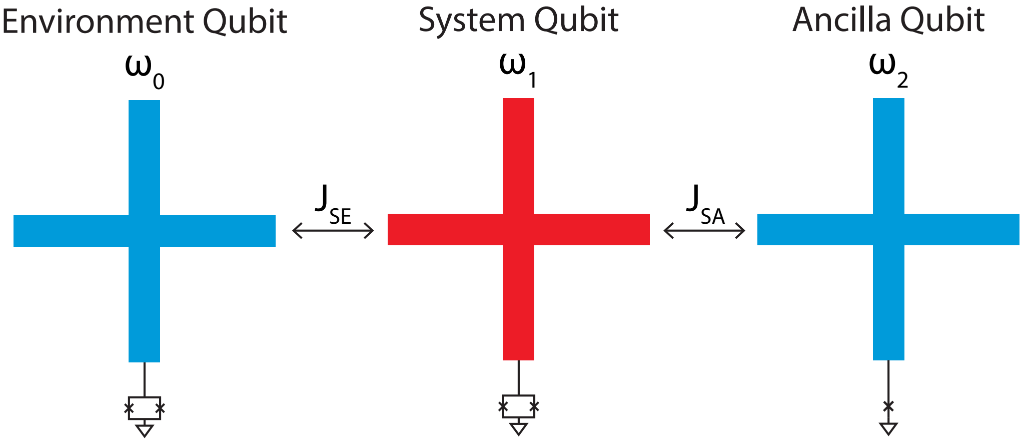

Figure 4.1: Cartoon demonstrating the main idea behind the three-qubit processor design.

Using the `mesolve` function in the `QuTiP` package, we can simply extract all the expectation values required to reconstruct the two-qubit density matrix at each timestep. First, we initialize the system and ancilla qubits in a Bell state (concurrence = 1) and then look at the evolution of the entanglement. As shown in Figure 4.2(a, b), the oscillations in concurrence gets weaker as we increase the detuning between the system and environment qubits for the simulation parameters assigned as follows: $\omega_1/2\pi = 4.24$ GHz, $\omega_2/2\pi = 4.5$ GHz, $J_{\mathrm{SA}}/2\pi =$

1.1 MHz, and $J_{\mathrm{SE}}/2\pi = 2$ MHz. In addition, the non-Markovianity of the system is calculated using Equation 3.50. Figure 4.2(c) illustrates the transition from non-Markovian to Markovian regime by varying the tuning between the system and environment qubits.

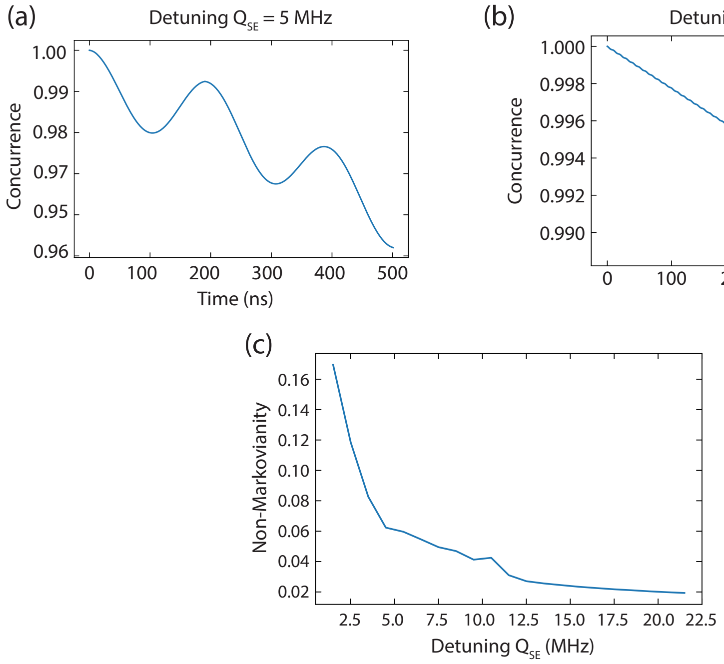

Figure 4.2: Numerical simulation results of the concurrence evolution for system-environment detunings of (a) 5 MHz and (b) 100 MHz. (c) The non-Markovianity of the system as a function of the detuning between the system and environment qubits.

4.2.2 Device design

Having all the desired parameters from the numerical simulations allows us to move onto the next step, where we need to run electromagnetic simulations to determine the actual device parameters, such as the Josephson junction's inductance and the capacitance, to bring our desired Hamiltonian (Eq. 4.1) into life by designing intricate superconducting circuits. I start by introducing the theory background on the main simulation tool proposed by Minev et al. [166] and then discuss the practicality of this theory in building multi-qubit circuits.

Energy-participation ratio

The main challenge in experimentally realizing various Hamiltonians is to have reliable, efficient, and accurate simulation tools to precede the fabrication steps. The most prominent simulation tool developed to simulate the multi-qubit complex circuits is known as the energy-participation ratio (EPR) quantization [166]. The main idea behind this method is to find the energy ratio of mode m stored in element j denoted p_{mj}. As shown later in this section, this ratio is the main element in bridging classical and quantum circuit analysis.

To elucidate how EPR works, we can look at a simple example where we have a flux tunable transmon qubit capacitively coupled to a microwave cavity. The Hamiltonian of such system can be divided into a linear and nonlinear part as ($H_{\mathrm{full}} = H_{\mathrm{lin}} + H_{\mathrm{nl}}$),

$$H_{\mathrm{lin}} = \hbar\omega_c a_c^{\dagger} a_c + \hbar\omega_q a_q^{\dagger} a_q, \tag{4.2a}$$

$$H_{\mathrm{nl}} = -E_J[\cos\phi_J + \phi_J^2/2], \tag{4.2b}$$

$$\phi_J = \phi_q(a_q + a_q^{\dagger}) + \phi_c(a_c + a_c^{\dagger}), \tag{4.2c}$$

where ω_c and ω_q are the cavity and qubit frequencies with a_c ($a_c^{\dagger}$) and a_q ($a_q^{\dagger}$) being their annihilation (creation) operators with the junction flux ϕ_J consisting of ϕ_c and ϕ_q representing the quantum zero-point fluctuations of junction flux in the cavity and qubit and $\hbar$ denoting the reduced Planck's constant. The ultimate goal of the EPR analysis is to calculate the unknown parameters ω_c, ω_q, ϕ_c, and ϕ_q. The cavity and qubit frequencies can be easily calculated by using the eigenmode solver of the well-known Ansys HFSS microwave simulation software, leading to the linear part of the Hamiltonian (H_{lin}).

In order to resolve the non-linear term (H_{nl}), we need to calculate ϕ_c and ϕ_q. These parameters can be determined by finding the fraction of the stored junction energy (E_J) to that of each of the modes using the electric and magnetic eigenfield results from the simulations defined as,

$$p_m = \frac{\langle \Psi_m | \frac{1}{2} E_J \phi_J^2 | \Psi_m \rangle}{\langle \Psi_m | \frac{1}{2} H_{\text{lin}} | \Psi_m \rangle}. \tag{4.3}$$

where $|\Psi_m\rangle$ denotes a coherent state of mode m in the system.

Using the participation ratios extracted from the finite-element simulations, we can easily extract ϕ_c and ϕ_q to determine the full Hamiltonian,

$$\phi_c^2 = p_c \frac{\hbar\omega_c}{2E_J}, \quad \text{and} \quad \phi_q^2 = p_q \frac{\hbar\omega_q}{2E_J}. \tag{4.4}$$

However, knowing the participation ratios does not directly allow us to calculate the coupling rates between distinct elements of the circuit. Therefore, we need to relate these ratios to parameters used to design real-world experiments. To this end, we can calculate the cross-Kerr matrix elements to link the participation ratios to more practical parameters, such as the anharmonicity of the qubit (α_q) or the coupling rates. The cross-Kerr matrix elements can be derived as a function of the participation ratios in the form of,

$$\chi_{qq} = 2\alpha_q = p_q^2 \frac{\hbar\omega_q^2}{4E_J}, \tag{4.5a}$$

$$\chi_{qc} = p_q p_c \frac{\hbar\omega_c\omega_q}{4E_J}, \tag{4.5b}$$

where the coupling rate between the qubit and the cavity with the detuning Δ_{qc} can be written in terms of χ_{qc} as,

$$g = \sqrt{\chi_{qc}\Delta_{qc}\frac{(\Delta_{qc} + \alpha_q)}{\alpha_q}}. \tag{4.6}$$

Finite-element simulations

Now let us consider a simple simulation example with two transmon qubits coupled via a $\lambda/2$ co-planar waveguide (CPW) resonator where the goal is to extract all the coupling parameters as well as the resonant frequencies as the initial step in designing the desired multi-qubit circuit. In this study, we used the recently developed `Qiskit Metal` package [167] to both draw the design and transfer them to Ansys for the EPR simulations using the integrated `pyEPR` package [168]. Figure 4.3(a) shows the geometry of the coupled qubits in HFSS. Next, we can simply simulate the eigenmodes and eigenfields of each component in Ansys and calculate the energy ratios as discussed above. To start with, we need to define the junctions' inductance, qubits' pad geometry dimensions and the length of the CPW resonator which determines its frequency. We fix the gap (width) of all the CPWs to 6 μm (10 μm) to result in an impedance of $\sim$50 Ω on a 300 μm thick silicon substrate with a dielectric constant of 11.9. Note that the coupling between the qubit and the resonator is inversely proportional to the detuning of these components (Δ_{ic}) given as [169],

$$J = \frac{g_1 g_2}{2}(\frac{1}{\Delta_{1c}} + \frac{1}{\Delta_{2c}}), \tag{4.7}$$

with g_i representing the coupling between qubit i and the mediated resonator determined by the gap and length of the arm at the end of the resonator.

The results from the EPR quantization method is shown in Fig. 4.3(b). The first output of the EPR analysis is the resonant frequencies of each component as, $\omega_{\mathrm{q1}}/2\pi = 4.402$ GHz, $\omega_{\mathrm{q2}}/2\pi = 4.839$ GHz, and $\omega_{\mathrm{c}}/2\pi = 7.910$ GHz. Furthermore, the EPR simulation provides us with the full cross-Kerr matrix where the diagonal elements represent the anharmonicity of each component, $\alpha_{\mathrm{q1}}/2\pi = 217$ MHz and $\alpha_{\mathrm{q2}}/2\pi = 139$ MHz determined by the dimensions of the qubit's ground plane capacitor pads. The off-diagonal elements are defined as the cross-Kerr components used to calculate the coupling rate between components. Having $\chi_{\mathrm{q1,c}}/2\pi = 70.4$ kHz, we can easily calculate the coupling rate between qubit 1 and the resonator $g_1/2\pi = 68$ MHz using Eq. 4.6. Following the same procedure for the second qubit, we can see that $g_2/2\pi = 63$ MHz. The last step is to calculate the effective coupling between the qubits utilizing the (Eq. 4.7), which results in $J_{12}/2\pi = 1.22$ MHz. This concludes the simulations and all the required parameters for the two-qubit coupling case.

In addition to the coupling rates, the readout resonator's coupling quality factor and resonant frequency also needs to be calculated to acquire the dispersive shift between the

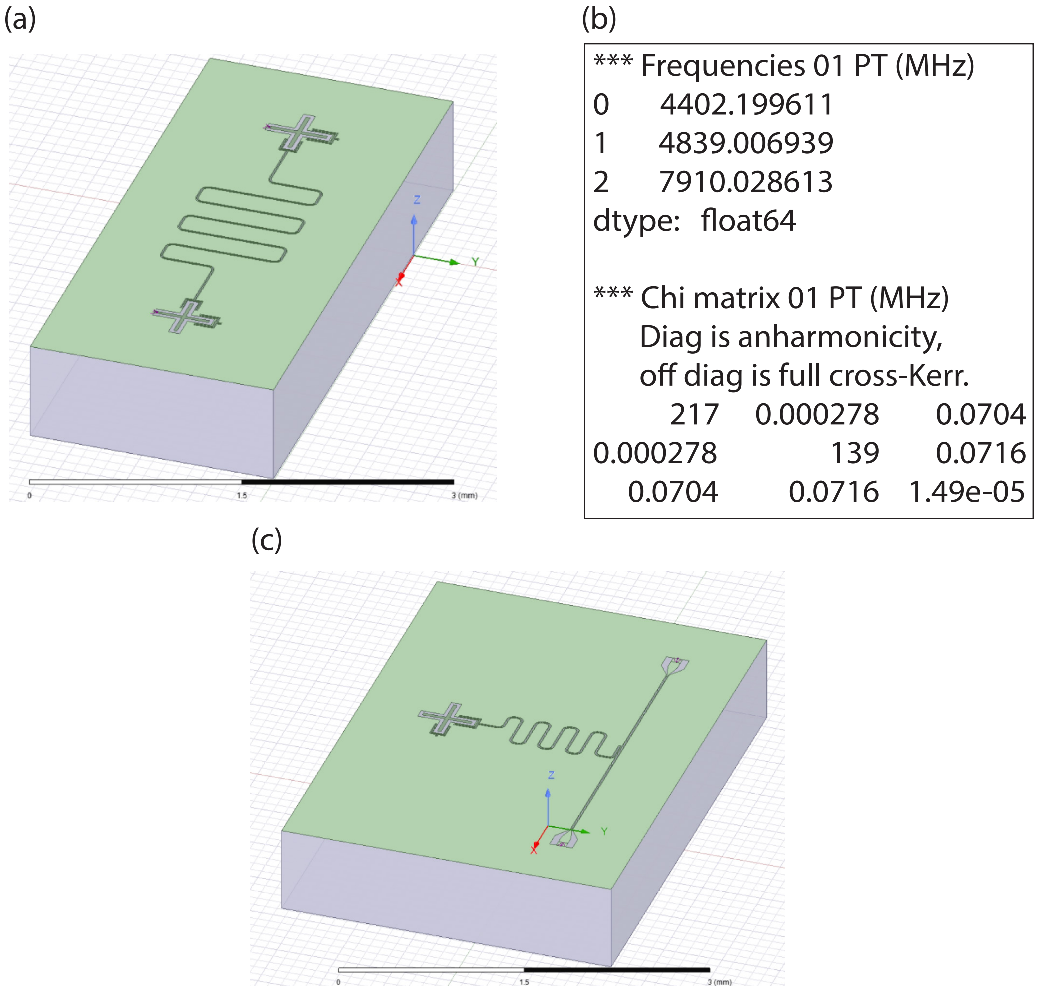

```
*** Frequencies 01 PT (MHz)
0     4402.199611
1     4839.006939
2     7910.028613
dtype:   float64

*** Chi matrix 01 PT (MHz)
     Diag is anharmonicity,
     off diag is full cross-Kerr.
        217    0.000278        0.0704
0.000278              139        0.0716
   0.0704        0.0716   1.49e-05
```

Figure 4.3: The finite-element simulation results incorporating the EPR quantization. (a) The transferred geometry from Qiskit Metal shown in Ansys HFSS. (b) The output of the EPR analysis showing the eigenmode frequencies of each component as well as the full cross-Kerr matrix. (c) Geometry of the coupled resonator to a feedline to extract the linewidth of the cavity.

qubit and cavity and to make sure that our qubit is not Purcell limited, meaning that the coupling is not too strong to reduce the coherence times. The Purcell decay rate of a qubit coupled to a single mode of a cavity with linewidth, κ is given as,

$$\Gamma_{\text{Purcell}} = \frac{g^2}{\Delta_{\text{qc}}^2}\kappa. \tag{4.8}$$

The only parameter left to simulate to get the Purcell decay rate is the cavity linewidth. To this end, we need to design a $\lambda/4$ CPW resonator capacitively coupled to a transmission feedline and define two lumped-element ports at the ends of the transmission line to look at the S-parameters in HFSS simulations. After careful meshing of the geometry and finding the resonance dip in the transmission spectrum, the 3-dB method [170] can be used to acquire the linewidth. Having the rest of the required parameters from the EPR simulation, we will be able to calculate the Purcell decay rate. It is noteworthy that to achieve the optimal readout signal-to-noise ratio, the cavity's linewidth should ideally be approximately equal to its dispersive shift, $\kappa \simeq 2\chi$.

In a similar manner, we can calculate the Purcell decay rate of the drive lines by looking at the reflection spectrum of the drive line port and extract the coupling rate using the 3-dB method and use Equation 4.8. Typically, a gap of 30 to 40 μm between the end of the drive line and the qubit's capacitor pad results in Purcell-limited relaxation times of about 200 μs with reasonable single-qubit gate times of $\sim$50 ns.

As for the fast flux lines, we need to calculate the mutual inductance between the SQUID loop and the flux line. We utilize AWR Microwave Office to simulate the Z parameters and then converting that to the mutual inductance as, $M = d\,\text{imag}(Z_{12})/d\,\omega$ with Z_{12} derived from the S parameters discussed in Section 4.4 of [171] (Fig. 4.4(a)). The imaginary part of Z_{12} is shown in Fig. 4.4(b) as a function of the frequency after setting the inductance of the junctions to 16 nH. Using its slope we can solve for the mutual inductance resulting in, $M \approx 3.7$ pH. To get the required current for a flux quanta we have, $i = \Phi_0/M$, where $\Phi_0 = h/2e$ is the magnetic flux quanta with h and e being the Plank's constant and the electron charge, respectively. From this we get $i \approx 560\ \mu$A. Take heed that having larger mutual inductance decreases the amount of current needed for a flux quanta with the caveat of the qubit being more susceptible to flux noise due to the stronger coupling. Hence, in the field of superconducting circuits the mutual inductance is typically set to a few picoHenries.

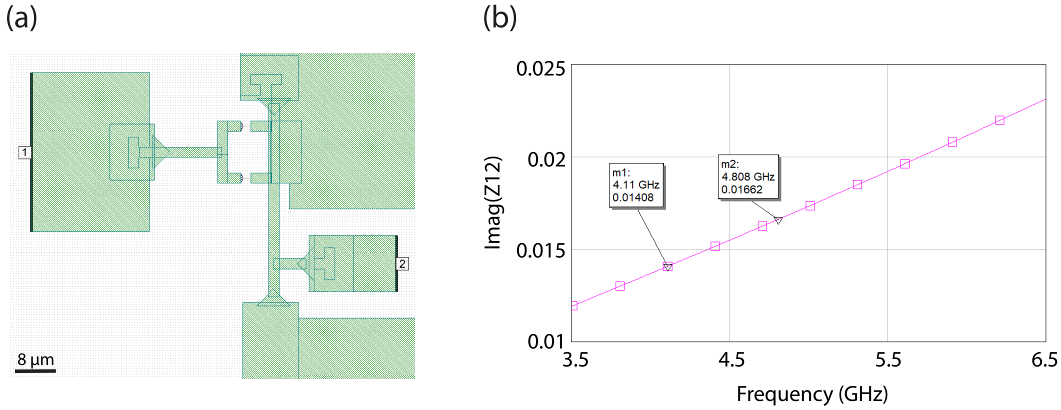

Figure 4.4: Simulating the mutual inductance of the fast flux line. (a) The geometry shown in AWR microwave office. (b) Simulation result demonstrating a linear slope for the imaginary part of Z_{12} as a function of frequency used to calculate the mutual inductance.

Figure 4.5 depicts the final layout used for the fabrication of the desired three-qubit device, named "Muninn". The simulated parameters for the device used in this project are given in Table 4.1. To elaborate, the readout resonator frequencies are separated by ~150 MHz, compatible with the bandwidth of the parametric amplifier used in the experimental setup and to avoid any unintentional coupling between them. The qubit frequencies were chosen in such a way that the system qubit can be brought close to the ancilla qubit's resonance frequency, hence we can apply two-qubit entangling gates required for this project with reasonable gate times as described in Section 4.5.

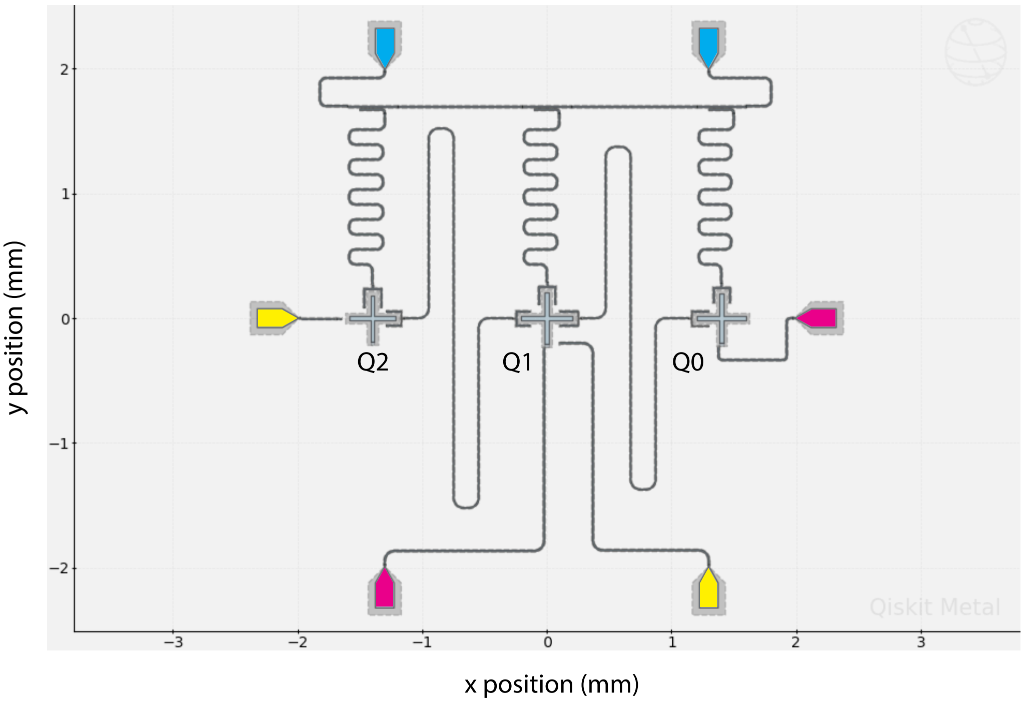

Figure 4.5: Color coded layout of Muninn in Qiskit Metal to demonstrate the drive lines in yellow, fast flux lines in magenta, and feedline ports in blue.

	$\omega_{\mathrm{q}}/2\pi$ (GHz)	$\lvert\alpha\rvert/2\pi$ (MHz)	$\chi_{\mathrm{qc}}/2\pi$ (kHz)	$g_1/2\pi$ (MHz)	$g_2/2\pi$ (MHz)	$\omega_{\mathrm{c}}/2\pi$ (GHz)	$\kappa/2\pi$ (kHz)
Q0	5.6	180	200	-	89	7.47	200
Q1	5.1	175	210	60	87	7.3	200
Q2	4.6	195	210	66	-	7.15	200

Table 4.1: Simulated parameters used to fabricate Muninn.

4.3 Experimental methods

This section covers the methods required to fabricate a qubit processor, how to set up the experiment inside a cryostat, and the techniques used to amplify the input signal for quantum measurements.

4.3.1 Superconducting qubit fabrication

The immediate next step in setting up our experiment after designing a simulated layout, is to fabricate the superconducting circuit using conventional nano-fabrication techniques. To fabricate a multi-qubit processor, we first need to make the resonators using the subtractive method explained in Section 2.4.2 and then patch the Josephson junctions (JJ) in a separate layer after removing the native surface oxide from the base metal layer using ion milling. Junctions are fabricated based on the Niemeyer-Dolan-bridge method [172, 173], where we start with spin coating a bi-layer stack of MMA-EL13 electron-beam resist as the top layer and ZEP-520A as the top layer on a 2-inch intrinsic silicon wafer with resistivity $> 8\ \mathrm{k}\Omega \cdot \mathrm{cm}$ at a spinning rate of 3000 rpm for 60 s for both layers after removing the organics and the native surface oxide from the substrate. The substrate is then soft baked after each spin to remove the moisture from the spun resists at 180 and 200 °C. This results in resist thicknesses of 450 and 280 nm, respectively.

Next, the resist needs to be exposed with electron beams to make the desired mask with Dolan-bridge structures. Figure 4.6(a) shows the layout of a typical three-dimensional transmon where each color represents a separate layer written with a different exposure time. At the heart of our design, we have the JJs with features as small as 200 nm, making them the most sensitive structures in the whole process. Due to their subtleties and to prevent the bridge from being over-exposed, these features are typically exposed using a low beam current (50 pA) with an area dose of $\sim$300 μC/cm^2. The capacitor pads (blue layer in Fig. 4.6(a)), on the other hand, are exposed with a relatively higher current, 4 nA with the same amount of area dose as the previous layer to expedite the exposure, which determine the anharmonicity of the qubit.

The mask is then developed in two separate solvents. First, we develop the top layer (ZEP-520A) using ZED-N50 developer at 0 °C for one minute. Immediately after that, we resolve the required undercut to form the Dolan-bridge by immersing the wafer in a solution of MIBK/IPA with ratios of 3:1 for 150 s to make sure we form enough undercut to realize the bridge. Finally, we clean the wafer in pure IPA for 15 s before blow drying the sample with nitrogen.

After development, we need to clean the sample for 30 s under oxygen plasma at 100 W of power to remove the residual resists on the substrate. Then the sample is ready for metallization in the electron-beam evaporator. To form the junction, we utilize a double-angle evaporation technique to deposit aluminum with thicknesses of 30 and 60 nm mediated by an oxidation step in between to form the dielectric layer. The overlap size can easily be calculated using simple two-dimensional geometry analysis given as (Fig. 4.6(b)),

$$s' = 2\tan(\theta)(H - \frac{s}{2}\tan(90-\theta)), \tag{4.9}$$

where H is the thickness of the bottom-layer resist with s representing the designed bridge width of the junction and θ denoting the evaporation angle in degrees.

Now we simply need to remove the extra aluminum from the wafer by immersing the sample in the remover-PG solution heated at 70 °C for two to three hours. Figure 4.6(c) shows the scanning electron microscopy image of a fabricated transmon qubit with JJ dimensions of 120 × 200 nm. Next, we probe the resistance of the junction at room temperature, which is inversely proportional to the critical current across the junction below the aluminum's transition temperature, given by the Ambegaokar-Baratoff relation [174],

$$I_c = \pi\frac{\Delta}{2eR}, \tag{4.10}$$

with Δ being the superconducting gap of the aluminum and R denoting the measured resistance of the junction at room temperature. The first transition frequency of the qubit can be calculated as [8], $\hbar\omega_{01} = \sqrt{8E_\mathrm{J}E_\mathrm{C}} - E_\mathrm{C}$, where E_C denoted the capacitive energy (anharmonicity) of the device determined by the dimensions of the capacitor pads and E_J is the energy stored in the junction as, $E_\mathrm{J} = \hbar I_\mathrm{C}/2e$. Typically, for a qubit with a reasonable frequency between 4 to 5 GHz with a designed $E_C = 250$ MHz, we need to achieve a critical current ∼10 nA. This concludes the fabrication techniques required to make multi-qubit processors and now we can look at the cryogentic microwave setup needed to measure such devices.

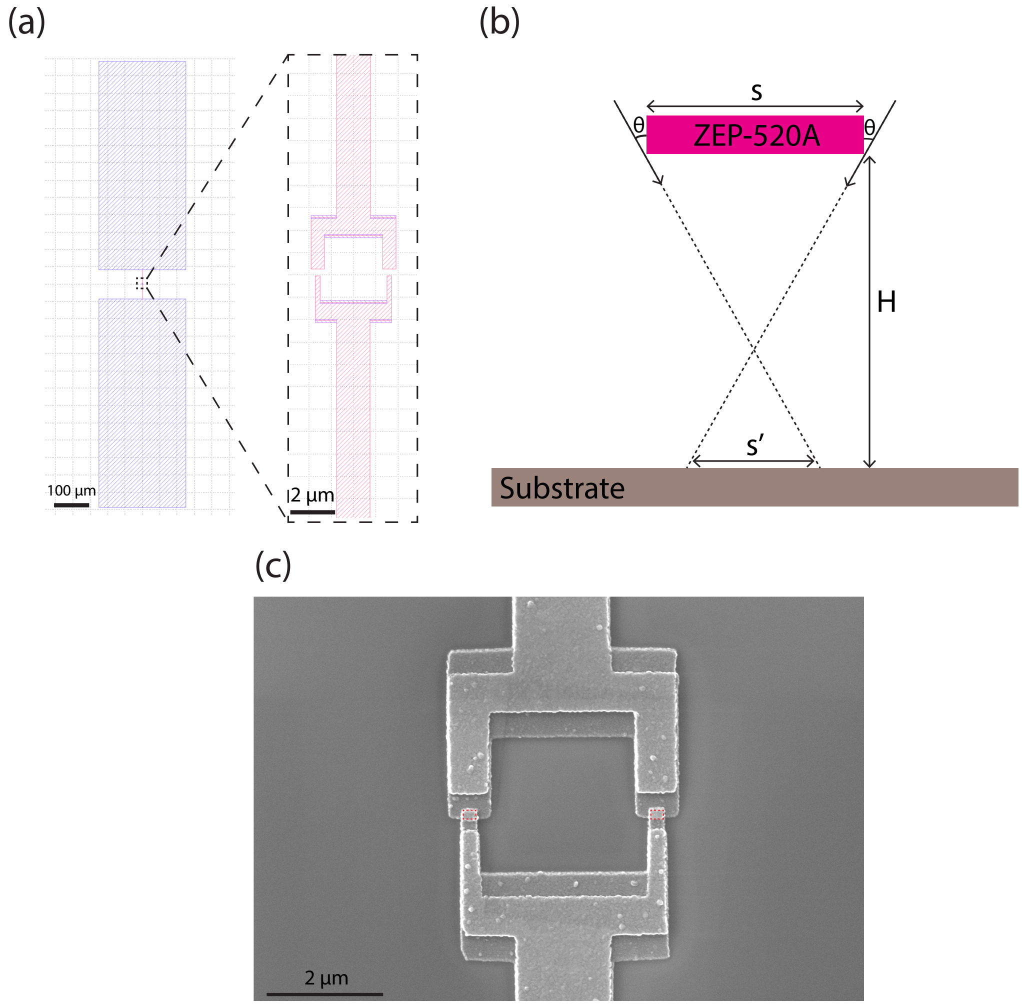

Figure 4.6: Fabrication of superconducting qubits. (a) The prepared layout showing different layers with blue indicating the capacitor pads and the red layer representing the junction. (b) The geometry analysis used to calculate the junction overlap. (c) The scanning electron microscopy image of a fabricated qubit with junctions marked with red dashed lines.

4.3.2 Cryogenic setup and preliminary characterizations

Harnessing quantum effects requires the suppression of the thermal fluctuations as much as possible. Therefore, the circuits need to be cooled down in dilution refrigerators with base temperatures of < 15 mK. In addition, the devices need to be probed with very low power in order to prevent heating and dephasing mechanisms. As the first order treatment to setup the experiment, the device needs to be isolated from the environment around them. The device is packaged in a copper box and surrounded by an additional copper and aluminum can as well as a cryoperm shielding to protect the device from the infrared radiations and external magnetic fields. The device is further thermalized to the mixing chamber stage via a copper plate as well as all the coaxial lines at each stage via microwave attenuators.

Moving onto the microwave setup in the fridge, we utilize microwave attenuators to reduce the input power on the device as well as to mitigate the microwave noise. Figure 4.7 demonstrates the complete wiring of the cryogenic setup of the experiment. For the fast flux lines (colored in magenta), we used a total of 40 dB attenuation as well as 300 MHz low-pass filters (MiniCircuits 300 VLFX) to suppress the high-frequency noise with a bias-tee at the top of the fridge to apply a DC current to tune the frequency of the qubits. Due to the stronger coupling of the drive lines, we added 60 and 70 dB of attenuation for drive lines 1 and 2, respectively. This arrangement of the attenuators allows us to achieve Rabi oscillations as fast as 20 MHz. In addition, we installed 7.2 GHz low-pass filters (MiniCircuits 7200+ VLFX) to mitigate the high-frequency noise. Finally, for the readout input line we added 70 dB of attenuation with a K&L low-pass filter at 8 GHz to ensure the low noise level. Note that, an eccosorb infrared filter was installed for every single microwave line inside the copper shielding with > 10 GHz cutoff frequencies to absorb the infrared radiation.

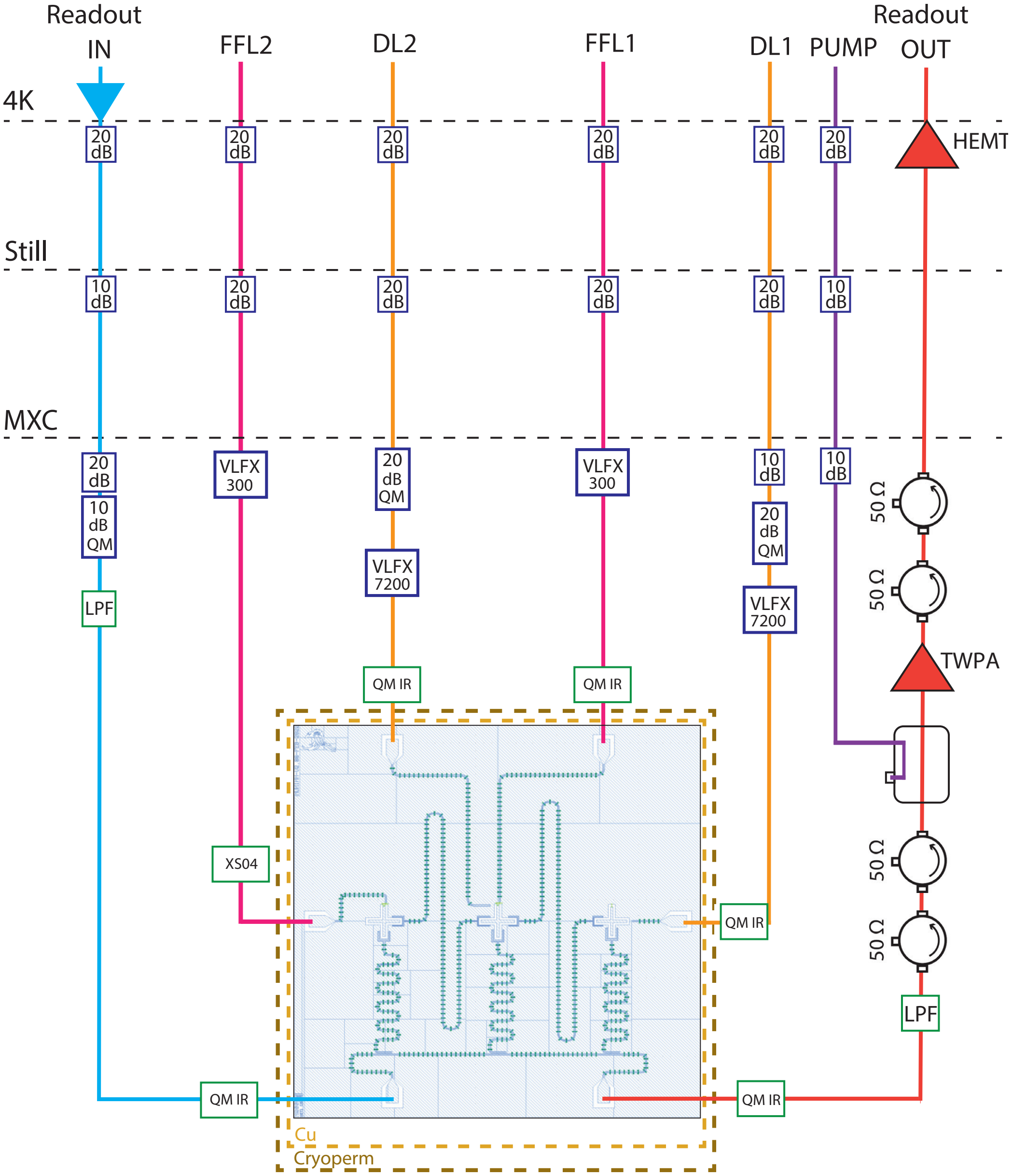

Figure 4.7: Cryogenic microwave setup of Muninn showing the microwave components at each stage.

To amplify the output signal, we make use of a high-electron-mobility transistor (HEMT) low-noise amplifier at the 4K stage and a travelling-wave parametric amplifier (TWPA) at milliKelvin temperatures with gains of about 40 dB and 20 dB, respectively. The noise temperature of the amplifier is proportional to its physical temperature, which makes it necessary to have the amplifiers at cold stages to achieve single-shot quantum state readout [175]. The TWPA used in this experiment is based on the SNAIL architecture resulting in reversed Kerr phase matching [176] with bandwidths as high as 4 GHz and noise temperatures of about 300 mK. The other advantage of this type of TWPA is that it can be pumped at frequencies ∼2 GHz away from the range of interest through a directional coupler, which results in minimal interference between the pump and readout signal in the experiment. On the other hand, due to the strong pump power, we install two cryogenic circulators both before and after the TWPA to further suppress any leakage that might hurt the readout readout signal.

To characterize the gain of the TWPA, we look at the transmission through the feedline of the device using a vector-network analyzer and compare the level with the TWPA pump being on and off. Figure 4.8 demonstrates the typical gain of the TWPA pumped at 9.8 GHz and operated at half of the flux-quanta showing an average gain of 20 dB over the desired range covering the resonant frequency our readout resonators.

We utilize conventional spectroscopy methods to characterize the frequency of the devices (reported at zero flux) and their corresponding dispersive shifts and the linewidths of the cavities [38]. We achieved an accuracy of 90% between the simulation and the measurement values, as shown in Table 4.2, proving the efficacy of the simulation methods and the precision of the fabrication techniques. Section 1.2.4 includes more details on the room temperature setup.

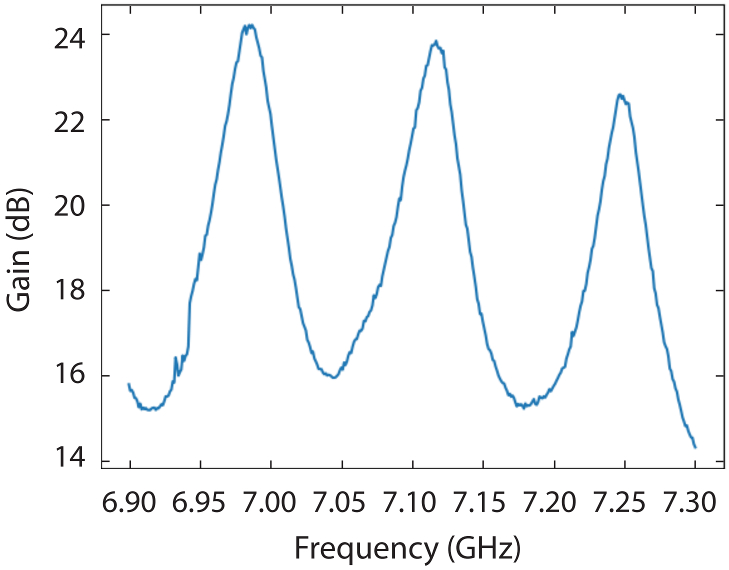

Figure 4.8: Optimal gain profile of the TWPA after carefully optimizing the pump frequency, power, and the flux bias.

	$\omega_q/2\pi$ (GHz)	$\lvert\alpha\rvert/2\pi$ (MHz)	$\chi_{qc}/2\pi$ (kHz)	$\omega_c/2\pi$ (GHz)	$\kappa/2\pi$ (kHz)
Q0	5.4	150	260	7.21	170
Q1	4.6	180	250	7.09	206
Q2	4.2	212	230	6.94	270

Table 4.2: Muninn measured parameters showing great accuracy compared to the simulations.

4.4 State tomography

To reconstruct the density matrix of a system one needs to master the tomography techniques. In this section, I will introduce the basics of the state tomography by starting with single-qubit tomography as the simplest case followed by an extension of the methods to two-qubit systems.

4.4.1 Single-qubit state tomography

For a single qubit, the density matrix has 4 components, meaning that a minimum of three measurements are needed to reconstruct the full matrix after taking into account the Hermiticity and trace-preserving nature of a physical density matrix. Since in our measurement scheme, we are only capable of measuring along the z axis, two additional rotations (in and out of phase $\pi/2$ pulses) must be applied immediately before the readout pulse to project the other two axes, populations to Z in order to measure the $\langle x\rangle$ and $\langle y\rangle$ expectation values as shown in Figure 4.9(a). For an arbitrary state in the $\{|0\rangle, |1\rangle\}$ basis, ($|\psi\rangle = a|0\rangle + b|1\rangle$) the normalized expectation value is defined as,

$$\begin{aligned}\langle z\rangle = \frac{\langle\psi|\sigma_z|\psi\rangle}{\langle\psi|\psi\rangle} &= \frac{1}{|a|^2+|b|^2}\begin{pmatrix} a^* & b^* \end{pmatrix}\begin{pmatrix} 1 & 0 \\ 0 & -1 \end{pmatrix}\begin{pmatrix} a \\ b \end{pmatrix} \\ &= \frac{|a|^2-|b|^2}{|a|^2+|b|^2}. \end{aligned} \tag{4.11}$$

It is easy to show that $|a|^2 = \mathrm{pr}^{(z)}(0)/(\mathrm{pr}^{(z)}(0) + \mathrm{pr}^{(z)}(1))$ and $|b|^2 = \mathrm{pr}^{(z)}(1)/(\mathrm{pr}^{(z)}(0) + \mathrm{pr}^{(z)}(1))$, representing the probabilities of measuring the system in the ground and excited state, where superscript $^{(z)}$ denotes the measurement axis. The expectation value can now be rewritten as,

$$\langle z \rangle = \frac{\mathrm{pr}^{(z)}(0) - \mathrm{pr}^{(z)}(1)}{\mathrm{pr}^{(z)}(0) + \mathrm{pr}^{(z)}(1)}. \tag{4.12}$$

The same approach can be used to calculate the rest of the expectation values,

$$\langle x \rangle = \frac{\mathrm{pr}^{(x)}(0) - \mathrm{pr}^{(x)}(1)}{\mathrm{pr}^{(x)}(0) + \mathrm{pr}^{(x)}(1)}, \tag{4.13}$$

$$\langle y \rangle = \frac{\mathrm{pr}^{(y)}(0) - \mathrm{pr}^{(y)}(1)}{\mathrm{pr}^{(y)}(0) + \mathrm{pr}^{(y)}(1)}. \tag{4.14}$$

Now that we have all the required measurement results, the density matrix of our single-qubit system is simply calculated as,

$$\rho = \frac{1}{2}(\mathcal{I} + \langle x \rangle \sigma_x + \langle y \rangle \sigma_y + \langle z \rangle \sigma_z), \tag{4.15}$$

where $\sigma_x, \sigma_y,$ and σ_z are the Pauli matrices with $\mathcal{I}$ denoting the 2×2 identity matrix.

Experimentally, one calibrates the tomography pulses by looking at all of the three tomography components after applying a time-varying Rabi drive with a constant amplitude on the qubit (Fig. 4.9(b)). After carefully adjusting the resonance frequency of the qubit using a typical Ramsey measurement [177], the time and amplitude of the tomography pulses as well as the orthogonality of the IQ mixers [178], the result should indicate oscillations on two of the components and a flat line for the third component as shown in Figure 4.10, indicating that the rotation occurs in either XZ or YZ plane on the Bloch sphere contingent on the rotational axis of the Rabi drive.

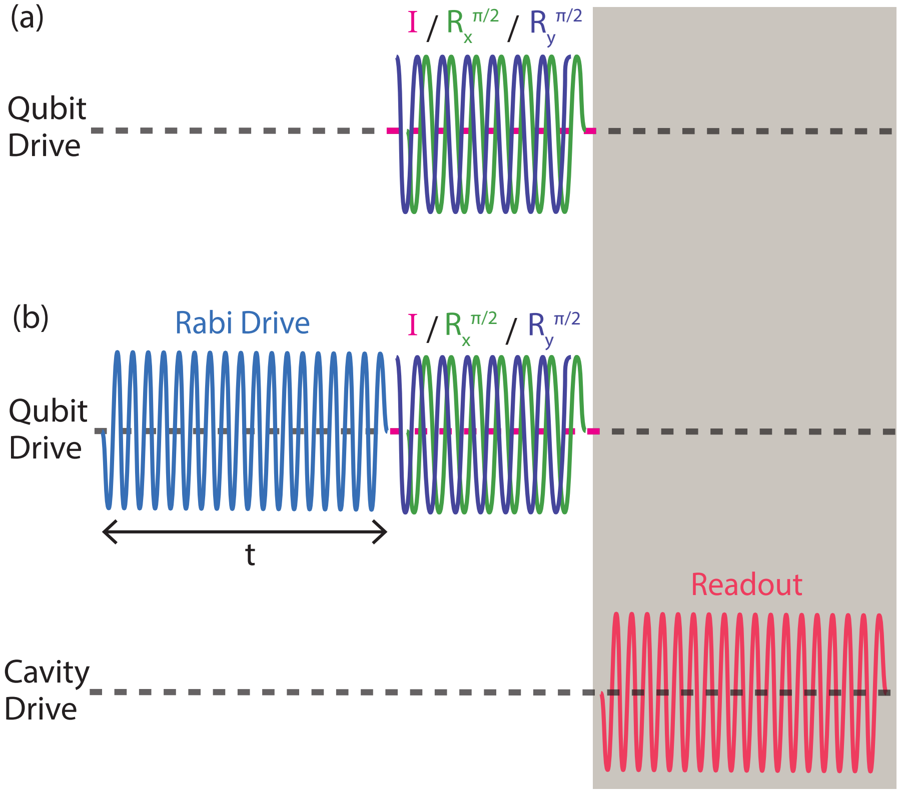

Figure 4.9: Single-qubit tomography pulses for (a) full state density matrix construction and (b) calibration utilizing a Rabi drive.

4.4.2 Two-qubit state tomography

In the more complicated case of two qubits, the density matrix (ρ) consists of 16 components. Similar to the single-qubit case, the Hermiticity and trace-preserving characteristics of ρ

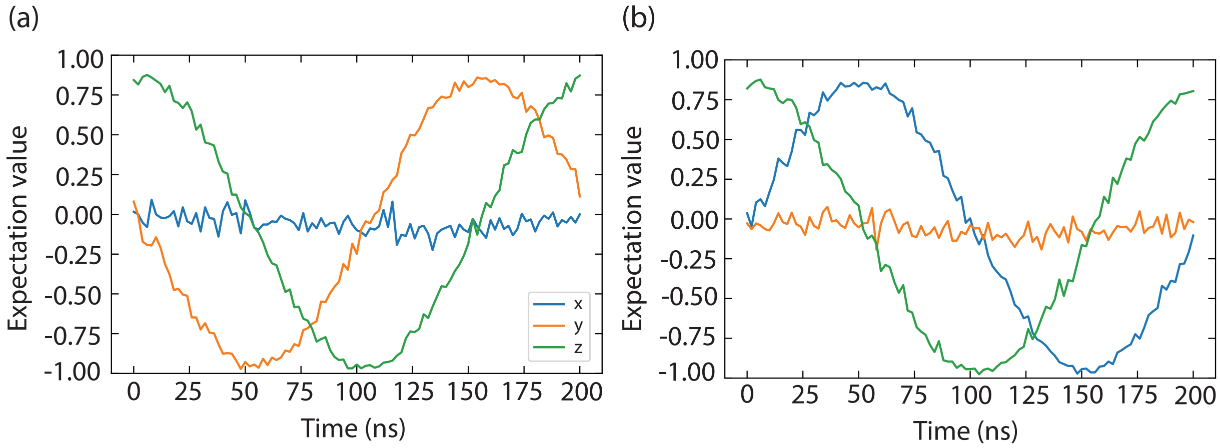

Figure 4.10: Calibrated tomography pulses for a Rabi drive along (a) X and (b) Y axis.

basically reduce the number of the required measurements to extract all the components of ρ. Conventionally, 30 distinct measurements are needed to find the components of the density matrix [179, 180] for the joint readout scheme, where the qubits share a readout resonator. However, since we have separate readout resonators for each qubit, we can simply elicit all the components by performing only 9 measurements (Table 4.3) after implementing the simultaneous readout scheme described in Section 1.2.4 for all the nine tomography pulses (Fig. 4.11).

As an example, measuring both qubits along Z yields in $\langle IZ\rangle, \langle ZI\rangle,$ and $\langle \mathrm{ZZ}\rangle$ (excluding the trivial $\langle II\rangle$). Using the analogy in Equation 4.12 for an arbitrary state in $\{00, 01, 10, 11\}$ basis ($|\psi\rangle = a|00\rangle + b|01\rangle + c|10\rangle + d|11\rangle$), the normalized expectation value $\langle IZ\rangle$, is given as,

$$\begin{aligned}\langle IZ\rangle = \frac{\langle\psi|\mathcal{I}\otimes\sigma_z|\psi\rangle}{\langle\psi|\psi\rangle} &= \frac{|a|^2 - |b|^2 + |c|^2 - |d|^2}{|a|^2 + |b|^2 + |c|^2 + |d|^2} \\ &= \frac{\mathrm{pr}^{(z)}(00) - \mathrm{pr}^{(z)}(01) + \mathrm{pr}^{(z)}(10) - \mathrm{pr}^{(z)}(11)}{\mathrm{pr}^{(z)}(00) + \mathrm{pr}^{(z)}(01) + \mathrm{pr}^{(z)}(10) + \mathrm{pr}^{(z)}(11)},\end{aligned} \tag{4.16}$$

Rotation	Measurement operator	Expectation values
$R_Y^{\pi/2} \otimes R_Y^{\pi/2}$	XX	$\langle IX\rangle, \langle XI\rangle, \langle XX\rangle$
$R_Y^{\pi/2} \otimes R_X^{-\pi/2}$	XY	$\langle IY\rangle, \langle XI\rangle, \langle XY\rangle$
$R_Y^{\pi/2} \otimes \mathcal{I}$	XZ	$\langle IZ\rangle, \langle XI\rangle, \langle XZ\rangle$
$R_X^{-\pi/2} \otimes R_Y^{\pi/2}$	YX	$\langle IX\rangle, \langle YI\rangle, \langle YX\rangle$
$R_X^{-\pi/2} \otimes R_X^{-\pi/2}$	YY	$\langle IY\rangle, \langle YI\rangle, \langle YY\rangle$
$R_X^{-\pi/2} \otimes \mathcal{I}$	YZ	$\langle IZ\rangle, \langle YI\rangle, \langle YZ\rangle$
$\mathcal{I} \otimes R_Y^{\pi/2}$	ZX	$\langle IX\rangle, \langle ZI\rangle, \langle ZX\rangle$
$\mathcal{I} \otimes R_X^{-\pi/2}$	ZY	$\langle IY\rangle, \langle ZI\rangle, \langle ZY\rangle$
$\mathcal{I} \otimes \mathcal{I}$	ZZ	$\langle IZ\rangle, \langle ZI\rangle, \langle ZZ\rangle$

Table 4.3: Two-qubit tomography measurement operators and their corresponding 16 expectation values.

where $\mathrm{pr}^{(z)}(00)$ ($\mathrm{pr}^{(z)}(11)$) is the joint probability of finding both qubits in the ground (excited) state measured along the Z axis. Additionally, $\mathrm{pr}^{(z)}(01)$ ($\mathrm{pr}^{(z)}(10)$) is the probability of finding the first qubit in the ground (excited) and the second qubit in the excited (ground) state. Similarly, we can write the other two expectation values as,

$$\begin{aligned}\langle ZI\rangle = \frac{\langle\psi|\sigma_z \otimes \mathcal{I}|\psi\rangle}{\langle\psi|\psi\rangle} &= \frac{|a|^2 + |b|^2 - |c|^2 - |d|^2}{|a|^2 + |b|^2 + |c|^2 + |d|^2} \\ &= \frac{\mathrm{pr}^{(z)}(00) + \mathrm{pr}^{(z)}(01) - \mathrm{pr}^{(z)}(10) - \mathrm{pr}^{(z)}(11)}{\mathrm{pr}^{(z)}(00) + \mathrm{pr}^{(z)}(01) + \mathrm{pr}^{(z)}(10) + \mathrm{pr}^{(z)}(11)}, \qquad (4.17) \\ \langle ZZ\rangle = \frac{\langle\psi|\sigma_z \otimes \sigma_z|\psi\rangle}{\langle\psi|\psi\rangle} &= \frac{|a|^2 - |b|^2 - |c|^2 + |d|^2}{|a|^2 + |b|^2 + |c|^2 + |d|^2} \\ &= \frac{\mathrm{pr}^{(z)}(00) - \mathrm{pr}^{(z)}(01) - \mathrm{pr}^{(z)}(10) + \mathrm{pr}^{(z)}(11)}{\mathrm{pr}^{(\mathrm{z})}(00) + \mathrm{pr}^{(\mathrm{z})}(01) + \mathrm{pr}^{(\mathrm{z})}(10) + \mathrm{pr}^{(\mathrm{z})}(11)}. \qquad (4.18)\end{aligned}$$

The remaining set of expectation values can be calculated in a similar manner after applying the tomogrpahy pre-rotation pulses. Having all the 16 expectation values leaves us in a

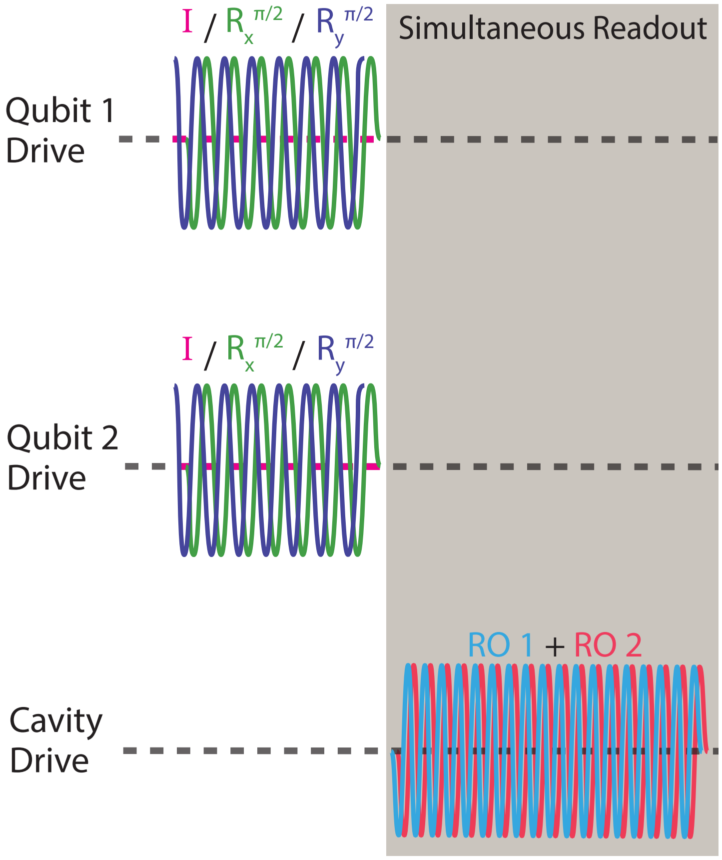

Figure 4.11: Two-qubit tomography sequence utilized to reconstruct the full density matrix.

position to utilize a least-square maximum likelihood estimation [181] to construct the density matrix. To this end, we define a lower-triangular matrix as,

$$T = \begin{pmatrix} t_1 & 0 & 0 & 0 \\ t_5 + it_6 & t_2 & 0 & 0 \\ t_7 + it_8 & t_9 + it_{10} & t_3 & 0 \\ t_{11} + it_{12} & t_{13} + it_{14} & t_{15} + it_{16} & t_4 \end{pmatrix}, \tag{4.19}$$

where the density matrix can be written as $\rho = \frac{T^\dagger T}{\mathrm{Tr}(T^\dagger T)}$, where $\mathrm{Tr}(\cdot)$ is the trace over the entire two-qubit system state space and † denotes the conjugate transpose of a matrix. The invertibility of T assures the Hermiticity of ρ as well as its trace-normalization.

To efficiently calculate the density matrix, we incorporate the `least_squares` function under the `scipy.optimize` package [182] with the minimization vector in the form of,

$$\mathcal{L}_k = \Big(\mathrm{Tr}(\hat{\mathcal{M}}_k\ \rho) - p_k\Big)^2 . \tag{4.20}$$

Here, $\hat{\mathcal{M}}_k$ represents the measurement operators with p_k being the outcome of each measurement and k runs over all the 16 measurement values. To minimize $\mathcal{L}$, we vary $\vec{t}$ (a real vector consisted of the T matrix components) until we have the least value for the minimization function and we take that as the optimum value for our density matrix. To clarify the relation between the elements in the T matrix (Eq. 4.19) and the measurement operators, the first term of Eq. 4.20 is given in Table. 4.4 for each measurement operator. Given the complexity of the expectation values, this problem is most efficiently solved by an optimization algorithm mentioned above utilizing all the 16 expectation values.

Measurement operator $\hat{\mathcal{M}}$	$\mathrm{Tr}(\hat{\mathcal{M}}\ T^\dagger T)/2$
XX	$t_3t_9 + t_4t_{11} + t_{13}t_{15} + t_{14}t_{16}$
XY	$t_4t_{12} - t_3t_{10} + t_{13}t_{16} - t_{14}t_{15}$
XZ	$t_3t_7 - t_4t_{13} + t_{12}t_{16} + t_{11}t_{15}$
YX	$t_4t_{12} + t_3t_{10} - t_{13}t_{16} + t_{14}t_{15}$
YY	$t_3t_9 - t_4t_{11} + t_{13}t_{15} + t_{14}t_{16}$
YZ	$t_3t_8 - t_4t_{14} - t_{11}t_{16} + t_{12}t_{15}$
ZX	$t_7t_9 + t_8t_{10} + t_2t_5 - t_4t_{15} + t_{14}t_{12} + t_{11}t_{13}$
ZY	$t_8t_9 + t_2t_6 - t_7t_{10} - t_4t_{16} - t_{11}t_{14} + t_{12}t_{13}$
ZZ	$t_1^2 - t_2^2 - t_3^2 + t_4^2 + t_5^2 + t_6^2 + t_7^2 + t_8^2$ $-t_9^2 - t_{10}^2 + t_{11}^2 + t_{12}^2 - t_{13}^2 - t_{14}^2 - t_{15}^2 - t_{16}^2$

Table 4.4: Expectation terms used to reconstruct the full density matrix with an optimization problem.

In summary, here are the steps required to reconstruct the full two-qubit density matrix:

1. Perform nine simultaneous measurements and store all the 16 expectation values as listed in Table 4.3. Note that some expectation values are measured more than once. In that case, the average of all the same expectation values should be used for the following steps.

2. Define an arbitrary lower-triangular matrix (Eq. 4.19), write the density matrix in terms of that, and set up the minimization function (Eq. 4.20) using the measurement results, p_k, from the previous step. This is to ensure that the reconstructed density matrix is trace-preserving and positive.

3. Employ an optimization algorithm to optimize the minimization function and determine the desired T matrix elements. The imaginary and real parts of the $\mathcal{L}$ need to be

optimized simultaneously for all the measurements. Hence, summing up the loss functions over all the measurements is the most efficient approach, $\mathcal{L} = \sum_k \mathcal{L}_k$.

4. Finally, reconstruct the two-qubit density matrix using the calculated T matrix as, $\rho = T^\dagger T/\mathrm{Tr}(T^\dagger T)$.

The simplest way to check the feasibility of this method is to look at the tomography results after preparing the qubits in product states. Figure 4.12 demostrates the reconstructed density matrix for four distinct separable initial states with an average fidelity of 84%. In the next section, we will further check the efficacy of this method by initializing a Bell state for our system and use the above-mentioned technique to reconstruct the mixed state.

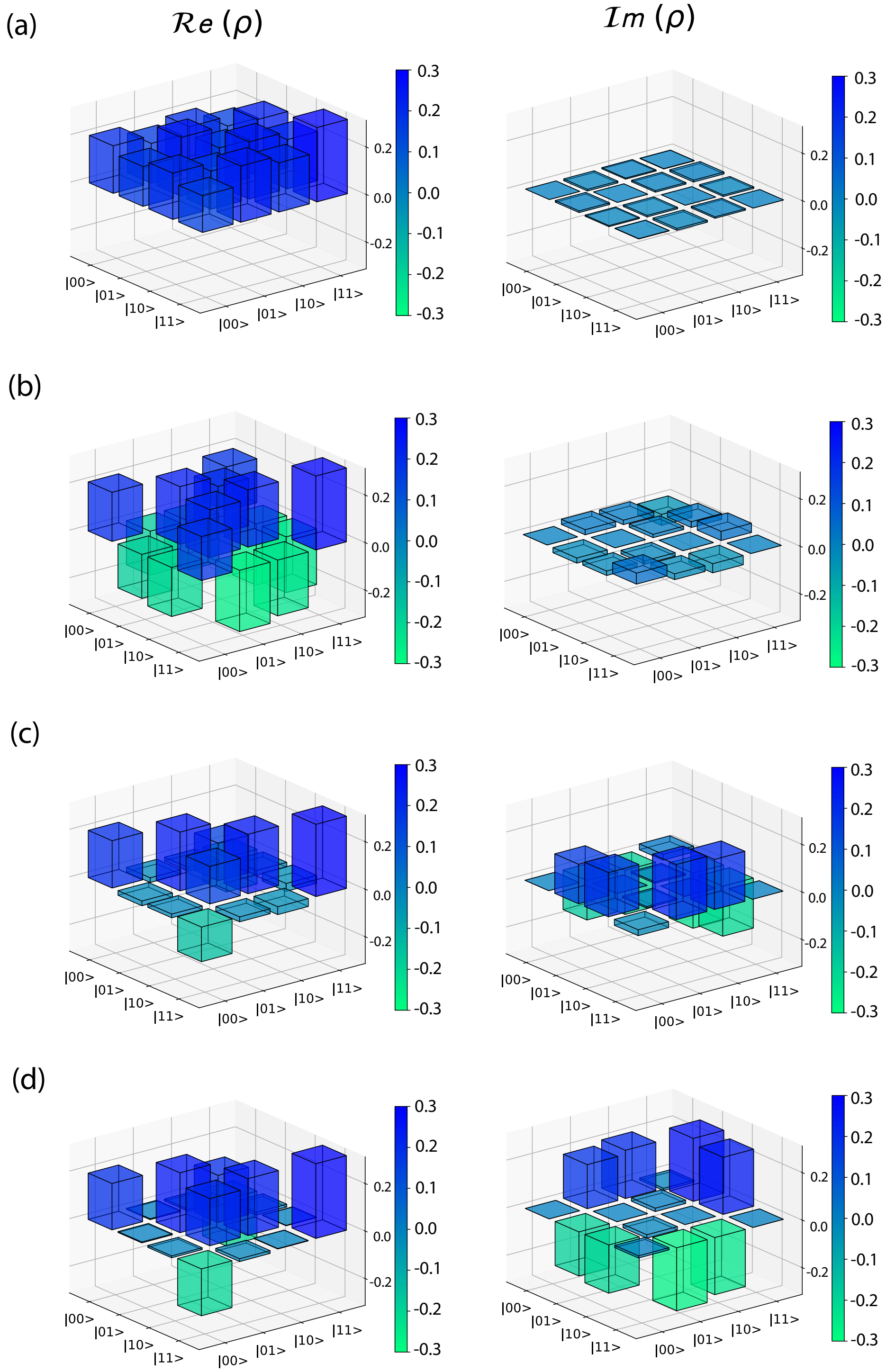

Figure 4.12: Real and imaginary parts of the reconstructed two-qubit density matrices for initially prepared product states (a) $|x+\rangle \otimes |x+\rangle$, (b) $|x-\rangle \otimes |x-\rangle$, (c) $|y+\rangle \otimes |y+\rangle$, and (d) $|y-\rangle \otimes |y-\rangle$.

4.5 Cross-resonance gate

Among various two-qubit entangling gates, the cross-resonance gate is of the most common entangling schemes utilized due to its high fidelity and ease of implementation. The cross-resonance gate was first demonstrated experimentally in 2011 [183]. This section will treat the theory background behind this entangling gate, and discuss the details on tuning the gate parameters in experiment.

4.5.1 Theory background

To start with, the Hamiltonian of a two-qubit system with XX coupling in the rotating frame with qubit resonance frequencies, $\omega_{1,2}$ is in the form of,

$$H/\hbar = \frac{1}{2}\omega_1 ZI + \frac{1}{2}\omega_2 IZ + JXX, \tag{4.21}$$

where J is the residual qubit-qubit coupling rate. For qubits coupled via resonators, is given as,

$$J = \frac{g_1 g_2}{2}(\frac{1}{\Delta_1} + \frac{1}{\Delta_2}), \tag{4.22}$$

with Δ_i denoting the detuning of qubit i from the coupling resonator frequency ω_r and g_i is the coupling rate between qubit i and the resonator.

The system Hamiltonian (Eq. 4.21) can be diagonalized by having two new sets of qubit frequencies, $\tilde{\omega}_1 = \omega_1 + J/\Delta_{12}$ and $\tilde{\omega}_2 = \omega_2 - J/\Delta_{12}$, where $\Delta_{12} = \omega_1 - \omega_2$ is the qubit-qubit detuning. Hence, in the cross-resonance (CR) scheme, control qubit is driven at the frequency of the target qubit $\omega_d \simeq \tilde{\omega}_t$ (Fig. 4.13(a)). This drive introduces a rotation on the target qubit with a frequency depending on the state of the control qubit, which is the main element behind the controlled-NOT (CNOT) gate in qubit processors to entangle and manipulate the interactions between two neighboring qubits.

We can write the Hamiltonian for such a drive with an amplitude of $A(t)$ on the control qubit as,

$$H_{\mathrm{D}}/\hbar = A(t)\cos(\tilde{\omega}_2 t)(\eta XI - \mu ZX + m_{12} IX). \tag{4.23}$$

The first term in Eq. 4.23 represents the Stark shift due to the off-resonant driving of the control qubit with rate η, m_{12} is a scalar denoting the spurious electromagnetic crosstalk between the qubits and μ is our desired ZX coupling rate given as,

$$\mu = \frac{J}{\Delta_{12}} \frac{\alpha_1}{\Delta_{12} + \alpha_1}, \tag{4.24}$$

where α_1 is the anharmonicity of the target qubit.

It has been shown previously that having all the additional terms in Equation 4.23 does not result in a degraded ZX coupling as these terms commute [184]. The only downside of the CR gate is the presence of an always-on ZZ coupling, resulting in a dephasing of the system's evolution. To circumvent this problem, one can try to carefully choose the coupling parameters of the system during the design and simulation phase. The ZZ interaction strength in a two-qubit system is in the form of,

$$ZZ = 2J^2 \frac{\alpha_0 + \alpha_1}{(\Delta_{12} + \alpha_0)(\Delta_{12} - \alpha_1)}. \tag{4.25}$$

To illuminate the basic concepts behind the CR gate, one can look at an analogy with a classical system where the qubits are replaced by the classical oscillators [185] (Fig. 4.13(b)). In this case, since the drive frequency is still in resonance with the target qubit, it will still apply oscillations due to the coupling of the two qubits with a rate g. However, for the control qubit, it will only produce a very small forced oscillations. Therefore, applying a drive to the control qubit with target qubit's resonance frequency results in oscillation in the target qubit, demonstrating the main mechanism behind the CR gate.

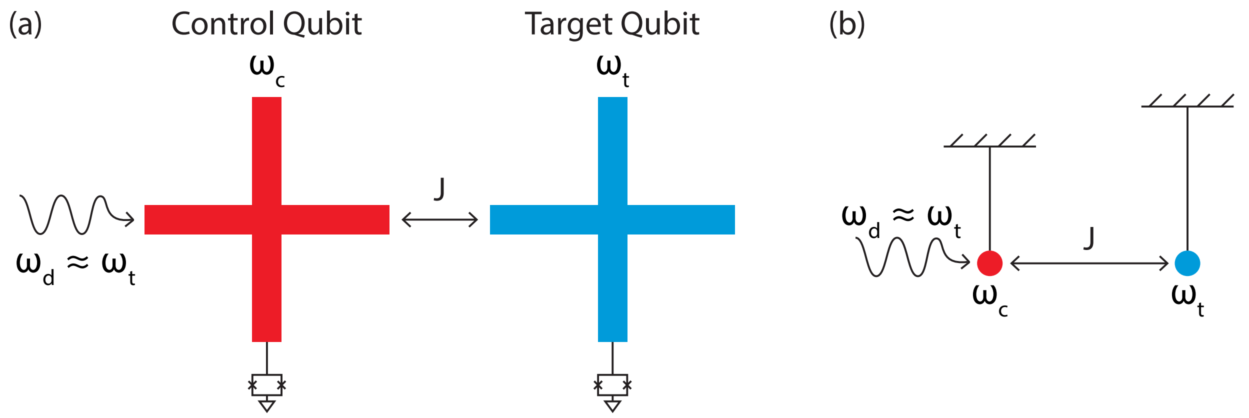

Figure 4.13: Cross-resonance gate explained with cartoons. (a) The basic mechanism behind the CR gate in qubits processors. (b) Utilizing coupled classical oscillators to illuminate the concepts behind the CR gate.

4.5.2 Experimental realization

Now that we have a sense of the theory behind the CR gate, we can look at the experimental protocols needed to tune up the gate. The first step is to bring the qubit frequencies closer together to get higher ZX coupling, therefore a shorter gate time according to Equation. 4.24. The maximum coupling between the qubits is set by the designed coupling between the qubits at resonance and that can be achieved by adjusting the detuning between the qubits and the drive amplitude. Typically, a detuning of ~80 MHz with respect to the other qubit is chosen to both result in a reasonable gate time and a low ZZ interaction strength [186], which is inversely proportional to the qubits' detuning (Eq. 4.25). After adjusting the qubits' detuning to a certain value, we need to apply a microwave signal with the frequency of the target qubit to the control with the control qubit. Next, we can look at the Rabi oscillations of the target qubit vs the CR gate amplitude and duration both with having the control qubit in both its ground and excited state. Figure 4.14 depicts the pulse sequences required to conduct such an experiment. Extracting the frequency of the Rabi oscillations on the target qubit with and without the π-pulse for each drive amplitude will allow us to calculate the effective CR interaction rate as,

$$J_{\mathrm{eff}}/2\pi = \frac{f^{\pi}_{\mathrm{Rabi}} - f_{\mathrm{Rabi}}}{2}. \tag{4.26}$$

From the fitting of the Rabi oscillations depicted in Figure 4.15 for a drive amplitude of 0.72 V, we can extract an effective coupling rate of $J_{\mathrm{eff}}/2\pi \sim 280$ kHz, which corresponds to

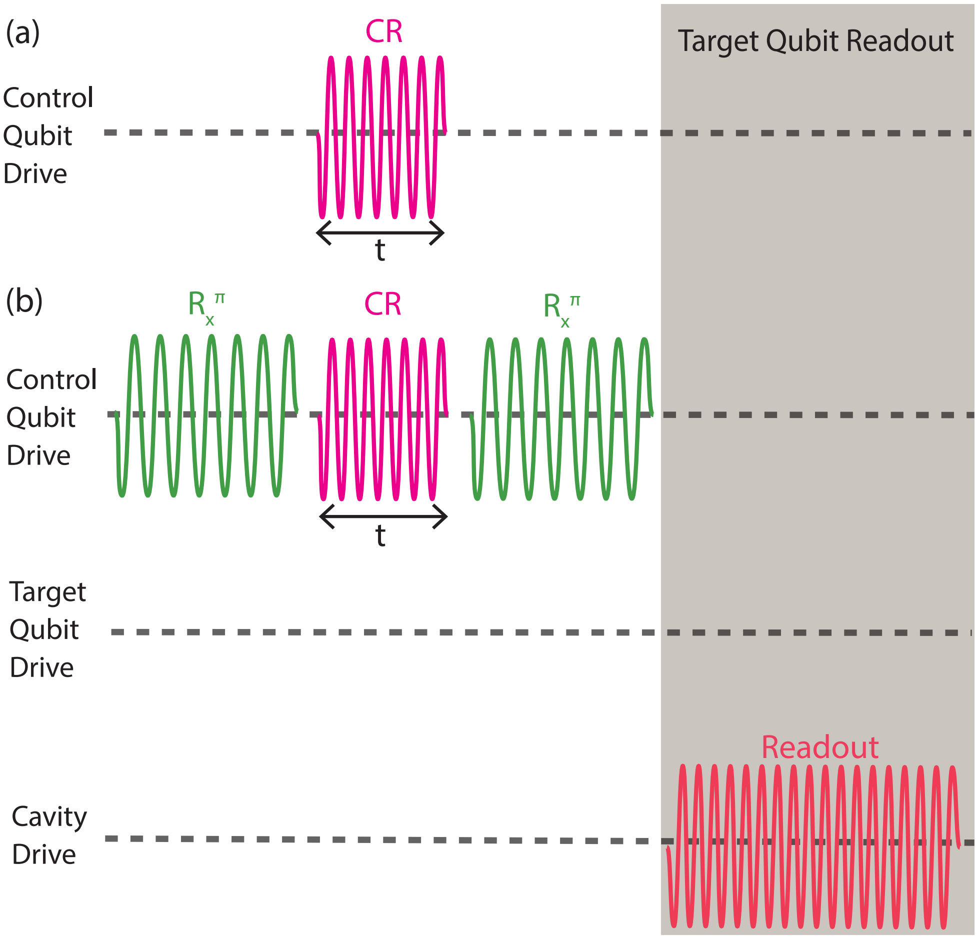

Figure 4.14: Pulse sequences used to calibrate the CR gate time with the control qubit initialized in the (a) ground or (b) excited state.

a gate time of $t_\mathrm{g} = 2\pi/2J_\mathrm{eff} \sim 1.8\ \mu$s. Note that the amplitude of the CR gate should also be adjusted such that the contrast of the two curves shown in Fig. 4.15 is optimal at the desired gate time.

The immediate experiment that follows is to entangle the qubits and characterize the concurrence (Eq. 3.49) as a function of the CR gate time to achieve the largest concurrence value possible. In order to entangle the qubits, first we initialize the control qubit in a superposition state ($|x+\rangle$), immediately apply the CR gate and run two-qubit tomography

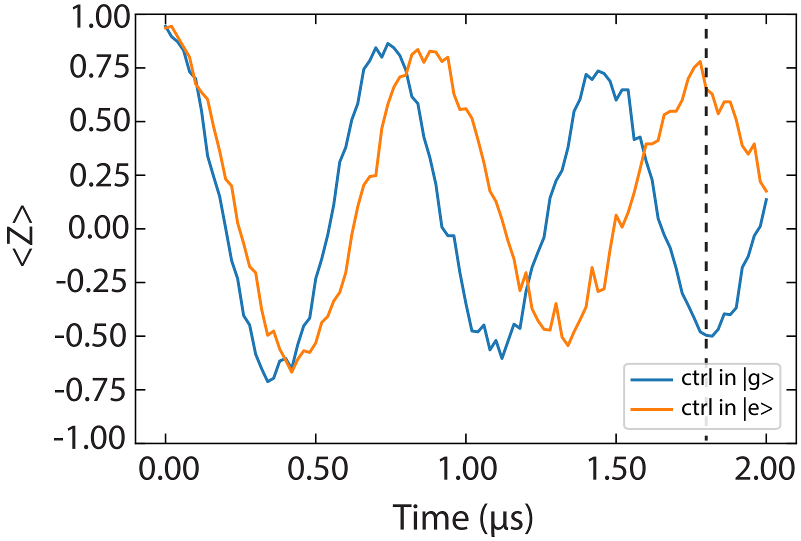

Figure 4.15: Time-varying Rabi oscillations on the target qubit after driving the control qubit using target's resonance frequency. The dashed line indicates the approximate required gate time to realize the CNOT gate.

(Sec. 4.4.2) as shown in Fig. 4.16(a). Knowing the density matrix of the two-qubit system allows us to calculate the concurrence. Now by varying the applied CR gate time we can plot the concurrence as a function of the gate time in our system (Fig. 4.16(b)). As expected, the concurrence reaches its maximum for a gate time close to t_g calculated above and goes back down to zero once we move away from the optimal point. Figure 4.16(c) demonstrates the two-qubit tomography result of a Bell state, $|\psi\rangle = \frac{1}{\sqrt{2}}(|01\rangle + |10\rangle)$, generated utilizing the above scheme for the optimal CR gate time (1.76 μs), resulting in a concurrence of 0.75 with 83% of fidelity.

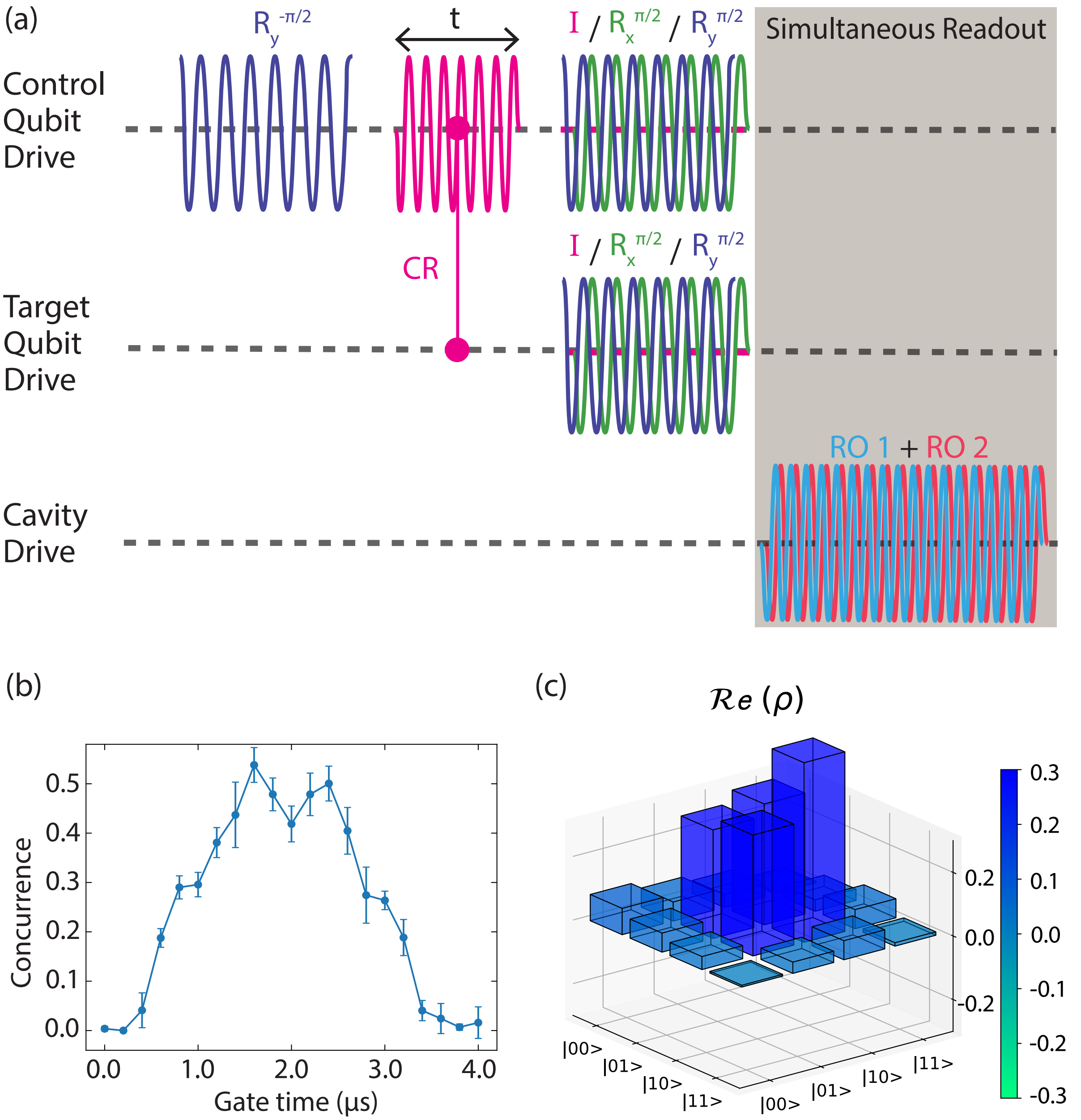

Figure 4.16: Entanglement scheme using the CR gate. (a) The pulse sequence required to generate a Bell state. (b) Gate time calibration by examining the concurrence. (c) Two-qubit tomography of the entangled state after careful gate time/amplitude calibrations.

4.6 Entanglement Dynamics

Having a calibrated CR gate allows us to explore the dynamics of an entangled state during a free evolution. To realize such dynamics, we simply need to add a delay time between the CR gate and the tomography pre-rotation pulses in the sequence shown in Figure 4.16. In this case, we initially prepare an entangled state, let it evolve over a certain amount of time, and finally reconstruct the full two-qubit density matrix at each time step and calculate its concurrence using Equation 3.49. As an initial try, Figure 4.17 shows the evolution of concurrence over a timespan of 2 μs for a detuning of 670 MHz between the system and the environment qubits.

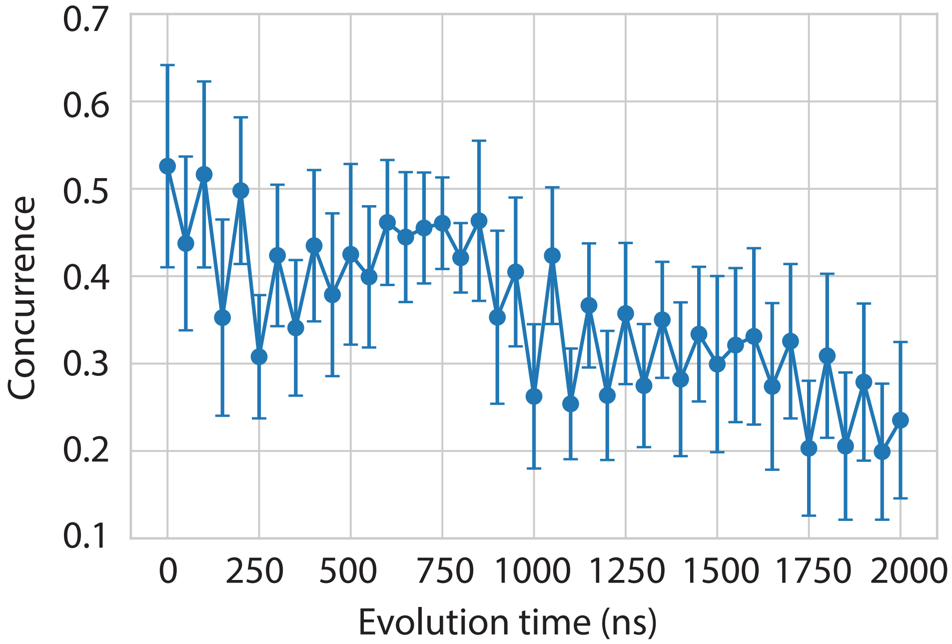

Figure 4.17: The entanglement free evolution over a timespan of 2 μs with a detuning of 670 MHz between the system and environment qubits.

It is anticipated from the numerical simulations (Sec. 4.2) that having a large detuning between the system and the environment qubits, prevents us from capturing the non-Markovian characteristics of the system as shown in Fig. 4.17. The other observation is that measuring each time step ten times over a two-day averaging time, resulted in large error bars. This can be attributed to the flux noise present in the system, injected through the fast flux lines on the device, mainly due to the bad grounding of the electronics and/or the ambient noise present in the laboratory generated by an external source. As a result of these difficulties, connecting the flux line of the environment qubit to a current source significantly shifts the frequency of the system qubit, proving that an extra source of noise has been added to the system.

The next step for this project is to mitigate the noise in the system by studying its spectrum and identifying the major contributing factors to this. Immediately after that, we can bring the environment qubit close to the system qubit and repeat the concurrence evolution to measure the non-Markovianity of the system and investigate the transition from Markovian to non-Markovian regimes as a function of the detuning between the two qubits. Moreover, after realizing a non-Markovian environment, it is a feasible to study the effects of the memory kernel in the evolution of the system by reconstructing the Nakajima-Zwanzig master equation using the techniques described in Section 3.1.3.

References

[1] A. J. Leggett. “Macroscopic Quantum Systems and the Quantum Theory of Measurement”. *Progress of Theoretical Physics Supplement* 69 (Mar. 1980), pp. 80–100. DOI: `10.1143/PTP.69.80`. eprint: `https://academic.oup.com/ptps/article-pdf/doi/10.1143/PTP.69.80/5356381/69-80.pdf` (Cited on page 1).

[2] M. Tinkham. *Introduction to superconductivity.* Mineola, N.Y.: Dover Publications, 2004 (Cited on pages 1, 9).

[3] M. H. Devoret, J. M. Martinis, and J. Clarke. “Measurements of Macroscopic Quantum Tunneling out of the Zero-Voltage State of a Current-Biased Josephson Junction”. *Phys. Rev. Lett.* 55 (18 1985), pp. 1908–1911. DOI: `10.1103/PhysRevLett.55.1908` (Cited on page 1).

[4] J. M. Martinis, M. H. Devoret, and J. Clarke. “Energy-Level Quantization in the Zero-Voltage State of a Current-Biased Josephson Junction”. *Phys. Rev. Lett.* 55 (15 1985), pp. 1543–1546. DOI: `10.1103/PhysRevLett.55.1543` (Cited on page 1).

[5] T. Yamamoto, Y. A. Pashkin, O. Astafiev, Y. Nakamura, et al. “Demonstration of conditional gate operation using superconducting charge qubits”. *Nature* 425.6961 (2003), pp. 941–944. DOI: `10.1038/nature02015` (Cited on page 1).

[6] C.-P. Yang, S.-I. Chu, and S. Han. “Possible realization of entanglement, logical gates, and quantum-information transfer with superconducting-quantum-interference-device qubits in cavity QED”. *Phys. Rev. A* 67 (4 2003), p. 042311. DOI: `10.1103/PhysRevA.67.042311` (Cited on page 2).

[7] A. Blais, R.-S. Huang, A. Wallraff, S. M. Girvin, et al. “Cavity quantum electrodynamics for superconducting electrical circuits: An architecture for quantum computation”. *Phys. Rev. A* 69 (6 2004), p. 062320. DOI: `10.1103/PhysRevA.69.062320` (Cited on pages 2, 13).

[8] J. Koch, T. M. Yu, J. Gambetta, A. A. Houck, et al. “Charge-insensitive qubit design derived from the Cooper pair box”. *Phys. Rev. A* 76 (4 2007), p. 042319. DOI: `10.1103/PhysRevA.76.042319` (Cited on pages 2, 5, 88).

[9] L. DiCarlo, J. M. Chow, J. M. Gambetta, L. S. Bishop, et al. “Demonstration of two-qubit algorithms with a superconducting quantum processor”. *Nature* 460.7252 (2009), pp. 240–244. DOI: `10.1038/nature08121` (Cited on page 3).

[10] Y. Zheng, C. Song, M.-C. Chen, B. Xia, et al. “Solving Systems of Linear Equations with a Superconducting Quantum Processor”. *Phys. Rev. Lett.* 118 (21 2017), p. 210504. DOI: `10.1103/PhysRevLett.118.210504` (Cited on page 3).

[11] H.-L. Huang, Y.-W. Zhao, T. Li, F.-G. Li, et al. “Homomorphic Encryption Experiments on IBM’s Cloud Quantum Computing Platform” (2017). arXiv: `1612.02886 [cs.CR]` (Cited on page 3).

[12] M. D. Reed, L. DiCarlo, S. E. Nigg, L. Sun, et al. “Realization of three-qubit quantum error correction with superconducting circuits”. *Nature* 482.7385 (2012), pp. 382–385. DOI: `10.1038/nature10786` (Cited on page 3).

[13] J. M. Chow, J. M. Gambetta, E. Magesan, D. W. Abraham, et al. “Implementing a strand of a scalable fault-tolerant quantum computing fabric”. *Nature Communications* 5.1 (2014), p. 4015. DOI: `10.1038/ncomms5015` (Cited on page 3).

[14] J. Kelly, R. Barends, A. G. Fowler, A. Megrant, et al. “State preservation by repetitive error detection in a superconducting quantum circuit”. *Nature* 519.7541 (2015), pp. 66–69. DOI: `10.1038/nature14270` (Cited on page 3).

[15] C. K. Andersen, A. Remm, S. Lazar, S. Krinner, et al. “Repeated quantum error detection in a surface code”. *Nature Physics* 16.8 (2020), pp. 875–880. DOI: `10.1038/s41567-020-0920-y` (Cited on page 3).

[16] F. Arute, K. Arya, R. Babbush, D. Bacon, et al. “Quantum supremacy using a programmable superconducting processor”. *Nature* 574.7779 (2019), pp. 505–510. DOI: `10.1038/s41586-019-1666-5` (Cited on pages 3, 22).

[17] C. Bartram, T. Braine, R. Cervantes, N. Crisosto, et al. “Dark matter axion search using a Josephson Traveling wave parametric amplifier”. *Review of Scientific Instruments* 94.4 (2023), p. 044703. DOI: `10.1063/5.0122907`. eprint: `https://doi.org/10.1063/5.0122907` (Cited on page 3).

[18] K. W. Murch, U. Vool, D. Zhou, S. J. Weber, et al. “Cavity-Assisted Quantum Bath Engineering”. *Phys. Rev. Lett.* 109 (18 2012), p. 183602. DOI: `10.1103/PhysRevLett.109.183602` (Cited on page 3).

[19] S. Shankar, M. Hatridge, Z. Leghtas, K. M. Sliwa, et al. “Autonomously stabilized entanglement between two superconducting quantum bits”. *Nature* 504.7480 (2013), pp. 419–422. DOI: `10.1038/nature12802` (Cited on page 3).

[20] M. E. Kimchi-Schwartz, L. Martin, E. Flurin, C. Aron, et al. “Stabilizing Entanglement via Symmetry-Selective Bath Engineering in Superconducting Qubits”. *Phys. Rev. Lett.* 116 (24 2016), p. 240503. DOI: `10.1103/PhysRevLett.116.240503` (Cited on page 3).

[21] L. Bretheau, P. Campagne-Ibarcq, E. Flurin, F. Mallet, et al. “Quantum dynamics of an electromagnetic mode that cannot contain N photons”. *Science* 348.6236 (2015), pp. 776–779. DOI: `10.1126/science.1259345`. eprint: `https://www.science.org/doi/pdf/10.1126/science.1259345` (Cited on page 3).

[22] C. A. Rodriguez-Rosario and E. C. G. Sudarshan. “Non-Markovian Open Quantum Systems” (2008). arXiv: `0803.1183 [quant-ph]` (Cited on page 4).

[23] F. Rozpędek, K. Noh, Q. Xu, S. Guha, et al. “Quantum repeaters based on concatenated bosonic and discrete-variable quantum codes”. *npj Quantum Information* 7.1 (2021), p. 102. DOI: `10.1038/s41534-021-00438-7` (Cited on page 4).

[24] A. Orieux, A. D’Arrigo, G. Ferranti, R. L. Franco, et al. “Experimental on-demand recovery of entanglement by local operations within non-Markovian dynamics”. *Scientific Reports* 5.1 (2015), p. 8575. DOI: `10.1038/srep08575` (Cited on page 4).

[25] J.-S. Xu, C.-F. Li, M. Gong, X.-B. Zou, et al. “Experimental Demonstration of Photonic Entanglement Collapse and Revival”. *Phys. Rev. Lett.* 104 (10 2010), p. 100502. DOI: `10.1103/PhysRevLett.104.100502` (Cited on page 4).

[26] A. Mortezapour, M. A. Borji, and R. L. Franco. “Protecting entanglement by adjusting the velocities of moving qubits inside non-Markovian environments”. *Laser Physics Letters* 14.5 (2017), p. 055201. DOI: `10.1088/1612-202X/aa63c5` (Cited on page 4).

[27] A. Ask and G. Johansson. “Non-Markovian Steady States of a Driven Two-Level System”. *Phys. Rev. Lett.* 128 (8 2022), p. 083603. DOI: `10.1103/PhysRevLett.128.083603` (Cited on page 4).

[28] A. J. Landahl, J. T. Anderson, and P. R. Rice. *Fault-tolerant quantum computing with color codes.* 2011. DOI: `10.48550/ARXIV.1108.5738` (Cited on pages 4, 73).

[29] S. J. Devitt, W. J. Munro, and K. Nemoto. “Quantum error correction for beginners”. *Reports on Progress in Physics* 76.7 (2013), p. 076001. DOI: `10.1088/0034-4885/76/7/076001` (Cited on page 4).

[30] H. P. Breuer, E. Laine, and J. Piilo. “Measure for the Degree of Non-Markovian Behavior of Quantum Processes in Open Systems”. *Phys. Rev. Lett.* 103 (21 2009), p. 210401. DOI: `10.1103/PhysRevLett.103.210401` (Cited on pages 4, 64, 66, 73).

[31] A. Rivas, S. F. Huelga, and M. B. Plenio. “Entanglement and Non-Markovianity of Quantum Evolutions”. *Physical Review Letters* 105.5 (2010). DOI: `10.1103/physrevlett.105.050403` (Cited on pages 4, 70, 71, 73).

[32] M. H. Devoret. *Fluctuations quantiques : Les Houches, Session LXIII, 27 juin-28 juillet 1995.* Amsterdam: Elsevier, 1997 (Cited on page 5).

[33] J. J. Sakurai and J. Napolitano. *Modern Quantum Mechanics.* 2nd ed. Cambridge University Press, 2017. DOI: `10.1017/9781108499996` (Cited on pages 7, 15, 69).

[34] B. D. Josephson. “Possible new effects in superconductive tunnelling”. *Physics Letters* 1.7 (1962), pp. 251–253. DOI: `https://doi.org/10.1016/0031-9163(62)91369-0` (Cited on page 7).

[35] M. Reagor, C. B. Osborn, N. Tezak, A. Staley, et al. “Demonstration of universal parametric entangling gates on a multi-qubit lattice”. *Science Advances* 4.2 (2018), eaao3603. DOI: `10.1126/sciadv.aao3603`. eprint: `https://www.science.org/doi/pdf/10.1126/sciadv.aao3603` (Cited on page 9).

[36] S. K. Tolpygo, V. Bolkhovsky, R. Rastogi, S. Zarr, et al. "Advanced Fabrication Processes for Superconductor Electronics: Current Status and New Developments". *IEEE Transactions on Applied Superconductivity* 29.5 (2019), pp. 1–13. DOI: `10.1109/TASC.2019.2904919` (Cited on page 9).

[37] E. T. Jaynes and F. W. Cummings. "Comparison of quantum and semiclassical radiation theories with application to the beam maser". *Proceedings of the IEEE* 51.1 (1963), pp. 89–109. DOI: `10.1109/PROC.1963.1664` (Cited on page 12).

[38] M. Naghiloo. *Introduction to Experimental Quantum Measurement with Superconducting Qubits.* 2019. DOI: `10.48550/ARXIV.1904.09291` (Cited on pages 12, 18, 92).

[39] J. R. Schrieffer and P. A. Wolff. "Relation between the Anderson and Kondo Hamiltonians". *Phys. Rev.* 149 (2 1966), pp. 491–492. DOI: `10.1103/PhysRev.149.491` (Cited on page 12).

[40] V. B. Braginsky and F. Y. Khalili. "Quantum nondemolition measurements: the route from toys to tools". *Rev. Mod. Phys.* 68 (1 1996), pp. 1–11. DOI: `10.1103/RevModPhys.68.1` (Cited on page 13).

[41] D. I. Schuster, A. Wallraff, A. Blais, L. Frunzio, et al. "ac Stark Shift and Dephasing of a Superconducting Qubit Strongly Coupled to a Cavity Field". *Phys. Rev. Lett.* 94 (12 2005), p. 123602. DOI: `10.1103/PhysRevLett.94.123602` (Cited on page 14).

[42] J. Gambetta, A. Blais, D. I. Schuster, A. Wallraff, et al. "Qubit-photon interactions in a cavity: Measurement-induced dephasing and number splitting". *Phys. Rev. A* 74 (4 2006), p. 042318. DOI: `10.1103/PhysRevA.74.042318` (Cited on page 14).

[43] P. Krantz, M. Kjaergaard, F. Yan, T. P. Orlando, et al. "A quantum engineer's guide to superconducting qubits". *Applied Physics Reviews* 6.2 (2019), p. 021318. DOI: `10.1063/1.5089550` (Cited on page 16).

[44] D. Kowsari, K. Zheng, J. T. Monroe, N. J. Thobaben, et al. "Fabrication and surface treatment of electron-beam evaporated niobium for low-loss coplanar waveguide resonators". *Applied Physics Letters* 119.13 (2021), p. 132601. DOI: `10.1063/5.0066441`. eprint: `https://doi.org/10.1063/5.0066441` (Cited on pages 21, 42, 45, 49).

[45] P. Jurcevic, A. Javadi-Abhari, L. S. Bishop, I. Lauer, et al. "Demonstration of quantum volume 64 on a superconducting quantum computing system". *Quantum Science and Technology* 6.2 (2021). DOI: `10.1088/2058-9565/abe519`. arXiv: `2008.08571` (Cited on page 22).

[46] Y. Wu, W.-S. Bao, S. Cao, F. Chen, et al. "Strong quantum computational advantage using a superconducting quantum processor" (2021). arXiv: `2106.14734` (Cited on page 22).

[47] P. J. De Visser, D. J. Goldie, P. Diener, S. Withington, et al. "Evidence of a nonequilibrium distribution of quasiparticles in the microwave response of a superconducting aluminum resonator". *Physical Review Letters* 112.4 (2014), pp. 1–5. DOI: `10.1103/PhysRevLett.112.047004`. arXiv: `1306.4992` (Cited on page 22).

[48] R. Barends, J. Wenner, M. Lenander, Y. Chen, et al. "Minimizing quasiparticle generation from stray infrared light in superconducting quantum circuits". *Applied Physics Letters* 99.11 (2011), pp. 1–4. DOI: `10.1063/1.3638063` (Cited on page 22).

[49] A. D. Córcoles, J. M. Chow, J. M. Gambetta, C. Rigetti, et al. "Protecting superconducting qubits from radiation". *Applied Physics Letters* 99.18 (2011). DOI: `10.1063/1.3658630` (Cited on page 22).

[50] C. Song, T. W. Heitmann, M. P. Defeo, K. Yu, et al. "Microwave response of vortices in superconducting thin films of Re and Al". *Physical Review B - Condensed Matter and Materials Physics* 79.17 (2009), pp. 1–9. DOI: `10.1103/PhysRevB.79.174512`. arXiv: `0812.3645` (Cited on page 22).

[51] J. M. Sage, V. Bolkhovsky, W. D. Oliver, B. Turek, et al. "Study of loss in superconducting coplanar waveguide resonators". *Journal of Applied Physics* (2011). DOI: `10.1063/1.3552890`. arXiv: `1010.6063` (Cited on pages 22, 46, 48).

[52] J. M. Kreikebaum, A. Dove, W. Livingston, E. Kim, et al. "Optimization of infrared and magnetic shielding of superconducting TiN and Al coplanar microwave resonators". *Superconductor Science and Technology* 29.10 (2016). DOI: `10.1088/0953-2048/29/10/104002` (Cited on page 22).

[53] M. Sandberg, M. R. Vissers, T. A. Ohki, J. Gao, et al. "Radiation-suppressed superconducting quantum bit in a planar geometry". *Applied Physics Letters* 102.7 (2013). DOI: `10.1063/1.4792698` (Cited on page 22).

[54] B. Chiaro, A. Megrant, A. Dunsworth, Z. Chen, et al. "Dielectric surface loss in superconducting resonators with flux-trapping holes". *Superconductor Science and Technology* 29.10 (2016). DOI: `10.1088/0953-2048/29/10/104006`. arXiv: `1607.05841` (Cited on page 22).

[55] J. Lisenfeld, A. Bilmes, A. Megrant, R. Barends, et al. "Electric field spectroscopy of material defects in transmon qubits". *npj Quantum Information* 5.1 (2019), pp. 1–6. DOI: `10.1038/s41534-019-0224-1`. arXiv: `1909.09749` (Cited on page 22).

[56] S. E. de Graaf, L. Faoro, L. B. Ioffe, S. Mahashabde, et al. "Two-level systems in superconducting quantum devices due to trapped quasiparticles". *Science Advances* 6.51 (2020), pp. 1–9. DOI: `10.1126/SCIADV.ABC5055`. arXiv: `2004.02485` (Cited on page 22).

[57] D. Niepce, J. J. Burnett, M. G. Latorre, and J. Bylander. "Geometric scaling of two-level-system loss in superconducting resonators". *Superconductor Science and Technology* 33.2 (2020). DOI: `10.1088/1361-6668/ab6179`. arXiv: `1908.02606` (Cited on page 22).

[58] J. Gao, M. Daal, A. Vayonakis, S. Kumar, et al. "Experimental evidence for a surface distribution of two-level systems in superconducting lithographed microwave resonators". *Applied Physics Letters* 92.15 (2008). DOI: `10.1063/1.2906373`. arXiv: `0802.4457` (Cited on pages 22, 23, 38, 48).

[59] D. S. Wisbey, J. Gao, M. R. Vissers, F. C. Da Silva, et al. "Effect of metal/substrate interfaces on radio-frequency loss in superconducting coplanar waveguides". *Journal of Applied Physics* 108.9 (2010), pp. 8–12. DOI: `10.1063/1.3499608` (Cited on pages 22, 46, 48).

[60] A. Bilmes, A. Megrant, P. Klimov, G. Weiss, et al. "Resolving the positions of defects in superconducting quantum bits". *Scientific Reports* 10.1 (2020), pp. 1–6. DOI: `10.1038/s41598-020-59749-y`. arXiv: `1911.08246` (Cited on page 22).

[61] L. Grünhaupt, U. Von Lüpke, D. Gusenkova, S. T. Skacel, et al. "An argon ion beam milling process for native AlOx layers enabling coherent superconducting contacts". *Applied Physics Letters* 111.7 (2017). DOI: `10.1063/1.4990491`. arXiv: `1706.06424` (Cited on page 22).

[62] G. Calusine, A. Melville, W. Woods, R. Das, et al. "Analysis and mitigation of interface losses in trenched superconducting coplanar waveguide resonators". *Applied Physics Letters* 112.6 (2018). DOI: `10.1063/1.5006888`. arXiv: `1709.10015` (Cited on page 22).

[63] A. P. Place, L. V. Rodgers, P. Mundada, B. M. Smitham, et al. "New material platform for superconducting transmon qubits with coherence times exceeding 0.3 milliseconds". *Nature Communications* 12.1 (2021). DOI: `10.1038/s41467-021-22030-5`. arXiv: `2003.00024` (Cited on pages 22, 39).

[64] J. T. Monroe, D. Kowsari, K. Zheng, J. Brewster, et al. "Optical Direct Write of Dolan-Bridge Junctions for Transmon Qubits" (2021), pp. 1–7. arXiv: `2106.09034` (Cited on page 22).

[65] J. Halbritter. "On the oxidation and on the superconductivity of niobium". *Applied Physics A Solids and Surfaces* 43.1 (1987), pp. 1–28. DOI: `10.1007/BF00615201` (Cited on pages 22, 39).

[66] A. Nersisyan, E. A. Sete, S. Stanwyck, A. Bestwick, et al. "Manufacturing low dissipation superconducting quantum processors". *Technical Digest - International Electron Devices Meeting, IEDM* 2019-Decem (2019). DOI: `10.1109/IEDM19573.2019.8993458`. arXiv: `1901.08042` (Cited on pages 22, 25).

[67] M. S. Blok, V. V. Ramasesh, T. Schuster, K. O'Brien, et al. "Quantum Information Scrambling on a Superconducting Qutrit Processor". *Physical Review X* 11.2 (2021), p. 21010. DOI: `10.1103/PhysRevX.11.021010`. arXiv: `2003.03307` (Cited on page 22).

[68] D. Bach, H. Störmer, R. Schneider, D. Gerthsen, et al. "EELS investigations of different niobium oxide phases". *Microscopy and Microanalysis* (2006). DOI: `10.1017/S1431927606060521` (Cited on page 22).

[69] D. Bach. “EELS investigations of stoichiometric niobium oxides and niobium-based capacitors”. PhD thesis. 2009. DOI: `10.5445/IR/1000012945` (Cited on page 22).

[70] M. V. P. Altoé, A. Banerjee, C. Berk, A. Hajr, et al. “Localization and reduction of superconducting quantum coherent circuit losses” (2020), pp. 1–20. arXiv: `2012.07604` (Cited on pages 22, 23, 40, 48).

[71] J. Verjauw, A. Potocnik, M. Mongillo, R. Acharya, et al. “Investigation of Microwave Loss Induced by Oxide Regrowth in High-Q Niobium Resonators”. *Phys. Rev. Appl.* 16 (1 2021), p. 014018. DOI: `10.1103/PhysRevApplied.16.014018` (Cited on pages 22, 25, 43, 48).

[72] M. Siemers, A. Pflug, T. Melzig, K. Gehrke, et al. “Model based investigation of Ar+ ion damage in DC magnetron sputtering”. *Surface and Coatings Technology* (2014). DOI: `10.1016/j.surfcoat.2013.09.025` (Cited on page 23).

[73] F. M. D’Heurle. “Aluminum films deposited by rf sputtering”. *Metallurgical and Materials Transactions B* (1970). DOI: `10.1007/BF02811600` (Cited on page 23).

[74] S. Morohashi, N. Takeda, S. Tsujimura, M. Kawanishi, et al. “Characteristics of superconducting Nb layer fabricated using high-vacuum electron beam evaporation”. *Japanese Journal of Applied Physics, Part 1: Regular Papers and Short Notes and Review Papers* 40.2 A (2001), pp. 576–579. DOI: `10.1143/jjap.40.576` (Cited on pages 23, 39, 41).

[75] D. P. Pappas, M. R. Vissers, D. S. Wisbey, J. S. Kline, et al. “Two level system loss in superconducting microwave resonators”. In: *IEEE Transactions on Applied Superconductivity.* 2011. DOI: `10.1109/TASC.2010.2097578` (Cited on pages 23, 48).

[76] X. Zhang, P. Zheng, Y. Ma, Y. Jiang, et al. “Atomic-scale understanding of oxidation mechanisms of materials by computational approaches: A review”. *Materials and Design* 217 (2022), p. 110605. DOI: `https://doi.org/10.1016/j.matdes.2022.110605` (Cited on page 23).

[77] D. R. Lide. *CRC handbook of chemistry and physics.* Vol. 85. CRC press, 2004 (Cited on pages 25, 27).

[78] W. S. Williams. “Transition metal carbides, nitrides, and borides for electronic applications”. *JOM* 49.3 (1997), pp. 38–42. DOI: `10.1007/BF02914655` (Cited on page 25).

[79] A. J. Deardo. “Niobium in modern steels”. *International Materials Reviews* 48.6 (2003), pp. 371–402. DOI: `10.1179/095066003225008833`. eprint: `https://doi.org/10.1179/095066003225008833` (Cited on page 25).

[80] L. Kommel, E. Kimmari, M. Saarna, and M. Viljus. “Processing and properties of bulk ultrafine-grained pure niobium”. *Journal of Materials Science* 48.13 (2013), pp. 4723–4729. DOI: `10.1007/s10853-013-7210-3` (Cited on page 25).

[81] J. Halbritter. “On the oxidation and on the superconductivity of niobium”. *Applied Physics A* 43.1 (1987), pp. 1–28. DOI: `10.1007/BF00615201` (Cited on pages 25, 26).

[82] V. Bouchiat, M. Faucher, C. Thirion, W. Wernsdorfer, et al. “Josephson junctions and superconducting quantum interference devices made by local oxidation of niobium ultrathin films”. *Applied Physics Letters* 79.1 (2001), pp. 123–125. DOI: `10.1063/1.1382626`. eprint: `https://doi.org/10.1063/1.1382626` (Cited on page 25).

[83] V. F. Shamrai, Y. V. Blagoveshchenski, A. S. Gordeev, A. V. Mitin, et al. “Structural states and electrical conductivity of oxidized niobium nanopowders”. *Russian Metallurgy (Metally)* 2007.4 (2007), pp. 322–326. DOI: `10.1134/S0036029507040106` (Cited on page 26).

[84] M. Grundner and J. Halbritter. “XPS and AES studies on oxide growth and oxide coatings on niobium”. *Journal of Applied Physics* 51.1 (1980), pp. 397–405. DOI: `10.1063/1.327386`. eprint: `https://doi.org/10.1063/1.327386` (Cited on page 26).

[85] K. Zheng, D. Kowsari, N. J. Thobaben, X. Du, et al. “Nitrogen plasma passivated niobium resonators for superconducting quantum circuits”. *Applied Physics Letters* 120.10 (2022), p. 102601. DOI: `10.1063/5.0082755`. eprint: `https://doi.org/10.1063/5.0082755` (Cited on page 26).

[86] A. L. Bowman, T. C. Wallace, J. L. Yarnell, and R. G. Wenzel. “The crystal structure of niobium monoxide”. *Acta Crystallographica* 21.5 (1966), p. 843. DOI: `10.1107/S0365110X66004043` (Cited on page 26).

[87] E. Kurmaev, A Moewes, O. Bureev, I. Nekrasov, et al. “Electronic structure of niobium oxides”. *Journal of Alloys and Compounds* 347.1 (2002), pp. 213–218. DOI: `https://doi.org/10.1016/S0925-8388(02)00765-X` (Cited on page 26).

[88] E. R. Pollard Jr. “Electronic properties of niobium monoxide.” PhD thesis. Massachusetts Institute of Technology, 1968 (Cited on page 26).

[89] D. Bach. “EELS Investigations of Stoichiometric Niobium Oxides and Niobium-based Capacitors” (2009), p. 210 (Cited on page 26).

[90] J. K. Hulm, C. K. Jones, R. A. Hein, and J. W. Gibson. “Superconductivity in the TiO and NbO systems”. *Journal of Low Temperature Physics* 7.3 (1972), pp. 291–307. DOI: `10.1007/BF00660068` (Cited on page 26).

[91] Y. Qiu, D. Smyth, and J. Kimmel. “The Stabilization of Niobium-Based Solid Electrolyte Capacitors”. *Active and Passive Electronic Components* 25 (2002), p. 452458. DOI: `10.1080/08827510212343` (Cited on page 27).

[92] A. K. Cheetham and C. N. R. Rao. “A neutron diffraction study of niobium dioxide”. *Acta Crystallographica Section B* 32.5 (1976), pp. 1579–1580. DOI: `10.1107/S0567740876005876` (Cited on page 27).

[93] S. K. E. Forghany and J. S. Anderson. “Reduction and polymorphic transformation of B-Nb2O5”. *J. Chem. Soc. Dalton Trans.* (1 1981), pp. 255–261. DOI: `10.1039/DT9810000255` (Cited on page 27).

[94] D. S. Rimai and R. J. Sladek. "Pressure dependences of the elastic constants of semiconducting NbO_2 at 296 K". *Phys. Rev. B* 18 (6 1978), pp. 2807–2811. DOI: `10.1103/PhysRevB.18.2807` (Cited on page 27).

[95] R. Janninck and D. Whitmore. "Electrical conductivity and thermoelectric power of niobium dioxide". *Journal of Physics and Chemistry of Solids* 27.6 (1966), pp. 1183–1187. DOI: `https://doi.org/10.1016/0022-3697(66)90094-1` (Cited on page 27).

[96] A. O'Hara, T. N. Nunley, A. B. Posadas, S. Zollner, et al. "Electronic and optical properties of NbO2". *Journal of Applied Physics* 116.21 (2014), p. 213705. DOI: `10.1063/1.4903067`. eprint: `https://doi.org/10.1063/1.4903067` (Cited on page 27).

[97] S. Kim, J. Park, J. Woo, C. Cho, et al. "Threshold-switching characteristics of a nanothin-NbO2-layer-based Pt/NbO2/Pt stack for use in cross-point-type resistive memories". *Microelectronic Engineering* 107 (2013), pp. 33–36. DOI: `https://doi.org/10.1016/j.mee.2013.02.084` (Cited on page 27).

[98] S. Helali, A. Abdelghani, I. Hafaiedh, C. Martelet, et al. "Functionalization of niobium electrodes for the construction of impedimetric biosensors". *Materials Science and Engineering: C* 28.5 (2008). MADICA 2006 Conference, Fifth Maghreb-Europe Meeting on Materials and their Applicatons for Devices and Physical, Chemical and Biological Sensors, pp. 826–830. DOI: `https://doi.org/10.1016/j.msec.2007.10.078` (Cited on page 27).

[99] S.-H. Lee, H.-N. Yoon, I.-S. Yoon, and B.-S. Kim. "Single crystalline NbO2 nanowire synthesis by chemical vapor transport method". *Bulletin of the Korean Chemical Society* 33.3 (2012), pp. 839–842 (Cited on page 27).

[100] M. Soares, S. Leite, C. Nico, M. Peres, et al. "Effect of processing method on physical properties of Nb2O5". *Journal of the European Ceramic Society* 31.4 (2011), pp. 501–506. DOI: `https://doi.org/10.1016/j.jeurceramsoc.2010.10.024` (Cited on page 28).

[101] A. L. Viet, M. V. Reddy, R. Jose, B. V. R. Chowdari, et al. "Nanostructured Nb2O5 Polymorphs by Electrospinning for Rechargeable Lithium Batteries". *The Journal of Physical Chemistry C* 114.1 (Jan. 2010), pp. 664–671. DOI: `10.1021/jp9088589` (Cited on page 28).

[102] A. Le Viet, R. Jose, M. V. Reddy, B. V. R. Chowdari, et al. "Nb2O5 Photoelectrodes for Dye-Sensitized Solar Cells: Choice of the Polymorph". *The Journal of Physical Chemistry C* 114.49 (Dec. 2010), pp. 21795–21800. DOI: `10.1021/jp106515k` (Cited on page 28).

[103] C. Valencia-Balvín, S. Pérez-Walton, G. Dalpian, and J. Osorio-Guillén. "First-principles equation of state and phase stability of niobium pentoxide". *Computational Materials Science* 81 (2014), pp. 133–140. DOI: `https://doi.org/10.1016/j.commatsci.2013.07.032` (Cited on page 28).

[104] N. Kumagai, Y. Koishikawa, S. Komaba, and N. Koshiba. “Thermodynamics and Kinetics of Lithium Intercalation into Nb2O5 Electrodes for a 2 V Rechargeable Lithium Battery”. *Journal of The Electrochemical Society* 146.9 (1999), p. 3203. DOI: `10.1149/1.1392455` (Cited on page 28).

[105] R. Gruehn. “Eine weitere neue Modifikation des niobpentoxids”. *Journal of the Less Common Metals* 11.2 (1966), pp. 119–126. DOI: `https://doi.org/10.1016/0022-5088(66)90076-2` (Cited on page 28).

[106] H. Schäfer, R. Gruehn, and F. Schulte. “The Modifications of Niobium Pentoxide”. *Angewandte Chemie International Edition in English* 5.1 (1966), pp. 40–52. DOI: `https://doi.org/10.1002/anie.196600401`. eprint: `https://onlinelibrary.wiley.com/doi/pdf/10.1002/anie.196600401` (Cited on page 28).

[107] L. Chua. “Memristor-The missing circuit element”. *IEEE Transactions on Circuit Theory* 18.5 (1971), pp. 507–519. DOI: `10.1109/TCT.1971.1083337` (Cited on page 28).

[108] J. Niebuhr. “Die niederen Oxide des Niobs”. *Journal of the Less Common Metals* 11.3 (1966), pp. 191–203. DOI: `https://doi.org/10.1016/0022-5088(66)90005-1` (Cited on page 29).

[109] J. F. Marucco. “Electrical resistance and defect structure of stable and metastable phases of the system Nb12O29–Nb2O5 between 800 and 1100 °C”. *The Journal of Chemical Physics* 70.2 (1979), pp. 649–654. DOI: `10.1063/1.437545`. eprint: `https://aip.scitation.org/doi/pdf/10.1063/1.437545` (Cited on page 29).

[110] C. Nico, T. Monteiro, and M. P. Graça. *Niobium oxides and niobates physical properties: Review and prospects.* 2016. DOI: `10.1016/j.pmatsci.2016.02.001` (Cited on pages 29, 44).

[111] J. Gao. “The Physics of Superconducting Microwave Resonators Thesis by”. 2008 (2008) (Cited on pages 29, 38).

[112] J. M. Martinis, K. B. Cooper, R. McDermott, M. Steffen, et al. “Decoherence in Josephson Qubits from Dielectric Loss”. *Phys. Rev. Lett.* 95 (21 2005), p. 210503. DOI: `10.1103/PhysRevLett.95.210503` (Cited on page 29).

[113] C. Müller, J. H. Cole, and J. Lisenfeld. “Towards understanding two-level-systems in amorphous solids: insights from quantum circuits”. *Reports on Progress in Physics* 82.12 (2019), p. 124501 (Cited on page 29).

[114] L. Gordon, H. Abu-Farsakh, A. Janotti, and C. G. Van de Walle. “Hydrogen bonds in Al2O3 as dissipative two-level systems in superconducting qubits”. *Scientific Reports* 4.1 (2014), p. 7590. DOI: `10.1038/srep07590` (Cited on page 29).

[115] A. Melville, G. Calusine, W. Woods, K. Serniak, et al. “Comparison of dielectric loss in titanium nitride and aluminum superconducting resonators”. *Applied Physics Letters* 117.12 (2020), p. 124004 (Cited on pages 30, 48).

[116] P. W. Anderson, B. I. Halperin, and C. M. Varma. "Anomalous low-temperature thermal properties of glasses and spin glasses". *The Philosophical Magazine: A Journal of Theoretical Experimental and Applied Physics* 25.1 (1972), pp. 1–9. DOI: `10.1080/14786437208229210`. eprint: `https://doi.org/10.1080/14786437208229210` (Cited on page 30).

[117] W. A. Phillips. "Two-level states in glasses". 50.12 (1987), p. 1657. DOI: `10.1088/0034-4885/50/12/003` (Cited on page 30).

[118] S. Hunklinger and W. Arnold. "3 - Ultrasonic Properties of Glasses at Low Temperatures". In: ed. by W. P. Mason and R. Thurston. Vol. 12. Physical Acoustics. Academic Press, 1976, pp. 155–215. DOI: `https://doi.org/10.1016/B978-0-12-477912-9.50008-4` (Cited on page 32).

[119] L. Hilico, C. Fabre, S. Reynaud, and E. Giacobino. "Linear input-output method for quantum fluctuations in optical bistability with two-level atoms". *Phys. Rev. A* 46 (7 1992), pp. 4397–4405. DOI: `10.1103/PhysRevA.46.4397` (Cited on page 34).

[120] L. Zhong, E. P. Menzel, R. D. Candia, P. Eder, et al. "Squeezing with a flux-driven Josephson parametric amplifier". *New Journal of Physics* 15.12 (2013), p. 125013. DOI: `10.1088/1367-2630/15/12/125013` (Cited on page 36).

[121] K. Satoh, D. Koizumi, and S. Narahashi. "Compact HTS bandpass filter employing CPW quarter-wavelength resonators with strongly-coupled open stubs". 97.1 (2008), p. 012132. DOI: `10.1088/1742-6596/97/1/012132` (Cited on page 36).

[122] M. Göppl, A. Fragner, M. Baur, R. Bianchetti, et al. "Coplanar waveguide resonators for circuit quantum electrodynamics". *Journal of Applied Physics* 104.11 (2008), p. 113904. DOI: `10.1063/1.3010859` (Cited on page 36).

[123] L. J. Zeng, P. Krantz, S. Nik, P. Delsing, et al. "The atomic details of the interfacial interaction between the bottom electrode of Al/AlOx/Al Josephson junctions and HF-treated Si substrates". *Journal of Applied Physics* (2015). DOI: `10.1063/1.4919224` (Cited on page 39).

[124] C. R. H. McRae, H. Wang, J. Gao, M. R. Vissers, et al. "Materials loss measurements using superconducting microwave resonators". *Review of Scientific Instruments* 91.9 (2020), p. 091101. DOI: `10.1063/5.0017378`. eprint: `https://doi.org/10.1063/5.0017378` (Cited on pages 41, 48).

[125] A. Premkumar, C. Weiland, S. Hwang, B. Jäck, et al. "Microscopic relaxation channels in materials for superconducting qubits". *Communications Materials* 2.72 (2021). DOI: `10.1038/s43246-021-00174-7` (Cited on pages 41, 44).

[126] B. Bonin and H. Safa. "Power dissipation at high fields in granular RF superconductivity". *Superconductor Science and Technology* 4.6 (1991), pp. 257–261. DOI: `10.1088/0953-2048/4/6/008` (Cited on page 41).

[127] M. Newville, A. Ingargiola, T. Stensitzki, and D. B. Allen. “LMFIT: Non-Linear Least-Square Minimization and Curve-Fitting for Python”. *Zenodo* (2014) (Cited on page 43).

[128] J. K. Hulm, C. K. Jones, R. A. Hein, and J. W. Gibson. “Superconductivity in the TiO and NbO systems”. *Journal of Low Temperature Physics* (1972). DOI: `10.1007/BF00660068` (Cited on page 44).

[129] M. R. Soares, S. Leite, C. Nico, M. Peres, et al. “Effect of processing method on physical properties of Nb2O5”. *Journal of the European Ceramic Society* (2011). DOI: `10.1016/j.jeurceramsoc.2010.10.024` (Cited on page 44).

[130] J. Zmuidzinas. “Superconducting Microresonators: Physics and Applications”. *Annual Review of Condensed Matter Physics* 3.1 (2012), pp. 169–214. DOI: `10.1146/annurev-conmatphys-020911-125022`. eprint: `https://doi.org/10.1146/annurev-conmatphys-020911-125022` (Cited on page 46).

[131] D. S. Wisbey, M. R. Vissers, J. Gao, J. S. Kline, et al. “Dielectric Loss of Boron-Based Dielectrics on Niobium Resonators”. *Journal of Low Temperature Physics* 195.5 (2019), pp. 474–486. DOI: `10.1007/s10909-019-02183-w` (Cited on page 46).

[132] J Burnett, L Faoro, and T Lindström. “Analysis of high quality superconducting resonators: consequences for TLS properties in amorphous oxides”. *Superconductor Science and Technology* 29.4 (2016), p. 044008. DOI: `10.1088/0953-2048/29/4/044008` (Cited on page 48).

[133] J. B. Chang, M. R. Vissers, A. D. Córcoles, M. Sandberg, et al. “Improved superconducting qubit coherence using titanium nitride”. *Applied Physics Letters* 103.1 (2013), p. 012602. DOI: `10.1063/1.4813269`. eprint: `https://doi.org/10.1063/1.4813269` (Cited on page 48).

[134] K. Gottfried and T.-M. Yan. “Fundamental Concepts”. In: *Quantum Mechanics: Fundamentals*. New York, NY: Springer New York, 2003, pp. 1–25. DOI: `10.1007/978-0-387-21623-2_1` (Cited on page 52).

[135] V. Gorini, A. Kossakowski, and E. C. G. Sudarshan. “Completely positive dynamical semigroups of N-level systems”. *Journal of Mathematical Physics* 17.5 (1976), pp. 821–825. DOI: `10.1063/1.522979`. eprint: `https://aip.scitation.org/doi/pdf/10.1063/1.522979` (Cited on page 54).

[136] G. Lindblad. “On the generators of quantum dynamical semigroups”. *Communications in Mathematical Physics* 48.2 (1976), pp. 119 –130 (Cited on page 54).

[137] A. G. Redfield. “The Theory of Relaxation Processes* *This work was started while the author was at Harvard University, and was then partially supported by Joint Services Contract N5ori-76, Project Order I.” In: *Advances in Magnetic Resonance*. Ed. by J. S. Waugh. Vol. 1. Advances in Magnetic and Optical Resonance. Academic Press, 1965, pp. 1–32. DOI: `https://doi.org/10.1016/B978-1-4832-3114-3.50007-6` (Cited on page 56).

[138] D. Jaschke, L. Carr, and I. Vega. “Thermalization in the quantum Ising model—approximations, limits, and beyond”. *Quantum Science and Technology* 4.3 (2019), p. 034002. DOI: `10.1088/2058-9565/ab1a71` (Cited on page 59).

[139] S. Nakajima. “On Quantum Theory of Transport Phenomena: Steady Diffusion”. *Progress of Theoretical Physics* 20.6 (Dec. 1958), pp. 948–959. DOI: `10.1143/PTP.20.948`. eprint: `https://academic.oup.com/ptp/article-pdf/20/6/948/5440766/20-6-948.pdf` (Cited on page 60).

[140] R. Zwanzig. “Ensemble Method in the Theory of Irreversibility”. *The Journal of Chemical Physics* 33.5 (1960), pp. 1338–1341. DOI: `10.1063/1.1731409`. eprint: `https://doi.org/10.1063/1.1731409` (Cited on page 60).

[141] H. P. Breuer and F. Petruccione. *The Theory of Open Quantum Systems*. Oxford University Press, Jan. 2007. DOI: `10.1093/acprof:oso/9780199213900.001.0001` (Cited on page 60).

[142] J. F. Poyatos, J. I. Cirac, and P. Zoller. “Complete Characterization of a Quantum Process: The Two-Bit Quantum Gate”. *Phys. Rev. Lett.* 78 (2 1997), pp. 390–393. DOI: `10.1103/PhysRevLett.78.390` (Cited on page 64).

[143] J. Cerrillo and J. Cao. “Non-Markovian Dynamical Maps: Numerical Processing of Open Quantum Trajectories”. *Phys. Rev. Lett.* 112 (11 2014), p. 110401. DOI: `10.1103/PhysRevLett.112.110401` (Cited on page 64).

[144] F. A. Pollock and K. Modi. “Tomographically reconstructed master equations for any open quantum dynamics”. *Quantum* 2 (July 2018), p. 76. DOI: `10.22331/q-2018-07-11-76` (Cited on pages 64, 73).

[145] M. A. Nielsen and I. L. Chuang. *Quantum Computation and Quantum Information: 10th Anniversary Edition*. Cambridge University Press, 2010. DOI: `10.1017/CBO9780511976667` (Cited on pages 65, 68).

[146] S. Wißmann, A. Karlsson, E. Laine, J. Piilo, et al. “Optimal state pairs for non-Markovian quantum dynamics”. *Physical Review A* 86.6 (2012). DOI: `10.1103/physreva.86.062108` (Cited on page 67).

[147] H.-P. Breuer, E.-M. Laine, J. Piilo, and B. Vacchini. “Colloquium: Non-Markovian dynamics in open quantum systems”. *Rev. Mod. Phys.* 88 (2 2016), p. 021002. DOI: `10.1103/RevModPhys.88.021002` (Cited on page 67).

[148] D. P. Nadlinger, P. Drmota, B. C. Nichol, G. Araneda, et al. “Experimental quantum key distribution certified by Bell’s theorem”. *Nature* 607.7920 (2022), pp. 682–686. DOI: `10.1038/s41586-022-04941-5` (Cited on page 67).

[149] J. F. Clauser, M. A. Horne, A. Shimony, and R. A. Holt. “Proposed Experiment to Test Local Hidden-Variable Theories”. *Phys. Rev. Lett.* 23 (15 1969), pp. 880–884. DOI: `10.1103/PhysRevLett.23.880` (Cited on page 68).

[150] M. B. Plenio. "Logarithmic Negativity: A Full Entanglement Monotone That is not Convex". *Physical Review Letters* 95.9 (2005). DOI: `10.1103/physrevlett.95.090503` (Cited on page 68).

[151] W. K. Wootters. "Entanglement of Formation of an Arbitrary State of Two Qubits". *Physical Review Letters* 80.10 (1998), pp. 2245–2248. DOI: `10.1103/physrevlett.80.2245` (Cited on page 68).

[152] M. Ziman and V. Buzek. "Concurrence versus purity: Influence of local channels on Bell states of two qubits". *Phys. Rev. A* 72 (5 2005), p. 052325. DOI: `10.1103/PhysRevA.72.052325` (Cited on page 70).

[153] J. Piilo, K. Härkönen, S. Maniscalco, and K.-A. Suominen. "Open system dynamics with non-Markovian quantum jumps". *Phys. Rev. A* 79 (6 2009), p. 062112. DOI: `10.1103/PhysRevA.79.062112` (Cited on page 73).

[154] J. Morris, F. A. Pollock, and K. Modi. "Quantifying non-Markovian Memory in a Superconducting Quantum Computer". *Open Systems & Information Dynamics* 29.02 (2022). DOI: `10.1142/s123016122250007x` (Cited on page 73).

[155] A. G. Fowler, M. Mariantoni, J. M. Martinis, and A. N. Cleland. "Surface codes: Towards practical large-scale quantum computation". *Phys. Rev. A* 86 (3 2012), p. 032324. DOI: `10.1103/PhysRevA.86.032324` (Cited on page 73).

[156] E. Vlachos, H. Zhang, V. Maurya, J. Marshall, et al. "Master equation emulation and coherence preservation with classical control of a superconducting qubit". *Phys. Rev. A* 106 (6 2022), p. 062620. DOI: `10.1103/PhysRevA.106.062620` (Cited on page 73).

[157] M. Ringbauer, C. Wood, K. Modi, A. Gilchrist, et al. "Characterizing Quantum Dynamics with Initial System-Environment Correlations". *Physical Review Letters* 114.9 (2015). DOI: `10.1103/physrevlett.114.090402` (Cited on page 73).

[158] B.-H. Liu, X.-M. Hu, Y.-F. Huang, C.-F. Li, et al. "Efficient superdense coding in the presence of non-Markovian noise". 114.1 (2016), p. 10005. DOI: `10.1209/0295-5075/114/10005` (Cited on page 74).

[159] E.-M. Laine, H.-P. Breuer, J. Piilo, C.-F. Li, et al. "Nonlocal Memory Effects in the Dynamics of Open Quantum Systems". *Phys. Rev. Lett.* 108 (21 2012), p. 210402. DOI: `10.1103/PhysRevLett.108.210402` (Cited on page 74).

[160] N. K. Bernardes, A. Cuevas, A. Orieux, C. H. Monken, et al. "Experimental observation of weak non-Markovianity". *Scientific Reports* 5.1 (2015), p. 17520. DOI: `10.1038/srep17520` (Cited on page 74).

[161] P. M. Burrage and K. Burrage. "A Variable Stepsize Implementation for Stochastic Differential Equations". *SIAM Journal on Scientific Computing* 24.3 (2003), pp. 848–864. DOI: `10.1137/S1064827500376922`. eprint: `https://doi.org/10.1137/S1064827500376922` (Cited on page 75).

[162] K. Mølmer and Y. Castin. “Monte Carlo Wavefunctions”. In: *Coherence and Quantum Optics VII.* Ed. by J. H. Eberly, L. Mandel, and E. Wolf. Boston, MA: Springer US, 1996, pp. 193–202 (Cited on page 75).

[163] J. Johansson, P. Nation, and F. Nori. “QuTiP 2: A Python framework for the dynamics of open quantum systems”. *Computer Physics Communications* 184.4 (2013), pp. 1234–1240. DOI: `https://doi.org/10.1016/j.cpc.2012.11.019` (Cited on page 75).

[164] J. Johansson, P. Nation, and F. Nori. “QuTiP: An open-source Python framework for the dynamics of open quantum systems”. *Computer Physics Communications* 183.8 (2012), pp. 1760–1772. DOI: `https://doi.org/10.1016/j.cpc.2012.02.021` (Cited on page 75).

[165] H. Chen and D. A. Lidar. “Hamiltonian open quantum system toolkit”. *Communications Physics* 5.1 (2022), p. 112. DOI: `10.1038/s42005-022-00887-2` (Cited on page 75).

[166] Z. K. Minev, Z. Leghtas, S. O. Mundhada, L. Christakis, et al. “Energy-participation quantization of Josephson circuits”. *npj Quantum Information* (2021). DOI: `10.1038/s41534-021-00461-8`. arXiv: `2010.00620` (Cited on page 78).

[167] Z. K. Minev, T. G. McConkey, J. Drysdale, P. Shah, et al. *Qiskit Metal: An Open-Source Framework for Quantum Device Design & Analysis.* 2021. DOI: `10.5281/zenodo.4618153` (Cited on page 80).

[168] Z. K. Minev, Z. Leghtas, P. Reinhold, S. O. Mundhada, et al. *pyEPR: The energy-participation-ratio (EPR) open- source framework for quantum device design.* https://github.com/zlatko-minev/pyEPR https ://pyepr-docs.readthedocs.io/en/latest/. May 2021. DOI: `10.5281/zenodo.4744447` (Cited on page 80).

[169] J. Majer, J. M. Chow, J. M. Gambetta, J. Koch, et al. “Coupling superconducting qubits via a cavity bus”. *Nature* 449.7161 (2007), pp. 443–447. DOI: `10.1038/nature06184` (Cited on page 81).

[170] D. S. Wisbey, A. Martin, A. Reinisch, and J. Gao. “New Method for Determining the Quality Factor and Resonance Frequency of Superconducting Micro-Resonators from Sonnet Simulations”. *Journal of Low Temperature Physics* 176.3 (2014), pp. 538–544. DOI: `10.1007/s10909-014-1099-3` (Cited on page 83).

[171] D. M. Pozar. *Microwave engineering.* Fourth edition. Hoboken, NJ : Wiley, [2012] ©2012, [2012] (Cited on page 83).

[172] J. Niemeyer and V. Kose. “Observation of large dc supercurrents at nonzero voltages in Josephson tunnel junctions”. *Applied Physics Letters* 29.6 (1976), pp. 380–382. DOI: `10.1063/1.89094`. eprint: `https://doi.org/10.1063/1.89094` (Cited on page 86).

[173] G. J. Dolan. “Offset masks for lift-off photoprocessing”. 31.5 (Sep 1977), pp. 337–339 (Cited on page 86).

[174] V. Ambegaokar and A. Baratoff. “Tunneling Between Superconductors”. *Phys. Rev. Lett.* 10 (11 1963), pp. 486–489. DOI: `10.1103/PhysRevLett.10.486` (Cited on page 88).

[175] D. Slichter. “Quantum Jumps and Measurement Backaction in a Superconducting Qubit”. In: 2011 (Cited on page 92).

[176] A. Ranadive, M. Esposito, L. Planat, E. Bonet, et al. “Kerr reversal in Josephson meta-material and traveling wave parametric amplification”. *Nature Communications* 13.1 (2022), p. 1737. DOI: `10.1038/s41467-022-29375-5` (Cited on page 92).

[177] A. Vepsäläinen, R. Winik, A. H. Karamlou, J. Braumüller, et al. “Improving qubit coherence using closed-loop feedback”. *Nature Communications* 13.1 (2022), p. 1932. DOI: `10.1038/s41467-022-29287-4` (Cited on page 95).

[178] S. W. Jolin, R. Borgani, M. O. Tholén, D. Forchheimer, et al. “Calibration of mixer amplitude and phase imbalance in superconducting circuits”. *Review of Scientific Instruments* 91.12 (2020), p. 124707. DOI: `10.1063/5.0025836`. eprint: `https://doi.org/10.1063/5.0025836` (Cited on page 96).

[179] S. Filipp, P. Maurer, P. J. Leek, M. Baur, et al. “Two-qubit state tomography using a joint dispersive readout”. *Physical Review Letters* (2009). DOI: `10.1103/PhysRevLett.102.200402`. arXiv: `0812.2485` (Cited on page 97).

[180] J. M. Chow, L. Dicarlo, J. M. Gambetta, A. Nunnenkamp, et al. “Detecting highly entangled states with a joint qubit readout”. *Physical Review A - Atomic, Molecular, and Optical Physics* (2010). DOI: `10.1103/PhysRevA.81.062325` (Cited on page 97).

[181] K. Banaszek, G. M. D’Ariano, M. A. Paris, and M. F. Sacchi. “Maximum-likelihood estimation of the density matrix”. *Physical Review A - Atomic, Molecular, and Optical Physics* (2000). DOI: `10.1103/PhysRevA.61.010304`. arXiv: `9909052 [quant-ph]` (Cited on page 99).

[182] P. Virtanen, R. Gommers, T. E. Oliphant, M. Haberland, et al. “SciPy 1.0: Fundamental Algorithms for Scientific Computing in Python”. *Nature Methods* 17 (2020), pp. 261–272. DOI: `10.1038/s41592-019-0686-2` (Cited on page 100).

[183] J. M. Chow, A. D. Córcoles, J. M. Gambetta, C. Rigetti, et al. “Simple All-Microwave Entangling Gate for Fixed-Frequency Superconducting Qubits”. *Phys. Rev. Lett.* 107 (8 2011), p. 080502. DOI: `10.1103/PhysRevLett.107.080502` (Cited on page 104).

[184] A. D. Córcoles, J. M. Gambetta, J. M. Chow, J. A. Smolin, et al. “Process verification of two-qubit quantum gates by randomized benchmarking”. *Phys. Rev. A* 87 (3 2013), p. 030301. DOI: `10.1103/PhysRevA.87.030301` (Cited on page 105).

[185] V. Tripathi, M. Khezri, and A. N. Korotkov. “Operation and intrinsic error budget of a two-qubit cross-resonance gate”. *Phys. Rev. A* 100 (1 2019), p. 012301. DOI: `10.1103/PhysRevA.100.012301` (Cited on page 106).

[186] M. Ware, B. R. Johnson, J. M. Gambetta, T. A. Ohki, et al. “Cross-resonance interactions between superconducting qubits with variable detuning”. 2 (2019), pp. 1–7. arXiv: `1905.11480` (Cited on page 107).